Towards Comprehensive Magnetic Resonance Imaging of Heterogeneously Catalyzed Reactions using Methanation as Case Study

Vom Fachbereich Produktionstechnik
der
UNIVERSITÄT BREMEN

zur Erlangung des Grades
Doktor-Ingenieur
genehmigte

Dissertation
von
Harm Ridder, M. Sc.

Gutachter:
Prof. Dr.-Ing. Jorg Thöming
Prof. Dr. Alexander Penn (Technische Universität Hamburg)

Tag der mündlichen Prüfung: 11.01.2024

Zusammenfassung

Die Optimierung chemischer Reaktionen im Hinblick auf eine effizientere Energie-nutzung sowie die Einführung neuer Prozessrouten sind wichtige Faktoren, um das Ziel der Klimaneutralität in der chemischen Industrie erreichen zu können. Da chemische Reaktoren jedoch blickdicht und unzugänglich für viele Messmethoden sind, ist eine Bewertung der Effektivität verschiedener Optimierungsmaßnahmen nur schwer möglich. Die Magnetresonanztomographie (MRT) bietet mehrere Möglichkeiten, die an der chemischen Reaktion beteiligten Stoffe nicht-invasiv zu charakterisieren und neue Erkenntnisse über das Reaktionssystem zu gewinnen. Die Anwendung von MRT-Methoden für chemische Reaktoren wird jedoch häufig durch physikalische Beschränkungen wie den möglichen Temperaturbereich und die Tatsache behindert, dass die gemessenen Parameter in der Regel von mehreren Reaktionsparametern abhängig sind. Prozesse in der Gasphase zu vermessen stellt dabei eine besondere Herausforderung dar, da Gase aufgrund der niedrigen Dichte nur eine geringe Signalintensität für die Messung anbieten.

In dieser Arbeit wird eine neue Technik zur Untersuchung von Gasphasenprozessen in der katalytisch aktiven Zone eines chemischen Reaktors vorgestellt. Die Combined Temperature and Density (CTD)-Technik ist in der Lage, eine dreidimensionale Verteilung der Temperatur und der Moleküldichte zu messen, die zum Beispiel zur Lokalisierung von Hotspots in der katalytisch aktiven Zone verwendet werden kann. Die Methode wird auf die Methanisierungsreaktion unter Verwendung einer Saturation-Recovery-Sequenz angewandt, wobei die gleichzeitige Messung der Signalamplitude und der longitudinalen Relaxationszeit T_1 ausgenutzt wird, um Informationen über Temperatur und Dichte von Methan direkt aus der Gasphase zu gewinnen. Um die anspruchsvolle Methanisierung im MR-Scanner realisieren zu können, wurde ein MRT-kompatibler Reaktor entwickelt und gebaut. Dieser ist in der Lage den elektromagnetischen Signalaustausch zu ermöglichen und gleichzeitig erhöhten Druck und Temperatur der Reaktion vom MRT zurückzuhalten. Für die Anwendung der CTD-Technik auf die Methanisierung sind Wechselwirkungspara-meter erforderlich, die aus eigens entwickelten Messungen extrahiert werden. Dies ermöglicht im Anschluss die Temperatur- und Dichteverteilungen verschiedener stationärer Zustände der Methanisierungsreaktion darzustellen und zu vergleichen. Die Unterschiede in der Temperatur- und Dichteverteilung lassen sich deutlich erkennen und ermöglichen so, die lokalen Reaktionslimitierungen zu identifizieren.

Abstract

The optimization of chemical reactions towards more efficient energy use as well as the implementation of new process routes are essential factors in the goal of reaching climate neutrality for the chemical industry. For this, reactor designs have to be reworked and tuned, but insight into chemical reactors is scarce due to the opaque nature of chemical reactors. Magnetic resonance imaging (MRI) techniques offer multiple ways to characterize the participants of the chemical reaction and gain new insight into the reaction system. However, the application of MRI methods for chemical reactors is often hindered by physical limitations like the feasible temperature range and the fact that parameters studied using MRI are usually dependent on various reaction parameters. Processes in the gas phase are increasingly hard to study due to the low density of the substances in comparison to the liquid phase.

This thesis presents a new technique to study gas-phase processes *operando* in the catalytically active zone of a chemical reactor. The Combined Temperature and Density (CTD) technique can measure a three-dimensional spatial distribution of temperature and molecular number density, which can, for instance, be used to locate hot spots in the catalytically active zone. The method is applied to the methanation reaction using a saturation recovery sequence, exploiting the simultaneous measurement of the signal amplitude and the longitudinal relaxation time T_1 to gather information about the temperature and density of methane directly from the gas phase. To perform the challenging methanation inside the MR scanner, a special reactor was built which enables electromagnetic signal exchange while retaining the harsh reaction conditions from the setup. Interaction parameters are required to apply the CTD method to the methanation obtained from dedicated measurements. As the final results of this thesis, the distributions of temperature and density are mapped during three different steady states of the methanation reaction. The differences in temperature and density distribution are clearly distinguishable, and local limitations of the chemical reaction can be identified.

Danksagung

Mit dieser Arbeit ist eine lange Zeit des Denkens, Diskutierens, Ausprobierens, Lernens, Verwerfens und Zweifelns einhergegangen, die ohne die Menschen um mich herum im professionellen sowie im persönlichen Kontext nicht möglich gewesen wäre.

Zuallererst möchte ich mich bei meinem Doktorvater Jorg Thöming bedanken, der diese Arbeit nicht nur ermöglicht hat, sondern mir immer mit großem Vertrauen sowohl in meine Arbeit und Fertigkeiten als auch für den Ausgang des Projekts begegnet ist. Dank ihm konnte ich viele meiner eigenen Ziele und Ideen in dieser Arbeit ausprobieren und in die Tat umsetzen.

Außerdem möchte ich mich bei Alexander Penn bedanken, dass er diese Arbeit als Zweitgutachter übernommen hat.

Mein besonderer Dank gilt meinem NMR-Betreuer Wolfgang Dreher. Nicht nur hat er immer Zeit gefunden, um mit mir meine vielen Fragen und abwegigen Ideen zu diskutieren und mir dabei die NMR-Welt näherzubringen. Außerdem hat Wolfgang mit einer unglaublichen Selbstverständlichkeit von früh bis spät mit mir am Magneten gearbeitet und sich auf alle Messungen eingelassen, die nur irgendwie physikalisch möglich waren.

Ebenso möchte ich mich bei meinem zweiten Betreuer Georg Pesch bedanken, dass er sich mit uns in zwei neue Themengebiete eingearbeitet und durch seine Korrekturen auf sehr hohem sprachlichen Niveau mehr für meine Textarbeit getan hat als all meine SchullehrerInnen zusammen.

Außerdem möchte ich mich bei der AG Bäumer, bei Roswitha Krebs-Goldbecker aus der glastechnischen Werkstatt und bei der feinmechanischen Werkstatt für ihre Untersützung beim Bau und bei der Umsetzung der Versuchsaufbauten bedanken.

Ein ganz besonderer Dank geht an meine Frau Sophie. Danke, dass Du in allen Lebenslagen für mich da bist und ich all die Emotionen und Momente der Promotion mit Dir teilen konnte.

Diese Arbeit hätte nicht so entstehen können ohne die vielen Gespräche mit meinen KollegInnen und FreundInnen. Der offene, freundliche und lösungsorientierte Geist, der bei uns in der Arbeitsgruppe herrscht ist ein starker Katalysator für Ideen und Forschungsvorhaben, der mich immer wieder aufs neue begeistert.

Insbesondere möchte ich mich bei Christoph, Jonas und Jasper bedanken, die mich seit der Studienzeit begleiten und auf vielfältige Weise zu dieser Arbeit beigetragen

haben.

Zuguterletzt möchte ich mich bei meiner Familie bedanken, dass sie immer für mich da war und meinen Weg in die naturwissenschaftliche Welt schon früh unterstützt hat.

List of publications

First author

- Harm Ridder, Christoph Sinn, Georg R. Pesch, Jan Ilsemann, Wolfgang Dreher, and Jorg Thöming. "A large fixed bed reactor for MRI operando experiments at elevated temperature and pressure". In: *Review of Scientific Instruments* 92.4 (2021), p. 043711. DOI: 10.1063/5.0044795.

- Harm Ridder, Christoph Sinn, Georg R. Pesch, Wolfgang Dreher, and Jorg Thöming. "Spatially resolved direct gas-phase thermometry in chemical reactors using NMR". in: *Chemical Engineering Journal* 433.September 2021 (2022), p. 133583. DOI: 10.1016/j.cej.2021.133583.

- Harm Ridder, Christoph Sinn, Georg R Pesch, Wolfgang Dreher, and Jorg Thöming. "Longitudinal Relaxation (T1) of Methane/Hydrogen Mixtures for Operando Characterization of Gas-Phase Reactions". In: *ACS Measurement Science Au* 2.5 (2022), pp. 449–456. DOI: 10.1021/acsmeasuresciau.2c00022.

Additional

- Mojtaba Mirdrikvand, Harm Ridder, Jorg Thöming, and Wolfgang Dreher. "Diffusion weighted magnetic resonance imaging for temperature measurements in catalyst supports with an axial gas flow". In: *Reaction Chemistry and Engineering* 4.10 (2019), pp. 1844–1853. DOI: 10.1039/c9re00082h.

- Georg R Pesch, Harm Ridder, and Christoph Sinn. "Operando characterization of heterogeneously catalyzed gas- and multi-phase reactions using nuclear magnetic resonance imaging". In: *Chemical Engineering and Processing - Process Intensification* 179.August (2022), p. 109086. DOI: 10.1016/j.cep.2022.109086.

Contents

Introduction

The reduction of greenhouse gas (GHG) emissions to fight climate change is one of the main challenges of our time. In 2016, industrial processes accounted for almost 30 % of the global anthropogenic GHG emissions, of which over 80 % can be rooted in energy consumption [6]. The demand to reduce GHG in the industry is met by supplying environmentally friendly energy and reducing overall energy consumption. However, many processes are challenging to decarbonize, and new process routes must be found.

The rejection of fossil fuels changes the way energy is produced and demands a change of current fossil feedstock-based process routes. Above all, the chemical industry relies on high-value chemicals like ethylene, benzene, and toluene to produce polymers, all of which are hydrocarbons produced from crude oil. Not only is carbon dioxide a direct product of, for instance, the production of ammonia. At the end of the life cycle, most chemical industry products cannot be recycled and are burned, which releases the carbon stored inside as carbon dioxide [7].

The conversion to a climate-friendly chemical industry sector creates an enormous demand for renewable energy and chemicals for industrial processes. One way to meet this demand is the use of Power-to-Gas or Power-to-Liquid technologies (PtX). PtX is designed to store renewable energy from windmills or solar farms by creating hydrogen from electrolysis and combining it with sequestrated carbon to form hydrocarbons such as methane, methanol, synthetic fuel, or other chemicals [8–10]. The processes have in common that they are heterogeneously catalyzed reactions, meaning that the process is catalyzed on a solid surface to accelerate the chemical reaction of the bulk material in the gas or liquid phase [11].

One prominent example of a PtX process is the CO_2 methanation, where carbon dioxide reacts with hydrogen to methane and water [12]. In order to improve the efficiency of the reaction system (i.e., reactor and reacting conditions) used for the methanation process, it is crucial to understand the macroscopic transport processes of heat, mass, and momentum inside the reactor [13]. Several technologies are available to study these transport processes in the opaque reactor and they come with their benefits and drawbacks. For instance, gas chromatography and mass

spectrometry offer detailed measurements of species concentration but can only measure *ex-situ* from the outlet or a tap [14, 15]. Other systems insert a small tube or capillary to probe gas and temperature along the tube dimension inside the reactor [16–18]. Only Magnetic Resonance Imaging (MRI) techniques offer the possibility to study the gas phase within the reactor during operation (*operando*) and spatially resolved. MRI can be applied to lab scale reactors without disturbing the transport in the actual reaction system [19–23].

1.1 Objective of this thesis

This thesis demonstrates an application of MRI techniques to a heterogeneously catalyzed gas-phase reaction to gain advanced insight into the process. Remarkable progress has been made such that MRI-based techniques can now map process parameters of chemical reactions spatially, such as velocities [24–28], mass transport [29, 30], temperature [4, 28, 31], and species distributions [32–34] in the opaque structure of a chemical reactor. While the fact that the measurements were made possible by the researchers is an achievement of their own, the mentioned works are not yet able to translate their findings into new insight of chemical reactors. One reason is that substantial simplifications were necessary to enable the measurements, e.g., measurement at non-reaction conditions (standard temperature and pressure; STP), insertions of probing liquids, limited spatial or timely resolution, or the study of too-simplified reactions.

In an attempt to challenge the drawbacks of current studies, the goal of this work is the development of an experimental setup as well as methods that can be used to study industrially relevant chemical reactions without the need to alter the actual operating conditions. As a benchmark, *operando* and 3D spatially resolved measurements of the methanation reaction are carried out to visualize the temperature and density distribution of methane. As this type of measurement carries many new and undescribed aspects, a secondary goal of the thesis is to elucidate the obstacles encountered in the development process and the limitations that might bias the results of the measurement.

1.2 Structure of this thesis

The different chapters of this thesis show the developments required to directly measure the temperature and molar concentration of methane during the methanation reaction using MRI. In the next chapter, the state of the art of chemical reactors and their study using MRI is briefly covered alongside the theoretical background on which the method and conclusions of this work are based. Chapter 3 describes the different experimental features of the measurement setup. A particular emphasis is put on the chemical reactor for MR applications designed and built in the context of this work. The experimental part is followed by Chapter 4 which describes the new Combined Temperature and Density (CTD) method that can simultaneously measure methane concentration and temperature. To reach the goal of this work which is to apply this new method to the methanation reaction, the cross section for the collision of methane σ_j is required. The experiments used to quantify this parameter for methane in hydrogen and methane in water are covered in Chapter 5. Chapter 6 presents the measurements of the methanation reaction using the CTD method. In the last chapter, the findings of this thesis are evaluated, and an outlook for future works is given.

A remark on data availability
The experimental data used in this study is openly shared in Zenodo archives that are part of the open-access publications on which this work is based. The results of Chapter 5.2 and Chapter 6 will be published in open-access publication in the near future, featuring the experimental data. A basic version of the graphical user interface (GUI) and different functions that are used for processing MR data and for data quantification can be found in the Zenodo archives as well. The current version can be downloaded from `https://github.com/HarmRidder/MATLAB-GUI-for-MRI`.

2

Scientific and technological background

2.1 Overview

Chemical reactions are essential to manufacturing goods in almost all parts of industry. In the process of converting one molecule to another, the energy stored in the atomic bonds of the molecule changes, and energy in the form of heat is either consumed or released when new molecules are formed. The respective name for this is the endothermic or exothermic reaction, the latter being the more common one [11]. In technical processes, where reactions are performed on a large scale, heat management is an important factor as the energy needs to be either removed or brought into the system to sustain the chemical reaction [35, 36]. For this and different other purposes, chemical reactions are usually performed in a reactor. The reactor contains the participants of the reaction and prevents interaction with the outside, allows to set a defined pressure, and controls the mixing behavior of certain species, if necessary. The most common material for chemical reactors is stainless steel, which is resistant to chemicals and high temperatures, and has a high ductility to enable immense pressures inside the reactor.

Chemical reactions require a specific temperature to split the atomic bonds in the reaction process, which is often way above ambient temperature. Catalysts facilitate the splitting of the current bonds or the formation of new ones by offering an intermediate bonding partner, reducing the temperature required for the reaction [11]. The catalyst is not consumed in the process and can be used many times before its ability deteriorates. Thus, removing catalysts from the product stream is essential. In homogeneous catalysis, where the catalyst is part of the liquid phase, a separation step is required in the post-processing [37]. In heterogeneous catalysis, the catalyst is fixated on a solid support material to circumvent mixing of the catalyst into the

bulk. In gas phases, only heterogeneous catalysis is performed.

The most common method to fixate a catalyst on a solid material is the impregnation of so-called pellets. These are formed by pelletizing powders of metal oxides like alumina (Al_2O_3), silica (SiO_2), or titanium oxide (TiO_2) [38–40] into different shapes like spheres, cylinders, or Raschig rings [41]. The impregnation of the porous pellets deposits catalyst nanoparticles inside the pores, which the surrounding gas can access through diffusion. The second method for catalyst fixation uses monolithic structures like honeycombs or solid sponges. The catalyst nanoparticles are deposited in the porous wash coat, through which gas can access the catalyst nanoparticles similar to pellets. The wash coat is an additional layer that is brought onto the solid structure by depositing a slurry on the monolith. The slurry is a liquid containing a ceramic material and the catalyst. Through sintering, it is fixated on the monolith and pores form.

All these components combined, the reactor, the catalyst, and the chemical reaction itself, are called the reaction system as they all change the chemical reaction's performance (e.g., yield or stability). The performance is usually characterized by measuring concentrations at the outlet of or along the reactor and by measuring the temperature inside the catalytic bed using one or more thermo sensors (e.g., thermocouples) [14, 16]. Outlet measurements, however, can only resolve changes inside the reactor as integral values as the measured value is already subject to mixing effects both in temperature and concentration. The use of thermo sensors disturbs the transport inside the reactor and softens the measured values of local hot spots, due to their thermal conductivity. As a result, researchers have tried to come up with different approaches to characterize the performance of a chemical reaction system.

One approach to minimize the disturbance of the reactor is the so-called SpaciMS (spatially resolved capillary-inlet mass spectrometry) system. It uses only a small capillary to measure concentration and temperature inside the reactor [16]. The capillary can be moved along one reactor axis, and continuous gas samples are taken through a sampling orifice for analysis in a mass spectrometer. Further, the capillary tip allows for optical measurements, such as Raman spectroscopy, to measure the temperature. Other researchers rely on optical measurements, too, but use a side window in the reactor to make the insight of the reactor accessible for the spectrometers or cameras [42, 43]. Even though these techniques can quantify specific parameters inside the chemical reactor *operando*, they cannot be used without altering the reaction system. The only technique that does not require

changes in the system and can still supply spatially resolved information about a chemical reactor is nuclear magnetic resonance.

MRI is based on the phenomenon called nuclear magnetic resonance (NMR). While the application of NMR spectroscopy for the analysis of chemical substances dates back more than 60 years (e.g., the company Bruker started selling NMR spectrometers in the early '60s [44]), applications involving magnetic resonance imaging to study processes inside chemical reactors only date back about 30 years. Medical MRI applications, which were first used in the early '70s [45], saw a steep rise in usage 20 to 30 years later [46]. However, MRI applications in chemical engineering are still a niche technique. The low amount of publications in the field can partly be explained by the complexity of developing methods to study chemical reactions due to the high diversity of substances encountered and strongly varying process conditions. From a chemical point of view, human bodies exhibit a very defined set of substances that makes developing standards a lot easier. Furthermore, the signal acquired by NMR techniques depends on a large variety of parameters present in the investigated systems, e.g., the molecular number density of a species, molecule movement (diffusive/convective), relaxation (T_1 & T_2), and temperature [22]. These different parameters can be measured using MRI, offering researchers high flexibility to investigate chemical processes. However, a single reaction parameter might depend on different NMR parameters, and only carefully designed experiments yield accurate results. Lastly, it needs to be mentioned that the temperature and pressure conditions required for most catalytic reactions are not favorable for their investigation. Temperatures above 250 °C and pressures larger than 20 bar are common and must be contained inside the reactor to avoid damage to the (very costly) MR magnet and its electrical parts.

As a result of the challenges involved in designing experiments and also the high costs in the purchase and maintenance of MR magnets, research is focused around a few groups in the world. In the last 20 years, the groups of Lynn F. Gladden (Department of Chemical Engineering and Biotechnology, University of Cambridge) and Igor Koptyug (International Tomography Center, Siberian Branch of the Russian Academy of Sciences) performed the lion's share of MRI investigations on chemical reactors. The development over the years has been summarized by Pesch, Ridder, and Sinn [5].

The Gladden group focuses on the study of the Fischer-Tropsch synthesis (FTS) which involved, among others, works on heterogeneously catalyzed gas-to-liquid reactions [21, 33] as model reactions for the FTS and the (mainly diffusive) transport

of hydrocarbons in porous materials [47–49]. They were able to use ethylene glycol-filled spheres to measure the temperature inside a fixed bed by exploiting the temperature dependence of the chemical shift between the two resonance peaks of ethylene glycol [21]. Further, the interaction of liquid water with hydrocarbons in porous pellets was investigated, and it was shown that depending on the pressure, the ratio between the two substances varies [47]. Combining information of chemical shift and diffusion, the diverse product distribution of the ethene oligomerization could be quantified [33]. In the last year, the group was able to consolidate much of the findings of the recent years in an impressive publication where different aspects of the FTS were analyzed, like the distribution of liquid products inside the operating reactor, the carbon number distribution in a single pellet, and the presence of water inside the pellets [34]. Most of the mentioned investigations are made possible by a special reactor design for MR applications developed by Zeton B.V. (Enschede, Netherlands) [50], which features a silicon nitride tube for the reacting zone.

The group of Igor Koptyug published several works on studies of catalytic material and reactions using NMR, such as the transport of catalytic material into a pellet during impregnation [51], flow inside fixed beds [52], and temperature measurements of Al_2O_3 pellets during a chemical reaction [53]. Recently, the group focuses on the usage of parahydrogen-induced signal enhancement. Parahydrogen, formed at low temperatures, can interact with other reactants leading to hyperpolarized species that show a magnetization several orders of magnitude higher than the usual thermodynamic equilibrium [23, 54]. Hyperpolarization counteracts the low amount of signal in gas-phase studies without the need to increase the magnetic field strength, which adversely effects on the magnetic field homogeneity in fixed beds.

In the last decade, the group of Jorg Thöming (Chemical Process Engineering, University of Bremen) – from which this work derives – started working on MRI of heterogeneously catalyzed gas-phase reactions. In collaboration with the in-vivo MR group of the University of Bremen, different works have been published, which studied the product/reactant distribution *operando* inside monoliths [55] and fixed beds [56] during the hydrogenation of ethylene. This reaction is a model reaction because in the industry, ethylene is usually produced from ethane than the other way around. Nevertheless, it was possible to show that *operando* MRI measurements of chemical reactions in the gas phase are possible – a fact that was doubted by researchers before. The ratio between product and reactant was based on the ratio of the signal measured from ethylene and ethane. The separation was possible due to a spatially resolved spectroscopic imaging sequence which produced at

first cross-sectional 2D slices and was later expanded to a 3D spatially resolved spectroscopic imaging (3D-MRSI) sequence. This sequence is still the basis for the measurements carried out in this work. Ulpts et al. [55] used liquid ethylene glycol to measure the temperature at certain spots inside the catalytically active region of the reactor, like the Gladden group did before. However, the capsules or capillaries used to contain the ethylene glycol impeded the measurement of gases in the same region, and the boiling point of the liquid limited the temperature range that could be investigated. Still, using the temperature from an ethylene-glycol-filled capillary at the outside of a monolith as a boundary condition for a 2D pseudo-homogeneous simulation, the temperatures inside the monolith could be predicted reasonably well [32].

Following the works of Ulpts et al., velocimetry studies have been carried out to acquire velocity distributions in monoliths and to compare these to simulations using computational fluid dynamics (CFD) [24, 57]. From the comparison, it could be concluded that the assumption of continuum used for many CFD simulations underestimates the mass transport of the gas against the convective flow direction, which can be crucial in reactive simulations. Even though the measurements have been carried out using pure methane and at ambient temperature, the matching of the results generated by the two techniques was only partially successful.

Recently, works by the group of Alexander Penn (Institute of Process Imaging, Technical University of Hamburg) were published mainly focusing on large-scale reactors. The group could monitor the formation of bubbles in a fluidized bed [28] and the particle movement therein [58]. The works show how complex processes such as bubble formation can be imaged using MRI techniques if the necessary timescale can be met. From the images, the different regimes of bubbly flow in fluidized beds could be visualized, and a new model could be derived to describe the permanent jet regime. In the latest work published by the group, the temperature in a fixed bed could be measured using the chemical shift of water [59].

2.2 Heterogeneously catalyzed gas-phase reactions

The theoretical background given in this chapter is based on *Elements of Chemical Reaction Engineering* by Fogler [41] and *Concepts of Modern Catalysis and Kinetics* by Chorkendorff and Niemantsverdriet [11].

2.2.1 Methanation reaction

The main focus of this work is the characterization of the methanation reaction using MRI methods. The methanation reaction was chosen as it is a prominent example of a power-to-gas technique that can, together with electrolysis, convert electrical energy into chemically stored energy. In the methanation reaction, hydrogen and carbon dioxide react to methane and water [12]

$$4\,H_2 + CO_2 \longrightarrow CH_4 + 2\,H_2O \quad \left(\Delta_R H^{298\,K} = -164\,kJ\,mol^{-1} \right). \quad (2.1)$$
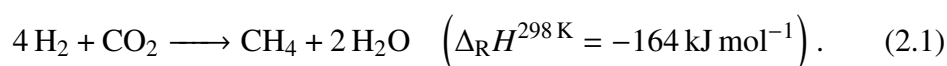
Like all chemical reactions, the methanation reaction is subject to two basic principles, the thermodynamic equilibrium and reactions kinetics. While the latter is a measure for the overall speed of the transformation of molecules, the former describes the equilibrium (after waiting a very long time) between the reaction rate from the reactant to the product site and the reaction rate backward to the reactant. At this point, no net changes in concentration can be observed anymore. Ideally, the reaction kinetic should be as high as possible to reach high yields in short amounts of time, and the thermodynamic equilibrium should be far on the product side. The methanation reaction is exothermic, like most reactions involving a reduction of the number of molecules. According to Le Chatelier's principle, the equilibrium of an exothermic reaction favors the product side of the reaction (here methane and water) with decreasing temperatures and vice versa for endothermic reactions. Further, the equilibrium is shifted to the side with fewer molecules when the pressure increases. The effect of the thermodynamic equilibrium on the highest possible mole fraction of methane during the methanation reaction as a function of the temperature is shown in Figure 2.1a. Pressure and inlet conditions are based on the methanation reaction performed in Chapter 6. From a thermodynamic equilibrium point of view, the reaction should be operated at low temperatures and increased pressure. However, from a kinetics point of view, a high temperature is favorable as the overall reaction rate increases exponentially with temperature (Figure 2.1b).

Kinetics and thermodynamical equilibrium result in reasonable productivity for the methanation reaction only when a catalyst improves the reaction rate. Catalysts reduce a reaction's required activation energy, meaning that less (primarily thermal) energy is required to reach the same reaction rate. This is done by offering an alternative reaction path of intermediate reaction steps. The most common catalyst for the methanation reaction is nickel, while cobalt and iron are also being investigated. Ruthenium is the catalyst of choice for many scientific applications. However, the

price of ruthenium leaves it as a non-feasible choice for industrial applications. Catalysis is a process on the atomic scale where the catalytic material becomes a part of the chemical reaction without being consumed. At least one of the reactants forms a bond with the catalyst, weakening or breaking the bonds to other atoms in the same molecule. As the bonds to the original molecule are weakened, combining with the other reactants is more likely, which increases the reaction rate on the macroscopic level. By choosing a suitable catalyst material in combination with defined parameters of temperature and pressure, chemical reactions can be controlled to yield one product specifically, and side products are mitigated.

The usage of catalysts, however, comes with its challenges in process design and control. As catalysis is a process that occurs only on the surface of the catalyst, the material is usually distributed in the reactor in the form of nanoparticles to increase the active surface area that is available for the reactants. At high temperatures, the catalytic particles tend to agglomerate or sinter to form larger particles, reducing the number of available active sites. This process is summarized with other effects as catalyst deactivation, meaning the reduction of catalytic material available for the reaction.
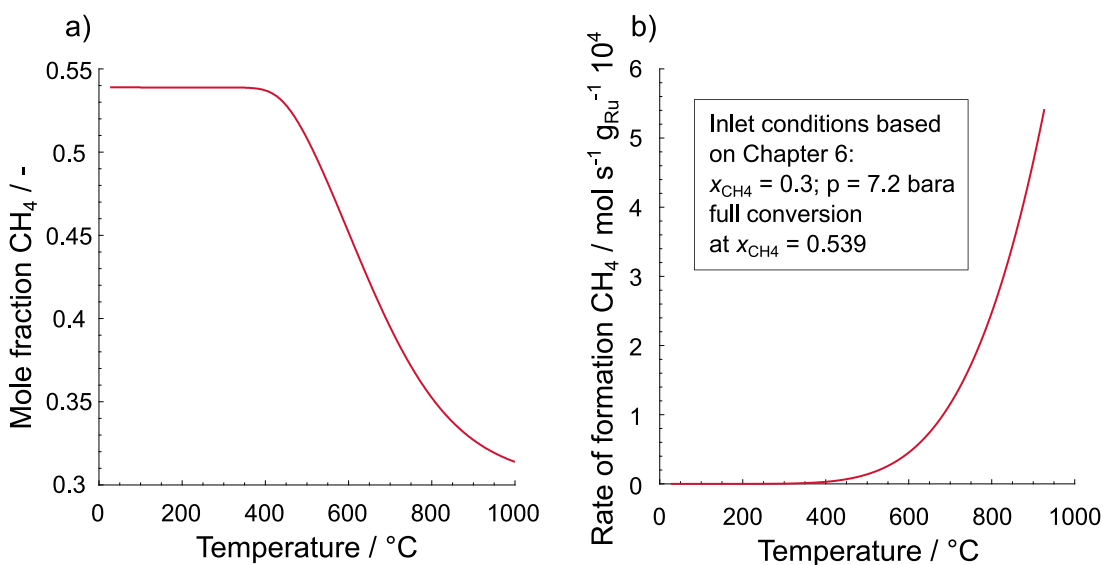
Figure 2.1: a) Highest possible mole fraction of methane that can be reached based on the thermodynamic equilibrium of the methanation reaction. b) Kinetics of the methanation reaction dependent on the temperature at the reactor inlet based on a simplified rate law equation. The calculations are based on inlet conditions following the methanation reaction shown later in this work (Chapter 6). Calculations of the thermodynamic equilibrium in a) are based on [60]. b) is based on an empirical rate law by [12].

2.2.2 Chemical reactors

Thermodynamic equilibrium, reaction kinetics, and catalyst deactivation through exceeding temperatures are all essential factors in the design of chemical reactors. As stated before, chemical reactors control the actual reaction process by bringing reactants (including catalysts) together and setting certain temperatures and pressures as operating conditions. According to the reaction enthalpy $\Delta_R H$, the local temperature changes inside the reactor, adding another level of complexity to the reaction system. The heat released during the exothermic reaction is proportional to the reaction rate. When the heat transport inside the reactor is low compared to the evolving heat, the temperature changes usually lead to so-called hot spots where the heat is nested in some part of the reactor. Through the exponential temperature dependence of the reaction rate, the chemical reaction is strongly favored in the hot spot region, further increasing the evolving heat, thus, fostering the creation of hot spots. An uncontrolled high reaction rate can severely threaten the reactor's security, as uncontrolled side reactions and explosions due to sharply rising pressure can result. Even without these extreme scenarios, the locally high temperatures can lead to catalyst deactivation due to sintering, drastically reducing the efficacy of the catalyst.

Developers often meet the formation of hot spots by trying to limit the available reactant at the catalytic surface site, or improving heat transport inside the reactor. The former method not only reduces the evolving heat but also limits the efficiency of the reactor. The latter method relies on highly thermally conductive material or a reactor design with small length scales and a coolant surrounding the reactor. Heat transport can further be increased by utilizing the convective transport offered by the fluid. However, the higher flow rates for an increase in convection often come with pressure drop and a higher mass flow rate of reactant, meaning that more heat evolves during reaction. Designing a safe and highly efficient chemical reactor is a complex matter subject to many different physical (and monetary) boundary conditions. To fully understand these processes, spatially resolved measurements of the objects inside the reactor are necessary, which can be provided using magnetic resonance imaging techniques.

2.3 Nuclear magnetic resonance

Nuclear magnetic resonance (NMR) measurements exploit the fact that atomic nuclei exhibit resonance in a strong magnetic field. NMR depends on the spin states that the observed nuclei can populate and their interaction. That is why the theory behind the phenomenon of NMR is part of quantum mechanics. As we will soon find out, however, experiments involving NMR require a large amount of spins to yield a measurable result. Many of the quantum mechanic-based expressions can be simplified for an ensemble of spins, yielding equations that are easier applied in the context of a user-defined experiment. This work only shows the non-quantum mechanical approach based on the book *NMR Imaging in Chemical Engineering* by Stapf and Han [22]. For studies directed at the more fundamental theory of NMR, *The Principles of Nuclear Magnetism* by Abragam [61] can be a good starting point.

2.3.1 The NMR signal

When atomic nuclei with a non-zero spin state are treated with an electromagnetic pulse at a certain frequency, the nuclei's energy level can be changed, and the response can be measured to study the properties of a specimen. This behavior is called nuclear magnetic resonance. In most applications – just like in this work – the resonance of the simplest nucleus, the proton (or ^{1}H), is studied. It can populate two different quantum states, $+\frac{1}{2}$ and $-\frac{1}{2}$. As was stated before, an NMR signal can only be measured when a large enough number of nuclei exhibit the same resonance behavior that a device can pick up. To achieve this, the objects of interest are placed in a strong magnetic field, where the spins of the proton align either along the external static magnetic field direction or in the opposite, denoted as N_+ and N_-, respectively. The overhead of aligned spins in one direction compared to the total amount of spins defines the amount of signal that can be derived from an observed volume and is called the degree of polarization θ. It is determined by

$$\theta = \frac{N_+ - N_-}{N_+ + N_-} = \frac{\frac{N_+}{N_-} - 1}{\frac{N_+}{N_-} + 1}. \tag{2.2}$$

The signal amplitude A of an analyzed volume V with N_i molecules of component i each containing S_m NMR-active nuclei then translates into

$$A = CN_i S_\mathrm{m} \theta, \tag{2.3}$$

where the factor C depends on experimental parameters such as the efficacy of the radio frequency (RF) coil or relaxation times. The ratio to encounter one quantum state versus the second $\frac{N_+}{N_-}$ is based on the energy difference between the two states ΔE_q and the thermal energy E_T as described by the Boltzmann distribution

$$\frac{N_+}{N_-} = \exp\left(\frac{\Delta E_q}{E_T}\right) = \exp\left(\frac{\hbar\omega_0}{k_B T}\right). \tag{2.4}$$

Here $\hbar = 1.0546\times10^{-34}\,\mathrm{J\,s}$ is the reduced Planck constant, $k_B = 1.3806\times10^{-23}\,\mathrm{J\,K^{-1}}$ is the Boltzmann constant, and T is the temperature. ω_0 is the Larmor frequency, which is connected to the strength of the surrounding magnetic field B_0 by the gyromagnetic ratio γ of a nucleus using

$$\omega_0 = \gamma\, B_0. \tag{2.5}$$

From this equation it is apparent, that the stronger the applied magnetic field is and the larger the gyromagnetic ratio of a nucleus is, the larger the energy difference between the two quantum states becomes and, thus, the larger the magnetization becomes that can be picked up in the measurement.

The benefit of using the ^{1}H nucleus for NMR studies lies in the high natural abundance of the ^{1}H-isotope, the high hydrogen content in many carbon-based molecules as well as a comparatively large gyromagnetic ratio of the proton $\gamma_p = 2.6752 \times 10^8\,\mathrm{rad/T}$ [62].

2.3.2 Relaxation

As was stated before, a single proton can only exhibit two quantum states, $+\frac{1}{2}$ and $-\frac{1}{2}$. However, the signal picked up by the receiver coil in a classical NMR experiment obtains a response from a multitude of protons in the form of a measurable magnetization M (bold symbol as vector notation). The macroscopic evolution of the magnetization over time for an ensemble of spins can be described by

$$\frac{d\boldsymbol{M}(t)}{dt} = \gamma \boldsymbol{M}(t) \times \boldsymbol{B}(t). \tag{2.6}$$

In the frame of this work, z denotes the direction along the (horizontal) bore of the magnet, x the horizontal direction perpendicular to z, and y the vertical coordinate. The z-direction is also called the longitudinal direction, and (x, y) the transverse plane.

To suit the application of NMR measurements, the relaxation times T_1 and T_2 are introduced, and the previous equation is rewritten to yield the Bloch equations

$$\frac{dM_{xy}(t)}{dt} = -i\,\gamma\left(M_{xy}(t)\,B_z(t) - M_z(t)\,B_{xy}(t)\right) - \frac{M_{xy}}{T_2}, \qquad (2.7)$$

$$\frac{dM_z(t)}{dt} = -i\,\frac{\gamma}{2}\left(M_{xy}(t)\,\overline{B_{xy}(t)} - \overline{M_{xy}(t)}\,B_{xy}(t)\right) - \frac{M_z}{T_1}. \qquad (2.8)$$

$M_{xy} = M_x + i\,M_y$ and $B_{xy} = B_x + i\,B_y$ are the complex combination of the x and y components, and a bar over a parameter denotes its complex conjugate. T_2 is called the transverse relaxation time and T_1 the longitudinal relaxation time. The B-field is a sum of the static magnetization from the external magnetic field B_0 (z-direction) and the magnetic field applied by the RF coil used to alter the magnetic field B_1 which is applied in the transverse plane

$$\boldsymbol{B} = \begin{pmatrix} B_1\sin(\omega_0 t) \\ -B_1\cos(\omega_0 t) \\ B_0 \end{pmatrix}. \qquad (2.9)$$

The RF field (or pulse) is used to alter the magnetization present in the magnet. Depending on the strength and duration of the RF pulse, the observable magnetization is flipped at a specific angle. NMR measurements are usually carried out using sequences of these RF pulses with different flip angles. By disturbing the thermodynamic equilibrium of the sample in this defined way, a specific response is obtained, which translates into the measurement results.

The two relaxation times, T_1, and T_2, play an important role in NMR applications, as they denote how the magnetization evolves over time when not in thermodynamic equilibrium. As the duration of RF pulses is usually short in comparison to the relaxation times, a large proportion of the time the observable magnetization evolves freely. During this time where $B_1 = 0$, the solution to the Bloch equations is

$$M_{xy}(t) = M_{xy}(0)\,e^{-t/T_2}, \qquad (2.10)$$

$$M_z(t) = M_0 - (M_0 - M_z(0))\,e^{-t/T_1}. \qquad (2.11)$$

As a result, T_2 describes how fast the magnetization in the transverse plane is diminishing and T_1 how fast it rebuilds in the direction of the external magnetic field towards thermodynamic equilibrium. From a phenomenological point of view, one can say that T_1 is the time the magnetization needs after being flipped by a

$90°$ pulse to rebuild 63% of the original magnetization in z-direction. T_2 is the time after which 63% of the magnetization in the transverse plane has diminished (Figure 2.2a).

The transition of magnetization from the transversal plane back to the longitudinal direction is not the only mechanism reducing the observed M_{xy}. A second mechanism is the dephasing of different compartments in the observed volume. When the B_0-field is not constant in the volume, some parts have a higher Larmor frequency than others. From the outside, only the sum of the different compartments can be observed as the magnetization M_{xy} and when the dephasing occurs, some parts of the magnetization of each compartment get canceled out by the other. Over time, the phase difference between the compartments rises, and the transverse magnetization M_{xy} diminishes faster than its counterpart M_z rises. This effective relaxation time is called T_2^*, calculated from the reciprocal sum

$$(T_2^*)^{-1} = (T_2)^{-1} + (T_2')^{-1} \tag{2.12}$$

of T_2 and another T_2', accounting for the B_0 inhomogeneity. T_2^* is not only important when T_2 is measured. It also describes how fast the observable signal diminishes. Only M_{xy} can be picked up by the RF coil. Towards larger magnetic inhomogeneities, T_2^* becomes shorter and less time is available to observe the signal. This factor is crucial for gases and at elevated temperatures, where T_2 is already very low. For instance, hydrogen becomes completely invisible at elevated temperatures because the T_2^* drops to a few hundred microseconds which is less time than required by the hardware to switch the gradients for imaging.

2.3.3 Spectroscopy

As stated in Equation 2.5, the magnetic field strength B_0 is directly connected to the Larmor frequency, the frequency at which the nuclei exhibit resonance. However, different aspects need to be considered that change the local magnetic field strength and, thus, alter the Larmor frequency of individual spins picked up during measurement. One alteration of the local magnetic field comes from the molecules observed in the measurement. Each atom reacts to the applied external field by blocking some part of the magnetic field or, in some cases, enhancing the field around it. The change in the local magnetic field is differentiated into two different categories. Shielding effects between atoms of the same molecule are categorized as intra-molecular shielding, while the influence between two molecules is called

inter-molecular shielding. The intra-molecular shielding effects are only dependent on the molecule's structure and usually allow to distinguish between different types of chemical groups because the shielding effects are only local. The phenomenon derives its name from this effect, the chemical shift, and it is a versatile tool to find single substances in mixtures by distinguishing, e.g., methyl groups ($-CH_3$) from methylene groups ($-CH_2-$) in a hydrocarbon. When the frequency information in an MRI measurement is maintained, the chemical shift information can be displayed in a spectrum (Figure 2.2b). Therefore, it is also referred to as magnetic resonance spectroscopy or magnetic resonance spectroscopic imaging (MRSI). Higher order shielding effects exist, where a ($-CH_3$) group next to a ($-CH_2-$) group shows slightly different chemical shift than a ($-CH_2-$) group only surrounded by other ($-CH_2-$) groups. In ^{1}H-spectroscopy, shifts are generally small and, thus, a high resolution in frequency detection (and a homogeneous magnetic field) is required to resolve these in an experiment [48].

Inter-molecular shielding effects are common in liquids, where the molecules' proximity and interactions are strong. They are usually temperature dependent, which is used to acquire temperature information of a liquid like ethylene glycol [63] or water [59]. Except for reference temperature measurements performed in Chapter 4, this work only deals with MRI measurements of gaseous species. In the case of gas-phase NMR spectroscopy, inter-molecular shielding effects and, thus, temperature effects only play a minor role for the chemical shift [64] and can be neglected.
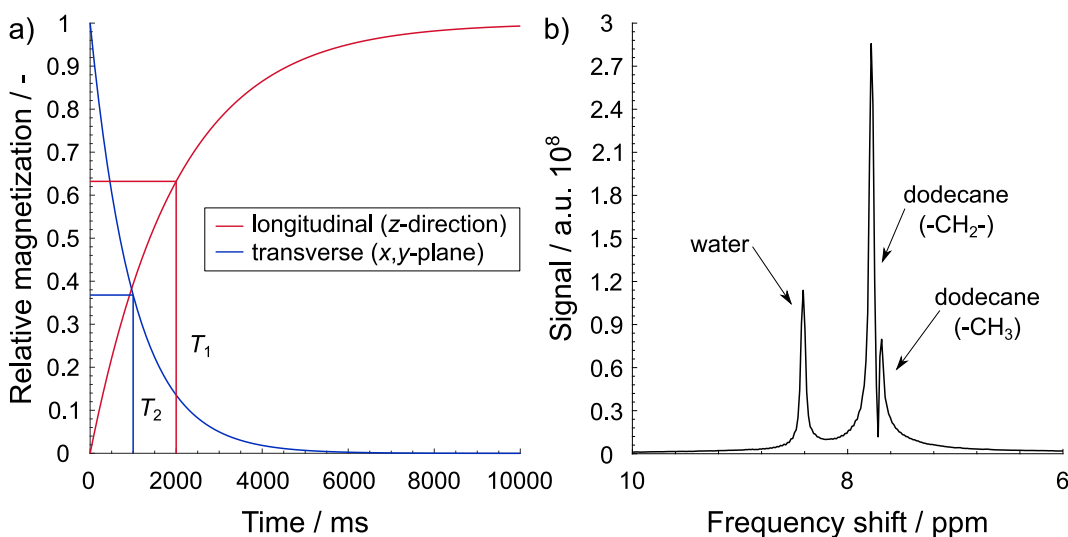

Figure 2.2: a) Illustration of the magnetization evolving over time after a 90° pulse.
b) Exemplary chemical shift spectrum of water and dodecane (absolute values).

Chemical shifts δ are usually given in ppm, where the actual shift ν_f in units of Hertz is set in relation to the applied Larmor frequency ν_{ref}

$$\delta_f = \frac{\nu_f - \nu_{ref}}{\nu_{ref}}.$$

(2.13)

Using this normalization, the results can be applied to all NMR measurements regardless of the magnetic field strength.

A remark on chemical shift spectra

Typically, the axis of the chemical shift in a graph is inverted, thus, going from right to left. In NMR spectroscopy, the chemical shift is given in reference to a substance like methane or tetramethylsilane (TMS), as the absolute frequency where a peak appears depends on many factors, such as the applied MR frequency and the local magnetic field strength. Methane is the typical reference for chemical shifts in the gas phase. As methane is present in every measurement in this thesis, the literature values given in Table 2.1 can be applied directly to the shown spectra. However, the methane signal is not set to $0\,$ppm, as is common practice in other applications of NMR spectroscopy. The magnetic field is never entirely homogeneous over the spatial directions of the different studied objects. Therefore, the position of the peaks in the spectrum is shifted from one volume element (voxel) to another. As a result, only relative peak positions can be evaluated, and the reader should focus on the signal differences given in the table, instead.

Lastly, the spectra shown in this work use the modulus or absolute of the complex values instead of its real part, which is more common in spectroscopy. The signal evaluation is not performed in the spectral domain. Therefore, it is just a graphical change. The absolute values are preferred here, as the different shapes of real value peaks due to the phase shift might confuse readers unfamiliar with NMR spectroscopy.

Table 2.1: Chemical shifts of the three gases containing hydrogen which are present during the methanation reaction. For gases the shift is commonly stated relative to methane.

Gas	Chemical shift	Literature
CH_4	0	-
H_2	4.49	[65]
H_2O	0.56	[66]

2.4 Magnetic resonance imaging

2.4.1 Gradients

MRI's core is the use of electromagnetic coils, which produce a linear magnetic field gradient in either of the three spatial directions x, y, z. Depending on their timing in a sequence, the gradient coil can be used for three different effects on the specimen. When the gradient is active during excitation or flipping of the magnetization (e.g., a 90° pulse), the pulse can be limited to a specific area of the studied object. Usually, this is used to study a single slice of the specimen. Therefore, the gradient is called the slice selection gradient. The thickness of the slice is determined by the strength of the magnetic field gradient and the bandwidth of the used pulse. The mechanism behind this is that spins can only be altered using RF pulses if the pulse frequency matches the spins' Larmor frequency (Equation 2.5). By changing the magnetic field through the gradient, the local Larmor frequency changes. Thus, only some part of the specimen can absorb the energy from the pulse and is flipped. The frequency of the RF pulse is converted into a spatial position along the magnetic gradient. The bandwidth of an RF pulse is inversely proportional to its duration. To realize a small bandwidth and, therefore, to select a thin slice, a long pulse is required. For the application in this work, using a slice selection gradient was not feasible. This is because the presence of the gradient leads to the dephasing of the magnetization, as will be discussed shortly for the phase encoding gradient. For rephasing, the gradient has to be applied in the opposite direction after the slice selection is performed (Figure 2.3). However, the rephasing has a diminishing effect when strong molecule diffusion occurs, as the applied phase depends on the spatial
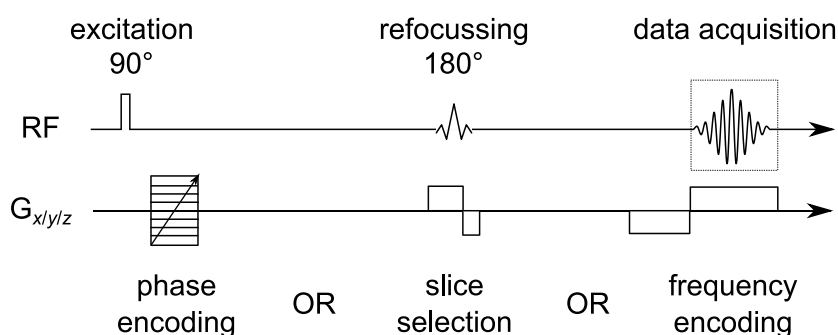

Figure 2.3: Scheme of the three different gradient types for MRI and their respective timing in a standard MRI sequence. In this work, only phase encoding gradients are used.

position. Gases exhibit high diffusion coefficients, which can lead to severe signal loss. The use of slice selection gradients is further discouraged, as very narrow timings and short pulses are required in the sequence due to the short relaxation times of the gases. Through the inverse proportionality between the bandwidth and duration of an RF pulse, the signal of fast-decaying gases like hydrogen cannot be measured using slice selection gradients.

A second way to deploy magnetic field gradients for MRI is using a read or frequency encoding gradient. As the name suggests, the gradient is deployed during the signal acquisition. Again, by changing the local magnetic field the Larmor frequency is changed such that every part in the read direction has an individual frequency during acquisition. The different frequencies present during acquisition can be obtained using the fast Fourier transform on the signal in the time domain. Even though this type of gradient has the benefit of acquiring every data point along the dimension in a single run of the sequence, the frequency is then superpositioned with the local frequency change from the chemical shift. If not corrected during the applied sequence, the spectroscopical information is lost when using a frequency encoding gradient. Further, the chemical shift can lead to imaging artifacts by shifting the position of the signal in the image along the frequency domain.

In this work, only phase encoding gradients are used. In the MR experiment, phase encoding is achieved by applying the gradient between signal excitation and signal acquisition (Figure 2.3). While the gradient is active, the local change in Larmor frequency leads to different angular speeds of the magnetization precessing in the transversal plane. As a result, the signal dephases along the gradient direction. The duration and strength of the applied gradient control the amount of dephasing. The procedure of phase encoding is described mathematically by a phase shift $\Phi(\boldsymbol{r})$, which is applied to the complex value of the signal ς. $\boldsymbol{r}$ is the vectorized spatial coordinate $\boldsymbol{r} = (x, y, z)$. As already stated, the amount of phase encoding $\Phi(\boldsymbol{r})$ depends on the duration δ of the gradient with strength $\boldsymbol{G}$, which results in

$$\Phi(\boldsymbol{r}) = \gamma(\boldsymbol{G} \cdot \boldsymbol{r})\delta. \tag{2.14}$$

However, the signal measured by the RF coil does not see just one phase shift but all the phase shifts exhibited from the different parts of the studied object. Due to the application of the gradient, each part along the gradient's axis has an individual

phase shift. Thus, the resulting signal S is a superposition of every phase shift $\Phi(\boldsymbol{r})$ applied to the original signal $\varsigma(\boldsymbol{r})$, which results in

$$S = \int \varsigma(\boldsymbol{r}) \exp(i\Phi(\boldsymbol{r})) d\boldsymbol{r}. \tag{2.15}$$

By introducing $\boldsymbol{k} = (2\pi)^{-1} \gamma G \delta$, Equation 2.15 can be inversely Fourier transformed to acquire $\varsigma(\boldsymbol{r})$

$$\varsigma(\boldsymbol{r}) = \int S(\boldsymbol{k}) \exp(-i2\pi(\boldsymbol{k} \cdot \boldsymbol{r})) d\boldsymbol{k}. \tag{2.16}$$

Thus, the original signal $\varsigma(\boldsymbol{r})$ can be calculated by applying the Fourier transform to the acquired signal $S(\boldsymbol{k})$. The downside of this type of signal encoding is that per sequence execution, only one data point from $S(\boldsymbol{k})$ is recorded. To acquire a certain number of voxels, the MR sequence needs to be repeated the same amount of times. In case of this work, where phase encoding gradients are applied in each of the three spatial dimensions, this results in an extensive measurement time. To acquire $10 \times 10 \times 40$ voxels in $x/y/z$-direction, 4000 runs of the used sequence would be necessary.

Through the step-wise acquisition of $\boldsymbol{k}$-space data, the result is not a continuous wave function but rather a grid of points in the $\boldsymbol{k}$-space, which is computed using the fast Fourier transform (FFT) to yield the different signal decays of each voxel. All measurements performed in this work use the elliptically reduced $\boldsymbol{k}$-space sampling offered by Paravision 5.1. This setting omits the outer regions of the $\boldsymbol{k}$-space (outside the largest ellipsoid that fits into the rectangular $\boldsymbol{k}$-space) as the magnetic field gradients are strongest here. Strong magnetic field gradients lead to heavy signal dephasing, only leaving noise to be acquired. By omitting these measurements, fewer sequence runs must be carried out, and less measurement time is required.

2.4.2 Field of view

An essential factor for image acquisition is the image's actual size in relation to our real world. The maximum values of $\boldsymbol{r}$ that can be acquired are called the field of view (FOV). The FOV changes depending on the number of steps in a phase

encoding direction and the gradient strength. This behavior can be derived from our previous Equation 2.16, now depicted in FFT form

$$\varsigma(\boldsymbol{r}) = \sum_{n=0}^{N-1} S(\boldsymbol{k})\exp(-i2\pi(\boldsymbol{k} \cdot \boldsymbol{r})/N), \tag{2.17}$$

with N being the number of elements of the vector $S(\boldsymbol{k})$. For a vector that depends on one parameter (here $S(\boldsymbol{k})$ depending on $\boldsymbol{k}$), the FFT is an operator that analyzes the dependency of this vector on the (oscillating) counterpart (here $\boldsymbol{r}$). However, the operator itself is dimensionless and assumes a distribution of all points contained in the vector onto a circle to emulate the continuous wave of the original Fourier transform. When performing the FFT computation, $\boldsymbol{k}$ needs to be scaled by $(N-1)/(2\boldsymbol{k}_{max})$ to meet this requirement. As a result, the FOV that can be acquired is just the scaled circle

$$FOV = \boldsymbol{r}_{max} = 2\pi\frac{N-1}{2\boldsymbol{k}_{max}}. \tag{2.18}$$

The scaling factor that defines the size of the FOV is the increment of $\boldsymbol{k}$ in each step $\Delta\boldsymbol{k} = (2\boldsymbol{k}_{max})/(N-1)$ and, subsequently, as δ is kept constant for the phase encoding gradients in our experiments, the FOV is determined by the increment of the strength of the magnetic field gradient $\Delta\boldsymbol{G}$.

For the actual experiment, it is crucial to understand this behavior of the FFT as it not only defines the size of the FOV but also what happens with an outside object. An object further away than $\boldsymbol{r}_{max}$ would have a position on the circle larger than 2π, making them appear on the part of the circle at $\Phi - 2\pi$ just on the other side of the FOV. To prevent the overlapping of signals from different positions in the specimen, choosing the FOV large enough to correctly map every signal to its original position is required. This factor is essential for the measurements in Chapter 5.1 and Chapter 6. In these measurements, leakages around the reactor tube are detected, which would overlap with the desired signal inside the tube if the FOV had not been enlarged. A larger FOV, however, increases the voxel size for a given measurement time resulting in a reduced resolution.

2.4.3 Magnetic field homogeneity

Another important factor in MRI is the assumption of a homogeneous magnetic field over the analyzed FOV. Through careful design and manufacturing, the magnetic field generated by the different coils and the magnet is usually homogeneous. However,

severe magnetic field distortions are brought into the FOV by the measured object [67]. To better understand this behavior, it is important to know that B is not just the magnetic field strength but the magnitude of the magnetic flux density. Depending on the difference between the magnetic susceptibility of the object to its surroundings and the shape of the object, the magnetic flux is either partially forced around the object or through it. As a result, the local (static) magnetic field B_0 changes, causing local changes in the resonance frequency of molecules (Equation 2.5). Even though techniques exist to minimize the effect of magnetic field inhomogeneity (e.g., spin-echo sequences), their application is limited for gases due to their low T_2 and high diffusivity. Thus, such techniques were not deployed in this work.

To counteract inhomogeneities of the magnetic field, a special array of coils is used in MRI, the so-called shimming coils. Each coil produces a magnetic field with a defined geometrical shape which can be set to different intensity levels to – in superposition with the other coils – homogenize the magnetic field in the FOV. In case of the used BioSpec 70/20 MRI system by Bruker, five shimming coils are available, which can alter the field in $[x \times y]$, $[x \times z]$, $[y \times z]$, $[z^2]$ and $[x^2 - y^2]$-direction, respectively. The gradient coils, which produce a linear magnetic field distortion, are also used such that eight different coils are available for shimming.

The Paravision 5.1 software used for data acquisition offers functions to gather shimming parameters for optimal magnetic field homogeneity. However, these are unsuitable for the special application of gas-phase MRI because of the low signal-to-noise ratio (SNR) encountered and the large inhomogeneity of the studied object. In the first studies (Chapters 4.3 & 5.1) presented in this work, the shimming was thus done using a water-filled spherical phantom (a ping-pong ball). While the shimming on this object produces excellent results, the shape and susceptibility of the ball do not resemble the actual studied MRI reactor and the objects inside it. Still, this was done as a best practice. Only in the last year, a self-made algorithm was developed that imitates the 'Mapshim' function by Paravision. The new method can be focused on a region of interest instead of using the whole FOV. Thus, it is less reliant on signal quality, as only the regions are picked where the desired signal is most prominent.

3

Experimental methods

The following chapter introduces the different technical and methodological components required to perform the measurement shown in the later chapters. Although the presented experiments differ in their respective boundary conditions and overall goals, they all share the same concept and basic components.

3.1 Technical setup

3.1.1 MRI-compatible reactor

The heart of every measurement performed in this work is a reactor specially designed to perform chemical reactions inside an MRI scanner. State-of-the-art chemical reactors are mainly built from metallic components such as stainless steel because of their excellent processability, low material prices, and high resistance to increased pressure and temperature. The latter is most important, as many heterogeneously catalyzed gas-phase reactions require temperatures of at least $150\,°C$ and pressures above ambient conditions. Further, they are usually exothermic so that temperature and pressure can rise drastically over the cause of the reaction. The requirement to

Figure 3.1: Image of the original reactor built for MRI applications and the specially designed RF coil by MRI.TOOLS. Reprinted from [1] under creative common license (CC-BY 4.0).

build a special reactor for MRI applications arises from the fact that the pulses of the RF coil are heavily disturbed by highly electrically conductive material. Further, an entirely closed stainless steel vessel of chemical reactors would act as a Faraday cage, shutting off the insight from RF pulses. Thus, new materials and concepts needed to be found that meet the requirements for the chemical reaction and MRI measurements alike.

The design of the MRI reactor was based on the tubular reactor type, a basic concept in reaction engineering. Further, the main goal was to perform measurements of the methanation reaction and the FTS inside an MRI scanner. From all this, the design of the MRI reactor was subjected to specific boundary conditions and ideas, of which an overview is given here.

- Region of interest (ROI) free of metallic materials: As fast switching magnetic fields gradients are required to obtain 3D MRI data. The ROI must be free of electrically conducting material.

- Withstand elevated pressures and temperatures: The setup must be able to withstand pressures of 30 bar, which is required for the FTS, and over 350 °C to allow measurements of the methanation reaction.

- Free of magnetic parts: Due to the strong magnets required in MR tomographs, the setup and periphery must be (almost) completely free of any magnetic materials (i.e., no magnetic material in the experimentation room).

- Outside temperature of the reactor of less than 80 °C: As the coil surrounding the outer reactor wall is sensitive to elevated temperatures, the temperature at the outermost shell of the reactor should not exceed 80 °C. The coil used in this work is intended for high-temperature usage, but other coils might only withstand an inner temperature below 50 °C.

- Outer diameter at most 111 mm: Depending on the used MR magnet and B_0 gradient system, this value might be different. The coil and reactor must fit into the bore of the MR tomograph, which limits possible space for the isolation material and a potentially larger reaction zone.

From these constraints, the reactor shown in Figure 3.1 was built. The setup is focused around a ceramic tube made of alumina (Al_2O_3), which houses the main reaction zone and, thus, the ROI of MRI studies. To reduce the possible tension on the tube during assembly and application, the ceramic tube is kept between two

flanges, only being held by one O-ring at each end. The flanges are made of titanium due to its excellent mechanical properties compared to other non-ferromagnetic metals, such as aluminum. The tube length ensures the ROI is sufficiently far from the flanges such that the titanium does not influence the measurements. A fastener keeps the flanges in place and retains the applied pressure in the axial direction. It consists of two secondary flanges wrapped around the flanges made of titanium and four custom-made fiberglass rods. To be able to fasten the rods, aluminum sleeves with threads are glued (3M Scotch-Weld DP 490, 3M Deutschland GmbH, Neuss, Germany) onto the rods. The secondary flange is made of polyamide-imide as its low thermal conductivity, compared to that of titanium or other metals, reduces heat transported in the radial direction toward the MR magnet and the RF coil. Further, the concept features a larger glass tube around the ceramic tube. The first intention to incorporate this tube was to mimic the shell of tubular reactors. Through the shell, a tempering fluid can be pumped to keep the temperature in the reaction zone at a desired level. During the design process, however, it was considered highly doubtful whether the outer temperature of the reactor could be kept below 80 °C when a fluid with approx. 200 °C flows through the shell, and almost no space remains for an isolation layer. Instead, the part inside the shell was filled with isolation material so that the reactor is operated in a (semi-) adiabatic fashion without active cooling. With the aim to share the concept of the MRI-compatible reactor, the construction files have been published openly [1], alongside performance tests of the reactor. As a part of these tests, the methanation reaction was first performed inside an MRI scanner (not shown in this work). However, the methanation reaction requires a minimum temperature of about 200 °C, which must be supplied to the catalytic bed. One of the first findings was that the comparably thick alumina tube provides high thermal conductivity in the axial direction due to its high mass. This is an issue, as heat brought in from the outside quickly dissipates towards the titanium flanges

Figure 3.2: Image of the MRI reactor with the new inlet featuring a larger tube. It is designed for frontal heating of the reaction using an unfocused laser. A detailed view of the changes between the two reactor designs can be found in Figure B.1.

of the reactor. Thus, the heat needed to be supplied locally and at a high rate. In the first experiments, the reactor was heated using the catalytic hydrogenation of ethylene. However, this method severely limited the flexibility of the experiments performed inside the reactor.

In the second stage of the design process, after the first results had been published, an unfocused diode laser was acquired, which supplies the required heat by heating the front of the catalytic bed using near-infrared radiation. To incorporate the laser into the system, the design of the MRI-compatible reactor needed to be adapted (Figure 3.2). The concept of a fluid-tempered shell was completely abandoned to make room for a large inlet opening for the radiative heat. The outer glass tube was maintained in the setup, as it has proven its worth by stabilizing the whole reactor and preventing larger torques on the alumina tube. A comparison between the original and the new reactor model is shown in Figure B.1.

3.1.2 Heating

As mentioned in the previous section, when performing heterogeneously catalyzed gas-phase reactions inside an MRI scanner, the supply and retention of heat inside the reactor is crucial. Apart from the used hydrogenation of ethylene, different methods exist to provide heat in an MRI-compatible fashion. One concept is the direct temperature control of the surrounding magnet (Sample Temperature Control, Magritek GmbH, Aachen, Germany), which eventually leads to a heated specimen. As mentioned before, most electric parts can only withstand temperatures below $80\,°C$. Thus the technique is limited to $60\,°C$. Tempering systems involving nitrogen as a temper fluid (Variable Temperature Control for NMR Probes, Bruker BioSpin AG, Fällanden, Switzerland) are commercially available. In these systems, the fluid is heated in an external unit and brought into contact with the specimen inside the MRI scanner via tubes. Nitrogen or air, however, are limited in the temperature they can provide as the heat capacity is relatively low, and high temperature gradients are required to transfer the necessary heat. In one of our previous works, we used a similar approach to heat sampling tubes inside a reactor made of glass [4]. This approach's highest possible temperature inside the MR scanner was $200\,°C$, while the air inlet was heated to over $450\,°C$. The heat dissipated through the inlet tubes or was taken up by the mantle used for cooling. To achieve higher temperatures inside the scanner, it was required to supply the heat directly to the object of interest.

As a first approach, the heat of the exothermal hydrogenation of ethylene to ethane [56, 68] was used

$$H_2 + C_2H_4 \longrightarrow C_2H_6 \quad \left(\Delta_R H^{298\,K} = -137\,kJ\,mol^{-1} \right). \qquad (3.1)$$
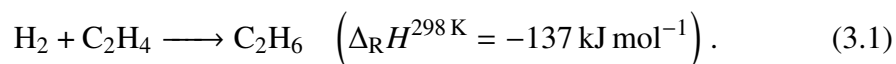
This hydrogenation is a heterogeneously catalyzed gas-phase reaction that was prior used as a model reaction to prove that MRI of the gas phase was possible [56]. Among others, the reaction had the benefit that it could be performed at room temperature over a Pt-type-catalyst. This, together with the high amount of energy being released during the reaction made the reaction an excellent candidate for the local heating inside the MRI reactor.

In the proof of concept for the CTD method, this type of heating was used to heat methane and ethylene glycol-filled glass tubes (Chapter 4.3). The heating inside the MRI reactor was successful and allowed us to perform the required study. However, a downside was that the heat of the reaction can only be controlled by changing the gas input stream. This is unfavorable in application with the methanation reaction as it is a competing reaction, and might change the reaction behavior inside the reactor. Further, the gases are visible by ^{1}H MRI and can influence the results by adding additional signals to the results of the measurement.

The second concept used in this work to heat the inside of the MRI reactor is the employment of an unfocused laser. The light emitted from the laser is sent directly onto the studied object. Therefore, the actual heat is only present at the very center of the reactor where it is needed. The laser used for this is a 500 W diode laser (LDM, LKK-D; Laserline GmbH, Mülheim-Kärlich, Germany) intended for industrial applications.

Usually, a complete laser device consists of the light emitting unit, an optical fiber, a collimator, and the focus lens. The light emitting unit includes the cooling, electrical control, and outside communication. From here, the coherent light is guided via the optical fiber to the collimator and the focus lens. When exiting the optical fiber, the light beam has a conical shape, thus widening over the distance. To prevent this behavior, the collimator is used to parallelize the light, which is focused to a tiny dot using the lens. In this application, only a semi-local heating is desired to heat the entire sample in the reactor and not just a single spot. Therefore, only a collimator without a lens is used at the end of the fiber. As the light is parallelized, the shape of the light beam is almost unchanged over the traveling distance, and the collimator can be placed at a larger distance to the object of interest which needs to be heated.

Thus, the collimator can be positioned outside the MR magnet and does not need to feature a special design.

Table 3.1: Overview over the usage of different peripheral devices in each measurement referring to the connection scheme of Figure 3.3.

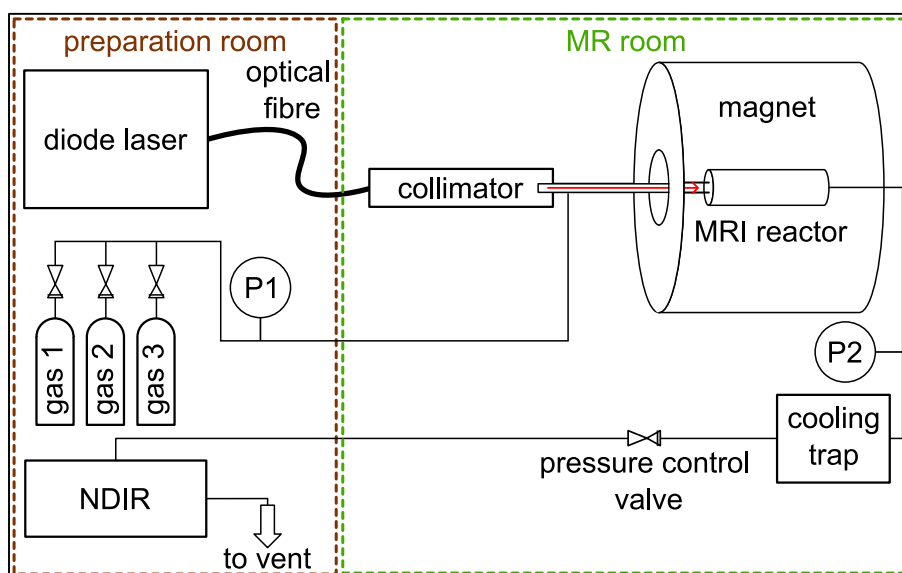| Measurement	Gases	Pressure Sensors	Heating	Cooling Trap	NDIR Spectrometer
Proof of concept CTD	$H_2/C_2H_4/N_2$	yes / no	reaction	no	no
Cross section σ_{j,CH_4-H_2}	$H_2/CH_4/N_2$	yes / no	laser	no	no
Cross section σ_{j,CH_4-H_2O}	-/-/N_2	yes / no	laser	no	no
Methanation reaction	$H_2/CO_2/CH_4$	yes / yes	laser	yes	yes

Figure 3.3: Connection scheme of the peripheral devices used for the measurements in this work. An overview of which device was used in which measurement is given in Table 3.1. Most peripheral devices had to be placed inside the neighboring preparation room to stay outside the 0.5 mT line.

3.1.3 Peripheral devices

A number of different devices and features has been used for up and down-stream processing of the gases involved in the different measurements. The positioning of the peripheral devices in the setup can be found in Figure 3.3, and Table 3.1 refers the usage of the devices to each measurement.

- **Mass flow controllers** (MFC; Bronkhorst Deutschland Nord GmbH, Kamen, Germany) have been used to control the volume flow into the reactor. The flow controllers can be used in a range of approximately $0.15\,\text{L}\,\text{min}^{-1}$ to $6\,\text{L}\,\text{min}^{-1}$ and were calibrated for H_2, CO and N_2, respectively. The CO-calibrated MFC was usually used for the carbon source of the process, thus, either C_2H_4 or CO_2. During the methanation reaction, the N_2-calibrated MFC was used for CH_4 as it represented the inert gas in the reaction.

- **Pressure sensors** (WIKA Alexander Wiegand SE & Co. KG, Klingenberg, Germany) were used to quantify the pressure inside the reactor. In all measurements except the methanation reaction, a single pressure sensor directly after the MFCs was used. For the methanation, it was necessary to ensure that the pressure drop over the reactor is known. Therefore, a second pressure sensor was placed right before the cooling trap.

- A **pressure control valve** (Hy-Lok D Vertriebs GmbH, Oyten, Germany) was used when a gas pressure above ambience was required inside the MRI reactor. The used valve sets a counter pressure by manually screwing a spring onto a polytetrafluoroethylene (PTFE) seat which blocks the gas flow if the pressure inside the reactor is below a certain threshold. As the knob of the valve needed to be turned manually, and it needed to be placed inside the MR room, the valve was usually set at the beginning of the measurement and then left at a certain position. This could result in small changes in the final pressure from the initial setting when the gas flow had adjusted to the combination of MFC flow control and pressure control valve. In the presented measurements, this was not an issue, as the actual pressure was known through the pressure sensors, and it was possible to account for the change in the calculations.

- A **non-dispersive infrared spectrometer** (NDIR) was used to quantify the molar concentrations of CO, CO_2 and CH_4 in the outlet stream during the methanation reaction. The NDIR spectrometer (GMS810 with a MULTOR module, Sick AG, Germany) is equipped with three different modules, one for

each gas. The spectrometer sequentially measures the gas concentration of one of the three gases for about 15 s and then switches to the next. As a result, the values are updated with a temporal resolution of approximately 45 s.

- A **cooling trap** was built to remove the water from the product stream that is created in the methanation process. This was necessary, as no water is allowed in the NDIR spectrometer used for gas analysis. The cooling trap was cooled to a temperature of $0\,°C$ by keeping the trap in a bath of ice and water. The cooling trap was a makeshift build using some larger Hy-Lok tubings (Hy-Lok D Vertriebs GmbH, Oyten, Germany) which were made from stainless steel. It was placed in front of the pressure control valve, so that the gas entering the valve was dry and no condensation occurred inside the valve.

3.2 MRI Measurements

3.2.1 Scanner

A 7 Tesla preclinical NMR imaging system (Biospec 70/20, Bruker Biospin GmbH, Ettlingen, Germany) equipped with a gradient system BGA12S2 ($441\,mT\,m^{-1}$ maximum gradient strength in each direction, $130\,µs$ rise time) was used for all MRI measurements. A circularly polarized volume RF coil was used for RF excitation and signal detection. The pulse sequences were implemented using the software platform Paravision 5.1.

3.2.2 Coil

A special MRI coil was built for the experimental setup. The coil was developed and manufactured by MRI.Tools GmbH (Berlin, Germany) using a ring-shaped cylindrical fiberglass body with an inner diameter of $72\,mm$. Its special feature are four cylindrical bores distributed evenly on the ring. The bores make room for the fiberglass rods to go through the body of the coil (see Figure 3.1). Furthermore, connections for pressurized air were added at the front to cool the coil *in situ* through thermal convection. Compared with previously used standard RF coils, the dedicated RF coil built by MRI.Tools exhibits reduced background signals and considerably reduced detuning of the RF coil with changing temperature, both essential properties for the presented measurements.

3.2.3 3D-MRSI measurements

An optimized short echo time MRSI pulse sequence was used to acquire spectral information of the MRI reactor with a 3D resolution. The sequence uses a RF pulse with a flip angle of 20° to partly flip the magnetization into the transverse plane. Immediately after the RF pulse, short triangular-shaped phase encoding gradients were applied with circularly reduced k-space sampling (see Chapter 2.4). In between the RF pulse and data acquisition of the free induction decay (FID), a wait time of T_E passes to allow for sufficient gradient rise times. Data acquisition was performed using 1024 complex data points and a spectral width of 50 kHz. Using a repetition time (T_R) of 80 ms, the total time per MRSI measurement was about 9 min.

3.2.4 T_1 measurements

To measure the signal amplitude A (as a measure of M_0) and the relaxation time T_1, a pulse sequence was used that combined a saturation module with the 3D-MRSI sequence. To reduce the influence of spatial inhomogeneities or maladjustments of the B_1 field used for RF pulses, the saturation module consisted of two consecutive 60 µs rectangular 90° pulses with a delay of 0.8 ms to flip the magnetization into the transverse plane. Each pulse is followed by spoiler gradients to destroy the longitudinal magnetization. After a recovery time τ, a third 60 µs rectangular 90° pulse is used to flip the partially rebuilt longitudinal magnetization into the transverse plane again. Immediately after the RF excitation pulse phase encoding gradients
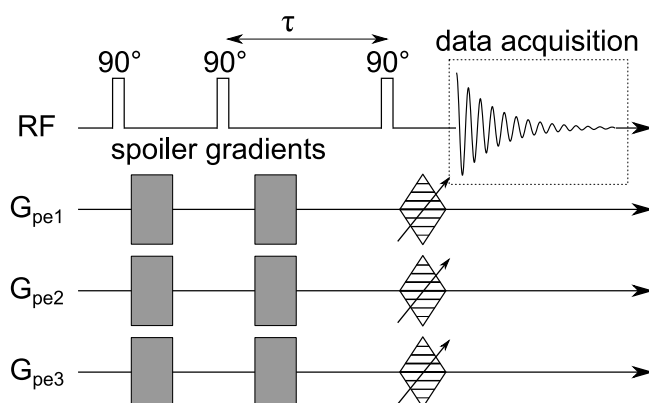

Figure 3.4: Scheme of the saturation recovery sequence used to measure the longitudinal relaxation time T_1 and signal amplitude A. The phase encoding gradients are shown as triangles emphasizing that the gradient duration is short in comparison to the rise time of the gradient system. Reworked from [2] under creative common license (CC-BY 4.0).

of 260 µs duration are applied in all three spatial dimensions, followed by data acquisition (50 kHz spectral width, 1024 complex data points, Figure 3.4).

The recovery time τ was varied to cover the T_1 relaxation progress of methane. The lowest value was always 0.8 ms and the highest value was chosen to be around 3 times of the expected T_1. Each step of τ in between was about double the prior value. A detailed overview of the chosen parameter for each measurement can be found in Table 3.2.

For each τ value a single 3D-MRSI measurement was performed, resulting in one decaying time signal (FID) for each τ value and each voxel. From the FIDs, signal amplitudes S were determined using the matrix-pencil method (MPM) as described by Lin et al. [69]. The method presents a fast way to fit exponentially decaying signals in the time domain. In comparison to integration in the spectral domain, MPM's ability to separate signals even with low frequency differences (< 0.5 ppm) was advantageous for our measurements, as the different resonance lines are usually too broad to be separated clearly. Further, the MPM fits provide information about the frequency, dampening factor and phase of the signal helpful for further analysis. In Chapter 6.3, for instance, the dampening factor could be used to separate the signal of liquid water from the remaining signals.

From the MPM fits, series of amplitudes S per voxel were determined. The amplitudes were fitted to the function

$$S = A + (C - A)\mathrm{e}^{-\tau/T_1}, \tag{3.2}$$

using the 'trust-region-reflective'-algorithm provided by MATLAB (mathworks.com, Version 2017b). The fitting parameters are the maximum signal amplitude A, the longitudinal relaxation time T_1 and an error term C, which accounts for incomplete saturation of the longitudinal magnetization, e.g., by misadjustment or spatial inhomogeneities of the RF field. A graphical depiction of the processing from FID to signal amplitude and T_1 can be found in Figure B.4 in the appendix alongside the effects of magnetic field inhomogeneity discussed in Chapter 2.4.3.

The FOV of the measurement was always chosen to be as small as possible to reduce measurement time. It can be seen in Table 3.2 that the size of the FOV differs for the measurements even though the same MRI reactor was studied. This is because some leakage occurs between the ceramic tube and the glass tube. Even though this did not pose a security threat, the accumulation of gases outside of the ceramic tube influences the measurement signal. To prevent the signal from influencing the measurement inside the reactor, a larger FOV needed to be chosen. In the

measurements of Chapters 4 and 5.2 the measured methane was inside glass tubes. Here, the most prominent gas was nitrogen. Therefore, a small FOV could be chosen. For future studies, a rework of the sealing of the reactor might be necessary.

Table 3.2: Overview over the different parameters used for the (series) of 3D-MRSI measurements.

Measurement	FOV / mm^3	Voxels	Acquisition time	Sequence
Proof of concept CTD Chapter 4	37.5×37.5×105	25×25×21	37 min	Saturation Recovery τ/ms $\in$ {80, 50, 30, 20, 12, 6, 0.8}
Parameter identification σ_{j,CH_4-H_2} Chapter 5.1	50×50×105	25×25×21	22–90 min	Saturation Recovery τ/ms $\in$ [0.8, 300]
Parameter identification σ_{j,CH_4-H_2O} Chapter 5.2	31.5×31.5×125	21×21×25	70 min	Saturation Recovery τ/ms $\in$ {450, 150, 80, 40, 20, 10, 6, 3, 0.8} τ/ms $\in$ {300, 150, 80, 40, 20, 10, 6, 3, 0.8}
Methanation Chapter 6	57×57×123	19×19×41	90 min 9 min	Saturation Recovery τ/ms $\in$ {300, 150, 80, 40, 20, 10, 6, 3, 0.8} 3D-MRSI flip angle: 20°; T_R: 80 ms

4

Method development: Combined Temperature and Density (CTD) measurements

This thesis is centered around the question, how heterogeneously catalyzed gas-phase reactions can be analyzed using MRI to better understand the complex interactions of different transport phenomena. To answer this nontrivial question, a new method was developed. It is called the Combined Temperature and Density (CTD) method. The CTD method depends on the translation from NMR parameters to reaction parameters, and more specifically, from signal amplitude A and T_1 relaxation time to temperature T and molecular number density ρ. This chapter elucidates the general idea behind the method, presents the equations and theorems required for the application of the method, and shows the method's proof of concept. The findings presented here have previously been published in Harm Ridder, Christoph Sinn, Georg R. Pesch, Wolfgang Dreher, and Jorg Thöming. "Spatially resolved direct gas-phase thermometry in chemical reactors using NMR". in: *Chemical Engineering Journal* 433.September 2021 (2022), p. 133583. DOI: 10.1016/j.cej.2021.133583.

4.1 The CTD method

As previously explained, chemical reaction systems are subject to complex transport phenomena. To better understand how a system reacts to potential optimizations, local reaction parameters like temperature and concentration need to be acquired *operando*. MRI allows to perform *operando* measurements of reactors. Among others, the acquired NMR parameters like signal amplitude, T_1, and T_2 depend on the temperature T and the molecular number density ρ (e.g., the number of

molecules contained in a given volume) of the different species. Thus, the two reaction parameters T and ρ can be measured using MRI. However, while other influences on the NMR parameters might be kept constant during a measurement, T and ρ cannot. Thus, measuring a single NMR parameter alone does not allow to derive the two local parameters T and ρ. A change in the measured NMR parameter might always be induced by either one of the two parameter, and more likely, a combination of both. To resolve the issue of the twofold dependence on T and ρ, two different NMR parameters need to be acquired, preferably from the same measurement.

The application of the CTD method in this thesis is based on a saturation recovery sequence. Saturation recovery sequences are commonly used to acquire the longitudinal relaxation time T_1 of a species by measuring the signal recovery after saturating the studied sample. However, T_1 cannot be derived from a single measurement alone, but a fit over multiple measurements with different wait times τ is required (see Chapter 3.2.4). Through this fit, not only T_1 is acquired, but also the maximum signal amplitude A of the species – a fact that is usually ignored. Thus, the saturation recovery offers two independent and simultaneously measured NMR parameters.

4.2 From NMR parameters to reaction parameters

To calculate temperature T and molecular number density ρ from signal amplitude A and longitudinal relaxation time T_1, the temperature and density dependence of the two NMR parameters needs to be known. In the following, the dependences are derived from theory, and then combined to suit the calculation of T and ρ. It is important to note that the resulting values are calculated as absolute quantities. Apart from some signal bleeding that is encountered in every MRI measurement, each individual voxel carries its unique set of temperature and density information of the methane therein. While this feature is inherent in multiple MRI sequences applied in reaction engineering, it is uncommon in medical MRI applications. For further analysis of the results, such absolute values are crucial. From absolute temperatures, for instance, one can calculate local reaction rates, which would not be possible from a qualitative image. However, the validation process for absolute values is much more complex. An image does not only need to make sense qualitatively, but ways need to be found to validate the acquired local information in each voxel.

4.2.1 Signal amplitude

As shown in Chapter 2.3.1, the dependence of the signal amplitude on temperature is characterized by the Boltzmann distribution and depends on the excess of spins that align to the magnetic field. Using the relation $\tanh(z) = (\exp(2z) - 1)/(\exp(2z) + 1)$, Equation 2.3 can be rewritten to

$$A = C\rho_i V S_m \tanh(z) \quad \text{with} \quad z(T) = \frac{\gamma \hbar B_0}{2k_B T}, \tag{4.1}$$

with the average molecular density in the observed volume $\rho_i = N_i/V$ of component i. When the signal amplitude is compared to a known state, for instance at room temperature (index 0), the dependence on measurement parameters in C can be removed and the equation now reads

$$\frac{A}{A_0} = \frac{\rho}{\rho_0} \frac{\tanh(z(T))}{\tanh(z(T_0))}, \tag{4.2}$$

For simplification, we can approximate $\tanh(z) = z$, which results in a negligible error ($< 1\,\%$) at $B_0 = 7\,\mathrm{T}$ and for temperatures $T > 5\,\mathrm{K}$, resulting in

$$\frac{A}{A_0} = \frac{T_0}{T} \frac{\rho}{\rho_0}. \tag{4.3}$$

4.2.2 Longitudinal relaxation time of methane

The temperature and density dependence of the T_1 relaxation time of gases has been widely studied by different authors in the past [70–75]. T_1 of gaseous methane is mainly dependent on the spin-rotation mechanism [71, 74]. The topic was experimentally covered by the studies of, for instance, Dong and Bloom [75] or Beckmann [72]. The generalized formula of the spin-rotation mechanism stated by Dong and Bloom is

$$T_1^{-1} = \frac{4\pi^2}{\hbar^2} C_{\mathrm{eff}}^2 2 I_0 k_B T \frac{\tau_1}{1 + \omega_0^2 \tau_1^2}. \tag{4.4}$$

Here, C_{eff}^2 is the effective spin-rotation constant for spherical top molecules

$$C_{\mathrm{eff}} = C_a^2 + \frac{4}{45} C_d^2, \tag{4.5}$$

with the constants for methane $C_a = (10.4 \pm 0.1)\,\mathrm{kHz}$ and $C_d = (18.5 \pm 0.5)\,\mathrm{kHz}$ [76], the angular rotational frequency $\omega_L/2\pi = 1.68\,\mathrm{MHz}$ [72] and the principal

moment of inertia $I_0 = 5.33 \times 10^{-47}\,\mathrm{kg\,m^2}$ [77]. The variable τ_1 is a characteristic time, sometimes described as the mean time between two consecutive molecule collisions

$$\tau_1 = (\rho\sigma_j\bar{v})^{-1}, \tag{4.6}$$

using the average molecular density ρ, the mean relative gas velocity [72] with the reduced mass of the colliding pair $\mu = (m_1 m_2)/(m_1 + m_2)$

$$\bar{v} = \sqrt{\frac{8k_B T}{\pi\mu}}, \tag{4.7}$$

and the effective cross section for the collision of each methane molecule σ_j. When multiple gases are present, the definition of τ_1 and σ_j needs to be extended to account for the different possible collision partners. According to the theoretical work by Gordon [78], τ_1 can be calculated as the sum of molecular density ρ_i of the collision partner i multiplied by their respective mean relative gas velocity $\bar{v}_i$ and the cross section for the collision of methane with that specific molecule σ_{j,CH_4-i}

$$\tau_1^{-1} = \sum_{i=1}^{n} \rho_i \bar{v}_i \sigma_{j,CH_4-i}. \tag{4.8}$$

The cross sections for the collision of methane with other gases are not commonly known and need to be calculated from measurements. Unfortunately, σ_j is not only different for each molecule, but also temperature dependent and, thus, needs to be quantified in an extensive measurement series, including changes in the temperature. In Chapter 5, the different cross sections required for the methanation reaction are discussed further.

4.2.3 Iterative calculation of temperature and density

From the theoretical analysis it can be derived that both signal amplitude A and longitudinal relaxation time T_1 are described by a function of density and temperature. To find a solution for ρ and T that fits a pair of amplitude and T_1 in each respective voxel, Equations 4.3 and 4.4 are computed iteratively.

For the calculation of temperature and density, assumptions are required, which vary for different cases of applications. In the measurements shown in this work, methane is measured either inside glass tubes or in an open reactor system, where the methane and other gases constantly flow through the reactor tube. Four different

molecular number densities must be considered in the measured framework. The number density of methane during the base measurement $\rho_{CH_4,0}$ and the molecular number density of all molecules in this state $\rho_{tot,0}$, as well as the molecular number density during the actual measurement ρ_{CH_4} and the corresponding overall molecular number density in this second state ρ_{tot}.

The overall molecular number density is calculated using the ideal gas law and the Avogadro constant $N_A = 6.022 \times 10^{23}$ mol^{-1}

$$\rho_{tot} = \frac{p N_A}{R T}. \tag{4.9}$$

As methane is measured in this work, Equation 4.3 only applies to the molecular number density of methane and needs to be specified as

$$\frac{A}{A_0} = \frac{T_0}{T} \frac{\rho_{CH_4}}{\rho_{CH_4,0}}. \tag{4.10}$$

The molecular number density is a quantity that cannot be applied directly to typical reactor models. Therefore, the iterative calculation method computes the mole fraction of methane x_{CH_4} from the signal amplitudes

$$x_{CH_4} = \frac{\rho_{CH_4}}{\rho_{tot}} = \frac{\rho_{CH_4,0} \frac{T}{T_0} \frac{A}{A_0}}{\rho_{tot}}. \tag{4.11}$$

In the quantification of σ_{j,CH_4-H_2} (Chapter 5.1) and the methanation reaction (Chapter 6), an open reactor system is used. Methane flows openly through the reactor and a constant pressure is set using the pressure control valve. For the proof of concept of the CTD method (Chapter 4.3) and the quantification of σ_{j,CH_4-H_2O} (Chapter 5.2), methane inside glass tubes is measured. Inside the closed tubes, the number of molecules stays constant. Therefore, it can be assumed $x_{CH_4} = 1$. Even though the overall number of molecules in a tube is constant, the molecular number density can be slightly shifted through temperature gradients over the tube length. This error is accounted for by calculating the ratio between the initially equally distributed density at room temperature and the actual density

$$\frac{\rho}{\rho_0} = \frac{T}{T_0} \frac{A}{A_0}, \tag{4.12}$$

and applying the ratio to x_{CH_4} when used as an input for the temperature calculation. In the case of an open reactor system, the calculation is different. Here, the mole

fraction at the base measurement $x_{CH_4,0}$ is set using mass flow controllers. Using $\rho_{CH_4,0} = x_{CH_4,0} \, \rho_{tot,0}$, Equation 4.11 is changed to

$$x_{CH_4} = \frac{x_{CH_4,0} \, \rho_{tot,0} \, \frac{T}{T_0} \, \frac{A}{A_0}}{\rho_{tot}} = x_{CH_4,0} \frac{p_0}{p} \frac{T^2}{T_0^2} \frac{A}{A_0}. \tag{4.13}$$

The second part of the CTD iteration process calculates the temperature of the measured methane from T_1 using Equation 4.4 by Dong and Bloom [75]. As explained in the previous chapter, to calculate the characteristic time τ_1 from Equation 4.8, the molecular number densities and cross sections for the collision of methane with the respective molecule need to be considered. In binary mixtures, quantifying the molecular number densities of each species can be done by measuring the applied pressure or quantifying the signal ratio between two gases. However, the gas mixture's characterization is less straightforward when dealing with the actual methanation reaction. In this case, gas mixtures are dependent on mass transport as a combination of diffusion, convection, and reaction processes. For simplification, diffusion was neglected. Thus, the gas mixture's composition is only a function of the extent of reaction. According to Equation 2.1, for each mole of methane formed, two moles of water are formed, while four moles of hydrogen and one mole of carbon dioxide are consumed.

The iterative method calculates the temperature and density in each voxel independently using the equations described above. The iteration stops when a local minimum is found, e.g., when the change per calculation step falls below a certain threshold. If no solution is found in a given range of feasible solutions, the value is set to not a number (NaN) and ignored for the remaining calculations. As Equation 4.3 has a linear dependence on the density, and the dependence of T_1 on the temperature is (at least in the investigated range, see Figure 6.2) monotonically decreasing, the local minimum should always be the global minimum.

4.3 Proof of concept: comparison with state-of-the-art temperature measurements

4.3.1 Experiment

As a first approach to show the applicability of the CTD method, the temperature of pure methane (quality 3.7, Linde GmbH, Pullach, Germany) was measured in

sealed glass tubes (inner diameter 3 mm, outer diameter 5 mm, Glaskomponenten / Roland Zein, Ingelsheim, Germany). The glass tubes are beneficial, as only temperature effects change the signal response of the methane. At room temperature, the pressure inside the glass tubes was approximately 0.9 bara, varying slightly for each glass tube as a result of the filling procedure. As a reference, glass capillaries (inner diameter 0.5 mm, outer diameter 0.7 mm, CM Scientific Ryefield (EU) Ltd., Republic of Ireland) filled with glycerol were placed next to the glass tubes to measure the temperature using diffusion weighted-MRI (DW-MRI) as shown in [4]. During the experiment, two methane-filled glass tubes and two glycerol-filled glass capillaries were placed inside the MRI reactor. The containers were mounted next to each other on a carrier made of polyamide-imide with alternating filling of the substances (Figure 4.1). The carrier was equipped with two MRI-compatible fiber optic temperature sensors (gallium arsenide-based fiber sensor TS2 comprehensive with FOTEMP 4; Weidmann Electrical Technology AG, Rapperswil, Switzerland), displaying the temperature at each end of the carrier. The inlet temperature sensor was placed at a distance of approximately 8 cm of the magnet's center while the outlet temperature sensor was 4 cm behind the center. A Pt/Al_2O_3-wash coated honeycomb was placed in front of the carrier and used to heat the setup by catalyzing the hydrogenation of ethene.

During the measurements, a total gas flow of 2 NL/min was set using mass flow controllers (Bronkhorst Deutschland Nord GmbH, Kamen, Germany). To achieve different temperatures inside the reactor, the ratio between the two reactants (C_2H_4, H_2) and the inert gas (N_2) was varied, ranging from 0.1/0.1/0.8 ($C_2H_4/H_2/N_2$) for the lowest temperature to 0.27/0.27/0.46 for the highest temperature. MRI measurements were started at steady state conditions, i.e., when both fiber optic

Table 4.1: Overview over the resulting inlet and outlet temperatures at each set point of gas compositions.

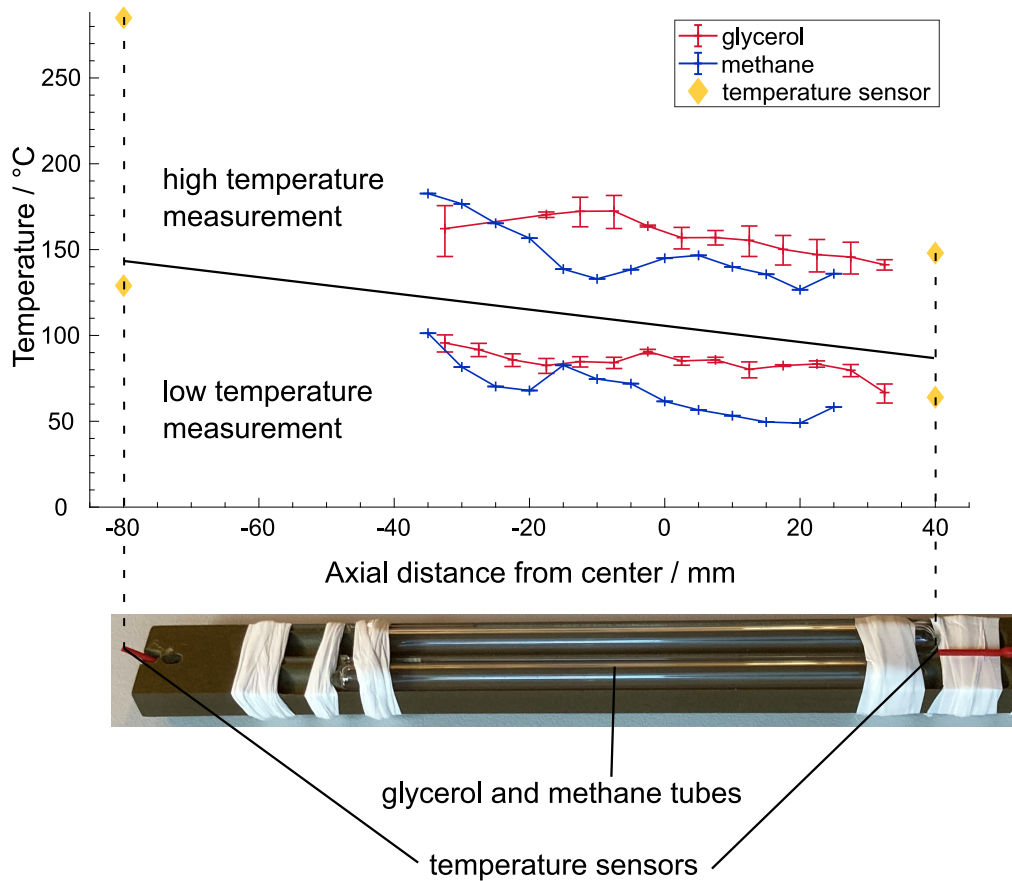| Mole fraction $C_2H_4/H_2/N_2$	Inlet temperature / °C	Outlet temperature / °C
0.1/0.1/0.8	129	64
0.16/0.16/0.68	165	84
0.18/0.18/0.64	209	108
0.22/0.22/0.56	242	125
0.24/0.24/0.52	258	136
0.27/0.27/0.46	285	148

Figure 4.1: Exemplary comparison between temperatures measured using a methane tube (CTD) and a glycerol tube (Diffusion). Reference temperature measurements using external sensors are shown as well.
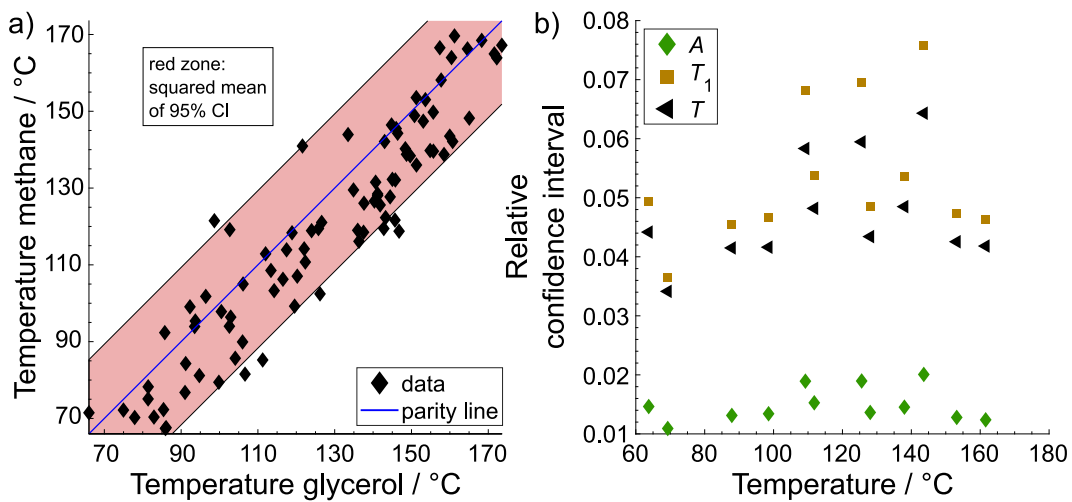

Figure 4.2: a) Parity plot of the temperature obtained from state-of-the-art DW-MRI measurements (glycerol) with the temperature measured using the CTD method (methane). b) Comparison of the methane temperature's relative CI (95 % CI divided by mean) with the relative CI of the two inputs, A and T_1. Reprinted from [2] under Creative Common License (CC BY 4.0).

temperature sensors exhibited changes in temperature less than $0.1\,\mathrm{K\,min^{-1}}$, resulting in a maximum temperature change over the cause of the measurements of 3 K.

4.3.2 Results

Measurements comparing the CTD and state-of-the-art DW-MRI method have been carried out at six different temperature levels (Table 4.1). The inlet/outlet temperature measured by the fiber optic temperature sensors at the lowest level was $T_{in} = 129\,°C$ / $T_{out} = 64\,°C$, and at the highest temperature $T_{in} = 285\,°C$ / $T_{out} = 148\,°C$. Prior to heating the setup, measurements at room temperature were carried out, which are used as a reference for the signal amplitude ratio A/A_0 and to quantify the absolute pressure inside the methane-filled tubes. From each measurement, the central eight slices were evaluated (slices 7–14). For both methane capillaries, 4×2 voxel per slice ($4.7\,\mathrm{mm} \times 2.3\,\mathrm{mm}$) were evaluated, each resulting in an individual value for T_1 and A/A_0. From these, the temperature T and the shift in molecular number density ρ/ρ_0 (Equation 4.12) were calculated as described in the previous section. The fitting procedure also calculates the 95 % confidence intervals (CI) of T_1 and A for each voxel. Furthermore, the temperature of the glycerol capillaries was calculated using a diffusion/temperature correlation (Equation 17 in [4]) from 6×6 voxel ($3\,\mathrm{mm} \times 3\,\mathrm{mm}$) of the DW-MRI measurement. All 95 % confidence intervals shown in the plots in this section are mean squared confidence intervals averaged from the respective voxels and calculated via error propagation.

To contextualize the results, Figure 4.1 shows the mean temperature (i.e., the temperature in each slice) as a function of axial distance for the outer methane-filled tube and the neighboring glycerol-filled capillary at the highest and lowest temperature level. Further, the mean temperature over the cause of the measurements of the two fiber optic temperature sensors is displayed. At first glance, it is apparent from the figure that the obtained temperatures are in reasonable agreement with each other. The measured temperatures decrease from the front to the back of the carrier, which was expected as the gas used for heating should have an axial temperature gradient, even at a steady state. However, the temperature measured using methane is always slightly lower than the glycerol temperature, whereas the fiber optical sensors display a temperature slightly above the glycerol temperature.

Results combined for all six measurements at different temperature levels are shown in Figure 4.2. Here, the mean of the methane temperature per slice is compared to the temperature measured in the glycerol-filled glass containers (a), and the relative

CI (95 % CI divided by the mean) of the measured methane is shown (b). The parity plot in Figure 4.2 a) solidifies that the measured temperature follows the same trend for both techniques. However, it also shows the methane temperature's offset to the temperature of the glycerol measured using DW-MRI. This constant offset indicates that the primary source of error does not come from statistical or SNR errors but from some systematical error during the measurement or the post-processing procedure. Figure 4.2 b) confirms this assumption, as the CI of the temperature relative to its value is only up to 6 %, while the error compared to glycerol is much larger. From the comparison of the different CIs of A, T_1 and T it can be seen that the deviation of T_1 mainly governs the CI of the temperature.

In retrospect, this indicates bad shimming of the magnetic field inside the glass tube. As mentioned in Chapter 2.4, large gradient coils are used to homogenize the magnetic field inside the measured specimen. However, Bruker's original procedure for this is not designed for the application on gases. Therefore, the magnetic field was shimmed prior to the measurements using a spherical water-filled phantom. Neither did the phantom incorporate the used MRI reactor nor the actual carrier with the glass containers. The shimming was thus only done poorly. When the magnetic field inside a voxel is inhomogeneous, the signal decay of the FID is not adequately fitted using MPM as it assumes a Lorentzian (exponential) decay of the signal, which is compromised when the shim is bad (Figure B.4). T_1 and A are fitted from a series of signal amplitudes calculated from multiple measurements using MPM. When only some of these signal amplitudes are over or under-predicted in comparison to the others, this will have a strong influence on T_1. T_1 is fitted in an $\exp\left(\frac{1}{T_1}\right)$ term, where small changes in the curve's steepness result in significant changes of the fitted value. The maximum signal amplitude A, however, has its main influence from the measurements at the highest τ and is not as susceptible to fitting errors. Another factor that needs to be considered is the low pressure inside the methane-filled tubes. Firstly, the low pressure results in a low SNR of methane (around 10-15 @50 kHz; SNR: signal amplitude versus noise at $t \to \infty$), meaning that at increased temperatures and for small τ values the results of both T_1 and A are less reliable. Secondly, the pressure range around ambient pressure is unfavorable for the T_1 of methane at a Larmor frequency around 300-400 MHz [2, 72]. In this range, the values for T_1 are close to a local minimum, meaning that T_1 only reacts with minor changes to changes in temperature and pressure (Figure 6.2). This unpronounced temperature dependence leaves the method vulnerable to deviations. Furthermore, the setup on the carrier was tightly packed to minimize temperature

gradients along the object. However, the optical fiber sensors must stick out of the carrier to work correctly. From experience with later experiments, it is apparent that the gas flow around the carrier is subject to large temperature gradients. Through natural convection effects, warmer gas flows fast along the upper regions of the free gas phase, which might explain the high temperature determined by the fiber optical sensors. Additionally, the proximity of glycerol- and methane-filled containers did not benefit the measurements of methane. The high signal of the liquid glycerol did partly appear in some of the voxels where methane was present due to the point-spread function [79]. Even though only a small portion of the glycerol signal appeared in the neighboring voxels, it was still in the same order of magnitude as the methane signal. Further, it appeared in a similar range of the chemical shift such that some of the voxels were not available for processing the methane's temperature.

Summarizing the first results using the CTD method, it is clear that the technique can measure the temperature of methane in this simplified setup spatially resolved. The results are in reasonable agreement with reference temperature measurements. As the measurements rely on methane, no temperature limits due to evaporation hinder the measurement at high temperatures. Further, the temperature can be quantified directly in the free gas phase without disturbing the gas flow.

Parameter identification: cross section for the collision of methane

The previous chapter explained how individual information about temperature and density inside a chemical reactor can be probed using MRI measurements and the proposed CTD approach. To acquire the two reaction parameters T and ρ, the signal amplitude A and the longitudinal relaxation time T_1 of methane are measured. Using the chemical shift, the signal amplitude of methane is separated from other signals present during the methanation (e.g., water and hydrogen), making the acquisition of the signal amplitude relatively straightforward. However, the longitudinal relaxation time T_1 of methane relies not only on the methane's temperature T and its molecular number density ρ_{CH_4}, but also on the molecular number density of the other gases present in the mixture. The T_1 relaxation time states how fast spins/molecules dissipate their magnetization to the surroundings. For gases in a continuum, this exchange is mainly dependent on molecule-molecule collisions. Therefore, the interaction parameter to calculate the longitudinal relaxation of methane in the presence of other gases is the cross section for the collision of methane with another molecule σ_{j,CH_4-i}. To be able to calculate T_1 of methane during the methanation reaction, the cross section for the collision of methane with each of the four participants of the reaction, hydrogen, carbon dioxide, water, and methane, are required. In many cases, nitrogen is present to dilute the gases and control the reaction. The cross sections for the collision of methane with methane, carbon dioxide, and nitrogen have already been determined by Jameson et al. [76]. Jameson et al. stated the cross sections as a temperature-dependent parameter in the form of

$$\sigma_{j,CH_4-i} = \sigma_{0,i} \left(\frac{T}{300\,\text{K}} \right)^{-n_i} ,\qquad (5.1)$$

using a reference value at STP $\sigma_{0,i}$ and an exponent for the temperature dependence n_i. No values for the collision of methane with hydrogen and water could be found

in the literature. To be able to carry out and evaluate the CTD measurements on the methanation reaction, two extensive measurement series have been conducted, each designed to extract the cross section of σ_{j,CH_4-H_2} and σ_{j,CH_4-H_2O}, respectively. The parameters $\sigma_{0,i}$, and n_i required for the methanation reaction are summed up in Table 5.1.

5.1 Mixtures of methane in hydrogen

The first experiment to extract a collision parameter was designed for mixtures of methane and hydrogen. As it was unclear how σ_{j,CH_4-H_2} would depend on temperature, pressure, and concentration, the experiment was designed to cover all three parameters in a broad range. The results shown here have been previously published in Harm Ridder, Christoph Sinn, Georg R Pesch, Wolfgang Dreher, and Jorg Thöming. "Longitudinal Relaxation (T1) of Methane/Hydrogen Mixtures for Operando Characterization of Gas-Phase Reactions". In: *ACS Measurement Science Au* 2.5 (2022), pp. 449–456. DOI: 10.1021/acsmeasresciau.2c00022.

5.1.1 Experiment

Measurements to extract σ_{j,CH_4-H_2} were carried out in a cylindrical glass tube, which was open for gas flow at the top and bottom of the cylinder (Figure 5.1). Two honeycomb structures were placed inside the glass tube to improve radial heat transport. The second honeycomb was used to offer a second temperature level for the measurement as the gap between the two monoliths interrupts thermal conduction. The tube was positioned in the center of the MRI reactor and heated up using the diode laser, as described in Chapter 3.1.2. Inside the tube at the front,

Table 5.1: Overview of cross sections for the collision of methane with gases present during the methanation reaction. The parameters are required to predict T_1 according to Equation 4.4.

Collision partner i	$\sigma_{0,i}/\text{Å}^2$	n_i	Source
CH_4	18.4	0.9	
N_2	16.3	0.87	Jameson et al. [76]
CO_2	24.1	0.98	
H_2	4.07	0.52	this work
H_2O	27.96	1.15	

a ceramic sponge was placed to absorb the radiative heat from the laser. The last honeycomb was wrapped in fiberglass wool and fitted tightly into the tube to fixate the three monoliths (black sponge and two ceramic honeycombs) inside the glass tube.

The measurements were performed using five different gas mixtures of hydrogen and methane (CH_4/H_2 ratios of 1:0, 1:3, 1:1, 3:1, and 0:1) with temperatures ranging from room temperature to approximately $300\,°C$ and pressures ranging from 1 to $5\,bara$. A constant gas flow of 0.565 LN/min was set for all measurements with changing gas composition. The pressure was measured after mixing the gases outside the MR scanner's room and altered using a back-pressure regulator at the outlet of the chemical reactor (see Chapter 3.1.3). From the gas composition and pressure, the molecular number density could be calculated a priori. Thus, it was sufficient to use the A/A_0 ratio to compute the temperature from Equation 4.13. For this, a base measurement of pure methane at room temperature was carried out, like in every other CTD measurement. After the initial measurement, the system was heated for about $90\,min$ to reach a certain temperature level. The power level of the laser was kept constant each day. This way, the actual temperature inside the measurement tube changed only slightly as a function of gas composition and pressure. Temperature changes occurred due to the different heat capacities of methane [80] and hydrogen [81] and because methane partially absorbs the laser's radiation, while hydrogen does not. However, as the temperature was measured *operando*, these changes could be detected and were thus accounted for. The measurements were performed in an
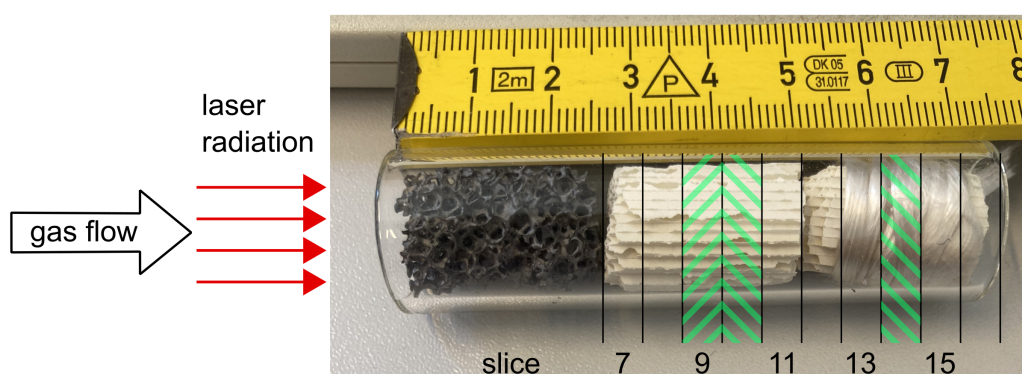

Figure 5.1: Picture and schematic drawing of the glass cell used to measure $\sigma_{CH_4-H_2}$. The cell is heated frontally using the $500\,W$ diode laser described in Chapter 3.1.2. Figure reworked from [3] under Creative Common License (CC BY 4.0).

open reactor system as this facilitated the change of gas composition and increased heat transport inside the tube.

5.1.2 Results

The obtained longitudinal relaxation times T_1 as a function of temperature for different pressures and gas ratios are shown in Figure 5.2. Each panel a)-c) contains the results
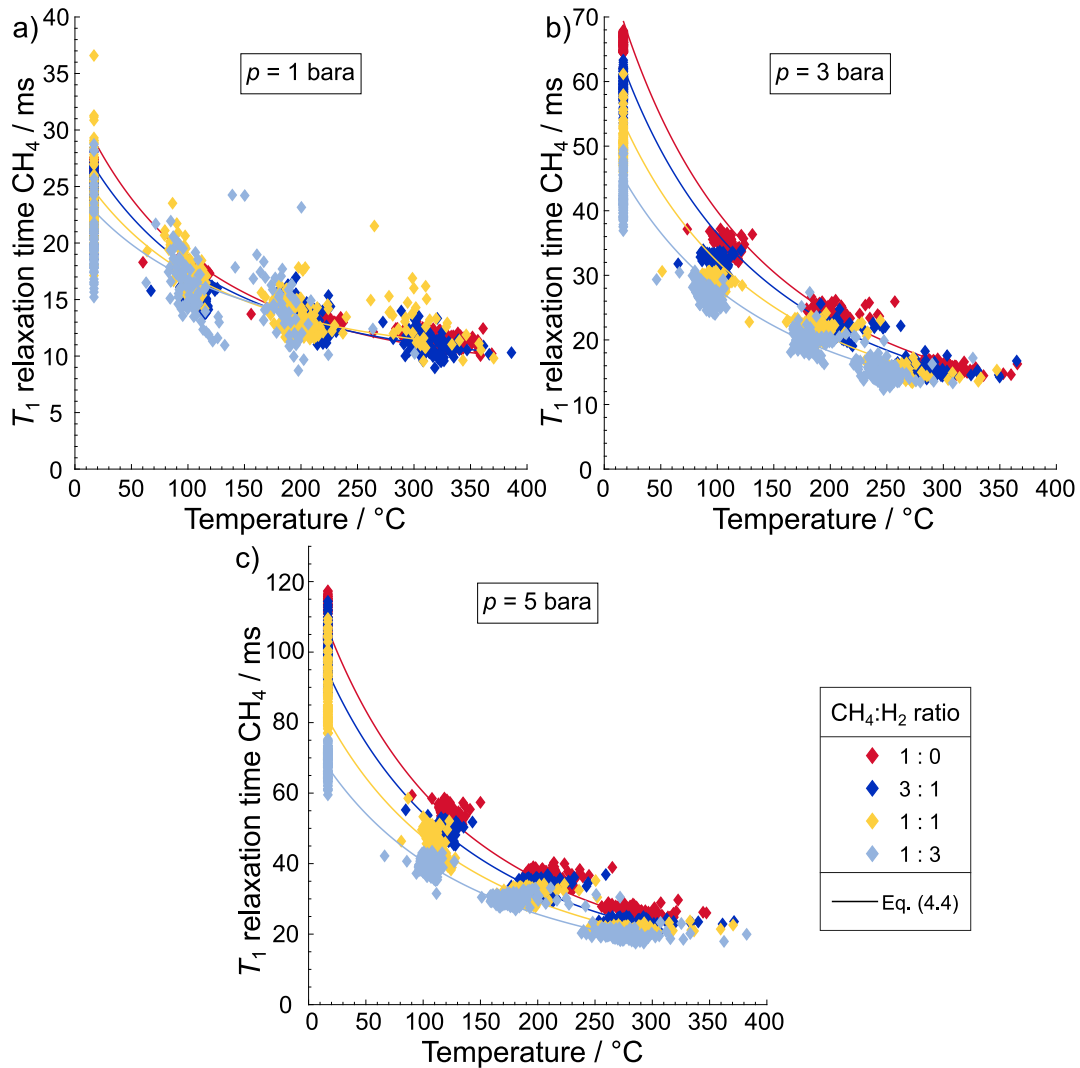

Figure 5.2: Measured longitudinal relaxation time T_1 of methane in different mixtures with hydrogen at the three investigated pressure levels of a) $p = 1$ bara, b) $p = 3$ bara and c) $p = 5$ bara. The cross section for the collision of methane with hydrogen is fitted to all data points at $p = 5$ bara. For reference, the calculated T_1 dependence is shown as well. Reworked from [3] under Creative Common License (CC BY 4.0).

of one pressure level. As the measurements at the highest pressure ($p = 5$ bara) yielded the most accurate results, the required collision cross section σ_{j,CH_4-H_2} was fitted to this data set. Curves (solid line) using the theoretical prediction of T_1 from Equation 4.4 with the acquired σ_{j,CH_4-H_2} are plotted for reference.

At $p = 1$ bara (Figure 5.2a), the theory predicts little dependence of T_1 on gas composition (lines). The measurements at the same temperature level deviate strongly in measured temperature and their T_1. The predicted temperature dependence is only slightly visible, while no change in T_1 from gas concentration can be seen. The uncertainty found here matches the uncertainty described in Chapter 4.3. The molecular number density was even lower towards higher temperatures than in the previous experiments as an open gas stream was used here, where the gas density decreases with temperature. Again, the low molecular number density does seem to enhance statistical uncertainty (standard deviation) compared to the higher pressure levels.

The next higher pressure level of $p = 3$ bara shows a clear dependence of T_1 on the gas ratio both in theory and from the experimental data (Figure 5.2b). T_1 increases with methane-to-hydrogen ratio and decreases with temperature. Compared to 1 bara, the temperature dependence at 1 bara is more pronounced, and experiments show less statistical uncertainty. For pure methane, the theoretical T_1-values are higher than the experimental values, emphasizing the findings in Figure 4.2. During the publication of these results, we could not find a suitable explanation for the low experimental T_1-values. However, this behavior might again result from low magnetic field homogeneity. Only three out of eight slices of the measurements could be used (Figure 5.1) due to the strong influence of the inhomogeneous magnetic field. While the problems in the remaining slices mainly arise from the interruption of the honeycomb, which results in sharp edges, no proper shimming was deployed during the measurements as well. Similar to the experiments in Chapter 4.3, a water sphere was used for shimming and the decay of the methane signal does not match well with the assumed exponential decay, even in the used slices #9, #10, and #14.

At $p = 5$ bara (Figure 5.2c), the dependence of T_1 on temperature and concentration is even more pronounced, and the uncertainty is reduced further. Here, Equation 4.4 can reproduce the data points accurately over all measured temperatures. Therefore, the parameter σ_{j,CH_4-H_2} was extracted from this data set. The parameter is obtained by minimizing the difference between the data points of methane/hydrogen mixtures at $p = 5$ bara and the theoretical prediction of Equation 4.4 using a linear least squares algorithm. The parameters for the effective cross section for the collision of methane

with hydrogen were determined as $\sigma_{0,H_2} = (4.07 \pm 0.09)$ Å^2 and $n_{H_2} = (0.52 \pm 0.01)$ (uncertainty given as a 95% confidence interval). Please note, the uncertainty only represents the influence of statistical errors.

Apart from the obtained parameter σ_{j,CH_4-H_2}, the presented results emphasize the importance of magnetic field homogeneity for the measurement of T_1 and A. While the inhomogeneity can partly be met using proper shimming parameters and objects, especially the very local inhomogeneities cannot be countered using external shimming coils. The fact that sharp edges heavily influence field homogeneity is a known principle in the field of dielectrophoresis. For instance, in the work of Lorenz et al. [82], a ceramic sponge is used to deliberately impose electric field gradients in a suspension as these are the main source of dielectrophoretic forces. The theory behind the electric and magnetic fields is very similar. In other works, magnetophoretic forces are used to alter the movement of particles in a suspension [83]. From the works in the field of dielectrophoresis, it is known that the electric field gradients can very well be studied [82, 84] using, for instance, the finite-element computer simulation toolbox COMSOL (Comsol Multiphysics GmbH, Göttingen, Germany). From simulations on differently shaped objects, information could be gathered on how edges influence field homogeneity and, even more importantly, how shapes can be changed to avoid inhomogeneities. Such studies would be a vital asset for the design of the experimental setups of future MRI studies.

5.2 Mixtures of methane in water

The second missing parameter to calculate the longitudinal relaxation time T_1 of methane is the cross section for the collision of methane with water $\sigma_{CH_4-H_2O}$. Due to the low vapor pressure of water at room temperature, it was impossible to repeat the measurements of Chapter 5.1 by just replacing hydrogen with water. To estimate $\sigma_{CH_4-H_2O}$, the concentration of both components needs to be varied. Only gaseous water interacts with the gaseous methane, but the amount of water in the gas phase is almost non-existent at room temperature. Hence, the temperature needs to be increased to increase the amount of vapor. However, as long as the temperature is below the boiling point of water, the ratio between water and methane is still temperature dependent. Additionally, the amount of liquid water required to form reasonable (e.g., 25%/75% or 50%/50%) mixtures of methane and vapor is comparably low. All these factors make the control of methane/water mixtures very difficult in an open reactor setup as was used to measure $\sigma_{CH_4-H_2}$. Instead,

a procedure was developed to fill and seal glass tubes with a certain amount of water and methane (see Appendix A) using liquid nitrogen. In total, 19 tubes filled with different amounts of water and methane were created aiming at methane/water mixtures of 0%/100%, 25%/75%, 50%/50%, and 75%/25% and different pressures. The longitudinal relaxation time T_1 of methane in these tubes was then measured at two different temperature levels inside the MRI reactor to extract $\sigma_{CH_4-H_2O}$. However, the performed measurements were biased from unstable temperature conditions. Only three measurements out of the initial ten were free of this bias and have thus been used to fit the actual $\sigma_{CH_4-H_2O}$. The remaining results will be repeated after finishing this thesis to be published openly.

5.2.1 Experiment

The glass containers used to study different mixtures of methane and water were made from tubes with ID 4 mm and OD 6 mm and were sealed using a blow torch. The water was purified using the Omniatap 6 UV/UF (stakpure GmbH, Niederahr, Germany) to an electrical resistivity of about $18\,M\Omega\,cm$; methane was provided by Linde GmbH (Pullach, Germany, purity 3.7). In the experiments of Chapter 4, the glass tubes could only be filled up to a pressure slightly below ambient conditions. Using a new preparation procedure (Appendix A), a quasi-unlimited amount of methane could be sealed inside the glass containers as the procedure involved liquid nitrogen to freeze the methane at the bottom of the tube prior to sealing. While vast amounts of substance might be filled into the glass containers using this technique, it is imperative that the maximum permissible surface tension of the material is taken into account for safety reasons.

For each measurement, five glass containers were placed inside the MRI reactor (Figure 5.3). One was always the same glass container filled with pure methane, which
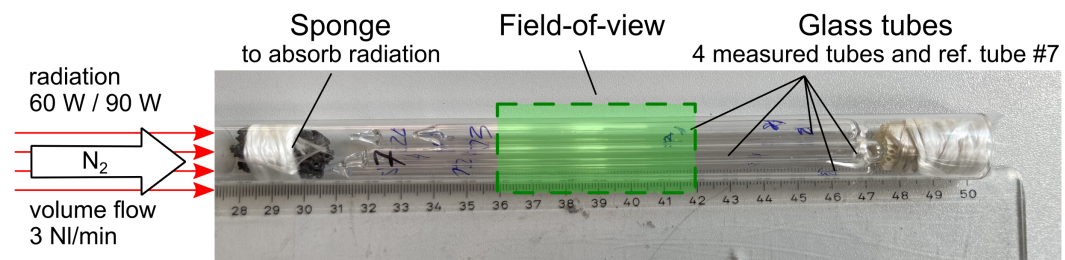

Figure 5.3: Picture of the array of glass tubes used to measure $\sigma_{CH_4-H_2O}$. The cell is heated frontally using the 500 W diode laser described in Chapter 3.1.2.

was a reference for temperature and pressure. The remaining glass containers were each filled with varying amounts of methane and water. The glass containers were frontally heated using the defocused diode laser, similar to the experiments shown in Chapter 5.1. In order to increase axial heat transport along the glass containers, a constant gas flow of 3 NL/min nitrogen was applied during all measurements. Each assembly of 4+1 glass containers was subjected to two different laser heating levels of 60 W and 90 W, respectively, resulting in a temperature range of 110-160 °C at 60 W and 320-350 °C at 90 W. The pressure ranged from 1.6 bara to 18.8 bara and the methane mole fraction from 0 to 0.82.

This thesis only shows the results of eight of the initially 19 glass containers. The temperature acquired in the remaining measurements carries a bias because of non-steady-state conditions during the measurements (see Figure 5.6). The temperature inside the glass tube should monotonically decline from front to back, as both the heat transported by the gas flow and the original laser heating are coming from here. In the unsteady measurements, the resulting temperature profile had an S-type shape which could not be reproduced. By coincidence, the time to reach steady-state was increased in one measurement. The longer wait time led to a significant improvement in the recorded temperature profile. Initially, steady-state conditions were assumed when a temperature sensor at the RF coil showed no changes over time, which was reached after approximately 1.5 h of heating. Instead, a 3-4 h wait time is needed to reach a constant temperature over the 70 min measurement time.

Using the reference tube and the fitted signal amplitudes in each voxel, the temperature T, mole fraction x and pressure p inside each tube could be quantified. The temperature of the reference tube was calculated using the CTD method similar to the results of the proof of concept (Chapter 4.3). The mole fractions of methane x and water $x - 1$ were quantified from the ratio of signal amplitude of the two signals and averaged over each tube. A factor of 2 was used to account for the different number of protons in the two molecules

$$x_{CH_4} = \frac{A_{CH_4}}{A_{CH_4} + 2A_{H_2O}} \quad \text{or} \quad 1 - x_{CH_4} = \frac{2A_{H_2O}}{A_{CH_4} + 2A_{H_2O}}. \tag{5.2}$$

Next, the pressure inside each measured tube was calculated by comparing its signal amplitude to the reference tube's signal. This factor was applied to the already-known pressure inside the reference tube to calculate the pressure inside the measured tube. The pressure inside the reference tube was known from the increase in temperature, as well as the pressure at room temperature of about 10 bara,

which was determined from prior T_1 measurements. To improve the quality of the calculated results, either the methane or water signal amplitude was used, whichever was larger. Furthermore, only the most central voxel of the tube in each slice was used. Like the mole fraction, the pressure was also averaged over each tube.

$$p = \frac{A_{CH_4}}{A_0 x_{CH_4}} p_0 \quad \text{or} \quad p = \frac{A_{H_2O}}{A_0 x_{H_2O}} p_0. \tag{5.3}$$

In order to calculate reliable results from amplitude ratios, it was necessary to ensure that the signal could be compared exactly to the signal of the base measurement at room temperature. The glass tube's cross section is small compared to the voxel size and tiny movements in the approximately 5 hours between acquiring the base and the actual measurement led to unwanted changes in the amplitude distribution. To account for this, the signal in the 3×3 voxels of each tube was distributed symmetrically around a single voxel. To this end, the MPM fitting procedure was applied to one slice at a time, and the 4D data set was then shifted in x- and y-dimensions to centralize the signal in that particular slice (Figure 5.4). The procedure was repeated for each of the 11 evaluated slices, and the results were combined into one data set of a single tube. The $3 \times 3 \times 11$ central voxels were evaluated from each tube. However, the fit failed in some voxels. Usually because of an influence of the neighboring reference tube, which exhibited a strong signal compared to the tubes with lower pressure. Those voxels with failed fits have been ignored.
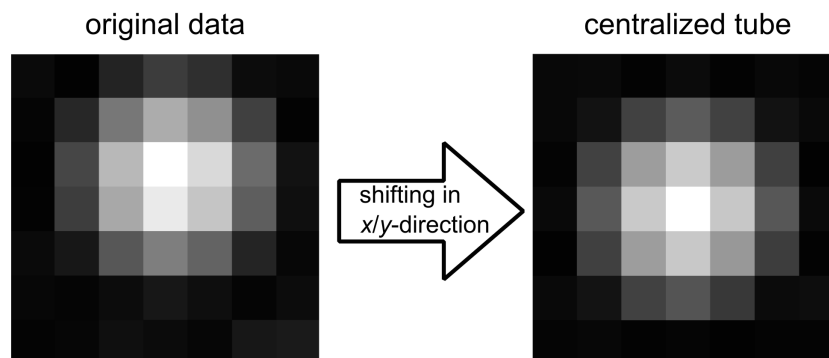
original data   centralized tube

shifting in
x/y-direction

Figure 5.4: Signal acquired from each tube was slice-wise centralized around a single voxel. This way, reliable results from amplitude ratios could be calculated.

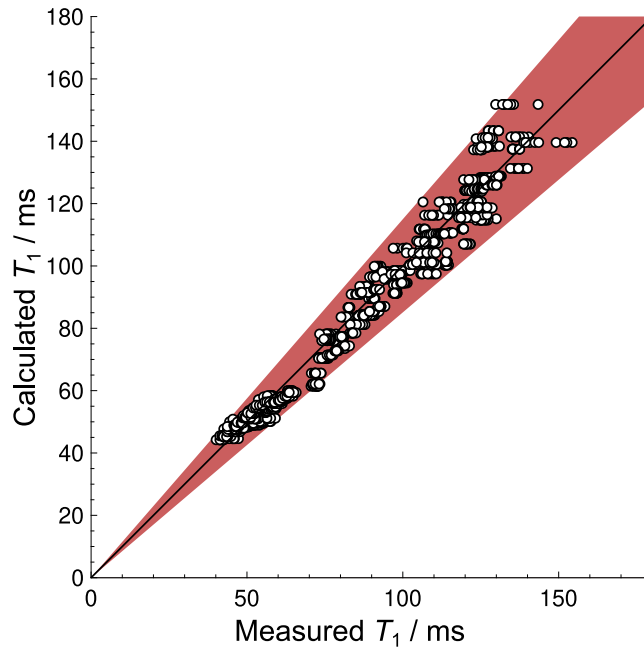**Figure 5.5:** Comparison of measured T_1 relaxation times of methane in a mixture with water and the respective values calculated from the theory of Dong and Bloom (Equation 4.4). The red area indicates a ±15 % deviation.
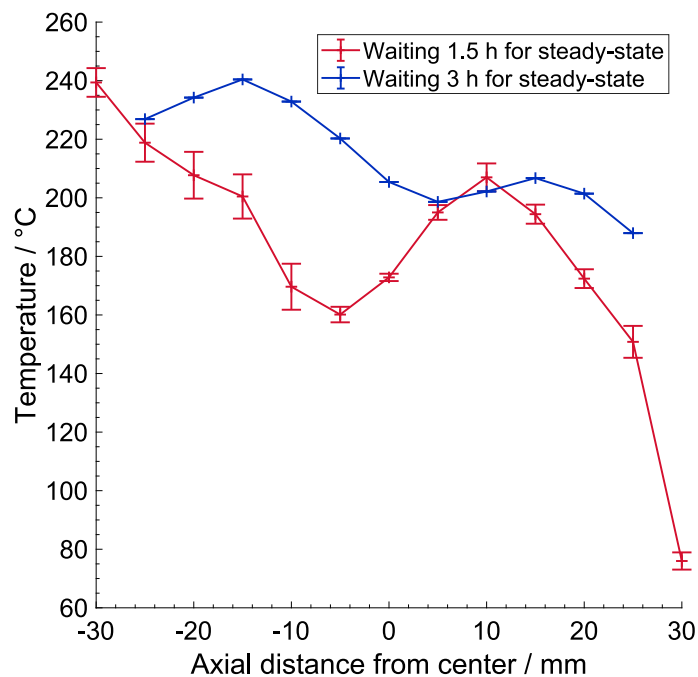

Figure 5.6: Influence of the wait time on the measured temperature distribution inside the reference tube. Significant temperature gradients were found to occur in a non-steady-state after 1.5 h.

5.2.2 Results

From the T_1 relaxation of methane, the parameters for the effective cross section for the collision of methane with water were extracted as $\sigma_{0,H_2O} = (27.96 \pm 6.38)\,\text{Å}^2$ and $n_{H_2O} = (1.150 \pm 0.282)$. Using the cross section, as well as the calculated values for the pressure, temperature and molar concentration, the T_1 relaxation of methane can be calculated from theory in the presence of water. A comparison between calculated and measured T_1 times is given in Figure 5.5. Most data points lie within an accuracy of $\pm 15\,\%$, as depicted by the red area.

As only a reduced amount of data points could be considered for $\sigma_{CH_4-H_2O}$, a higher uncertainty can be expected. Moreover, the question arises if other measurements are also influenced by changing temperatures during the measurement. In the proof of concept (Figure 4.1), the temperatures show slight local maxima, which might arise from a change in the local temperature. However, in this case, the assumption of steady-state was based on the temperature sensors, which were inside the MRI reactor's tube and not on the outside. Thus, only the reported $3\,\text{K}$ temperature difference would apply here. The measurements to obtain the $\sigma_{CH_4-H_2}$, unfortunately, do not allow an analysis of the temperature along the reactor as only three slices could be evaluated. Because the measurements are already overshadowed by the magnetic field inhomogeneities, a repetition of the measurements might be advisable to ensure that both factors can be ruled out. The methanation reaction measurements that are presented in the following chapter are likely not biased by unsteady temperature distributions. Here, the waiting time was not based on the temperature sensor inside the RF coil but rather on a constant carbon dioxide conversion rate measured at the outlet.

Apart from the proposed investigation of magnetic field inhomogeneities from the previous measurements, future works could try to study the temperature influence on the raw data acquired in the k-space by comparing artificial k-space with and without non-steady temperatures. From such simulations it can be derived how crucial temperature changes in the course of measurement are and if it is possible to correct temperature-biased data.

Characterization of the methanation reaction

In the last chapters, the foundation was laid to characterize methane in the environment of the methanation reaction using MRI. In this chapter, the previous results are brought together to perform the methanation reaction inside the MR magnet attempting to display the distribution of temperature and concentration individually, *operando* and 3D spatially resolved.

6.1 Experiment

The methanation reaction was performed on a cordierite honeycomb coated with a 12 wt% Ru/γ-Al$_2$O$_3$ wash coat. Again, the diode laser was used to heat an irregular ceramic sponge directly in front of the honeycomb. The gas concentration at the inlet was chosen such that at most 50 % of the incoming gases can perform the methanation. Instead of diluting the gas with an inert gas like nitrogen or argon, the gas was diluted using hydrogen and methane. By doing this, everywhere in the reactor tube, a signal from both gases can be measured regardless of the current progress of the reaction. In order to achieve different conversions inside the reactor, the inlet conditions have been changed (Table 6.1). The heating rate of the laser was changed from initially $P_{laser} = 75\,W$ (state #1) to 60 W (state #2) and later to 70 W (state #3) for the last measurement, while the volume flow was changed from $\dot{V} = 2\,NL/min$ (state #1 & #2) to 3 NL/min (state #3) for the last

Table 6.1: Inlet conditions for each observed steady state of the methanation reaction.

State	Mole fraction H$_2$/CO$_2$/CH$_4$	$\dot{V}$ / (NL/min)	p / bara	P_{laser} / W
reference	0/0/1	0.5	4.2	0
#1	0.58/0.12/0.3	2	7.2	75
#2	0.58/0.12/0.3	2	7.2	60
#3	0.58/0.12/0.3	3	7.2	70

measurement. The measurement of the first steady-state was repeated as an estimate for the reproducibility of the technique (State #1.1 & #1.2).

The CTD measurements were again performed using the saturation recovery technique. The calculation procedure was based on an open reactor system like in Chapter 5.1. The initial conditions for the mole fraction at the inlet required for Equation 4.4 and Equation 4.13 are the same for all three states, as stated in Table 6.1. It was assumed that the changes in mole fraction for each gas follow exactly the stoichiometry of the chemical reaction.

A measurement series consisted of individual measurements using τ-values of 300 ms, 150 ms, 80 ms, 40 ms, 20 ms, 10 ms, 6 ms, 3 ms and 0.8 ms. In the last measurement series with $\dot{V} = 3\,\mathrm{NL/min}$ and $P_{\mathrm{laser}} = 70\,\mathrm{W}$, the measurement using $\tau = 300\,\mathrm{ms}$ was omitted because of the expected high temperature and the subsequent low T_1 relaxation time. The size of the field of view was 57 mm × 57 mm × 123 mm with 19 × 19 × 41 voxel resulting in a nominal voxel size of $(3\,\mathrm{mm})^3$. The acquisition time for the complete series was 92 min and 56 min without $\tau = 300\,\mathrm{ms}$. The reaction had to be kept in a steady state during the measurement process of a series. The current state of the reaction was monitored using an NDIR measurement device (see Chapter 3.1.3) that kept track of the integral methane, carbon dioxide, and carbon monoxide concentrations at the outlet. The reaction progress was determined by the amount of remaining carbon dioxide. Using methane as reference was not possible, as the accuracy of the IR measurements is significantly reduced at mole fractions above 30 %. The mole fraction of methane remained consistently above this threshold. Reaching steady-state conditions took about two hours, as indicated by the changes in gas composition by the NDIR device. In the meantime, 3D-MRSI measurements (Chapter 3.2.3) were performed with a temporal resolution of approximately 9 min.

The pressure during the reaction was kept slightly above 7 bara to ensure a high SNR for the measurement. The reference measurement required for the CTD method was performed at room temperature, using pure methane and at a pressure of about 4 bara. This setting was a compromise between SNR and measurement time, as at room temperature the change in pressure significantly increases the T_1 relaxation time requiring longer wait times τ in the measurement.

6.2 Results

Three different steady-state conditions of the methanation reaction were observed. The initial state (#1.1 & #1.2) exhibited quasi-full conversion. In state #2, almost no reaction occurred, while in state #3, a high volume flow with a large amount of formed methane was observed. The results of these measurements are four distributions of the methane's mole fraction and temperature inside the MRI reactor during the methanation reaction. Figures 6.3-6.6 show the resulting distributions for each state. The depictions show an image of the central longitudinal slice (sagittal, $x = \text{const}$) through the reactor for the temperature and the methane mole fraction. Further, four cross-sectional slices are shown for both parameters. The slice's positions are right before the monolithic sponge in the free gas phase, right after the monolithic sponge inside the honeycomb, and in two more positions inside the honeycomb. The reactor needed to be completely disassembled between state #1 and state #2. As a result, the exact position of the sponge and honeycomb in the field of view varies slightly, just like the rotational angle of both objects inside the tube. In gray color, voxels are shown where the fitting procedure failed, or the measurements did not meet the requirement for good fits. Voxels were ruled out when they were outside the region of interest (outside the reactor tube), when their solution was out of physical bounds, and when the magnetic field inhomogeneity was too low (r^2 of the fit to pure methane at the base measurement below 0.95). It has to be noted that solutions for the mole fraction from 0.12 to 0.81 were allowed even though this leads to negative concentrations of water, carbon dioxide, or hydrogen. This was primarily due to numerical reasons. However, in some parts the mole fraction does seem to reach values above full conversion. The negative concentrations were necessary to calculate a solution in those voxels. This necessity mainly shows that the assumed boundary condition of an ideal extent of reaction does not suffice to describe the investigated system.

In **state #1**, the highest amount of laser heating was used, and almost complete conversion of carbon dioxide to methane was reached (yield 91.2 % and 90.4 %). A high local concentration of methane can be seen in the two distributions of state #1 (Figure 6.3 & 6.4). The highest temperature (approximately 800 °C) and the highest mole fraction (0.64) are reached at the beginning of the honeycomb. The hot spot is not in the radial center of the honeycomb, but it is slightly shifted upward against gravity. It can be seen that while the concentration distribution moves completely along the flow direction and no increased amount of methane can be found in front

of the sponge, the contrary is the case for the temperature distribution. While the high temperature in the region of the ceramic sponge is partly due to the heating of the laser, some heat formed in the reaction is also conducted through the solid material against the flow direction. In the cross sections towards the end of the honeycomb, the profiles are not ideally symmetrical along the horizontal axis, which is possibly a result of the imperfect structure of the honeycomb. Some channels break during manufacturing, storage, and placement inside the reactor. Thus, the honeycomb is asymmetric by itself and does not ideally fit into the reactor tube, promoting local bypasses.

The comparison of the results for the two measurements of state #1.1 & #1.2 shows a high similarity, indicating that SNR effects on the measurement are negligible and that the reaction reached a steady state. With the chosen inlet conditions (Table 6.1), the highest possible methane mole fraction is 0.54, as can be derived from the reaction balance of the methanation. While reaching local methane concentrations of up to 0.64 seems unrealistic, local diffusion effects might lead to such behavior. As hydrogen and carbon dioxide are consumed, the tendency of the two gases to
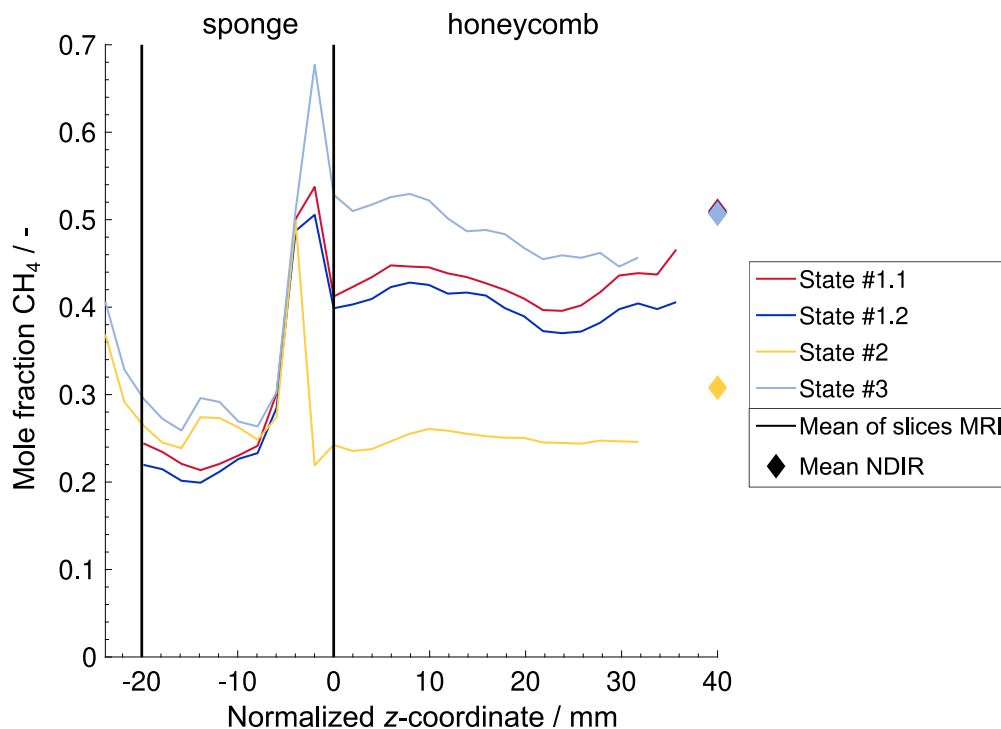

Figure 6.1: Comparison of the different mole fractions of methane measured via MRI and NDIR. The mean per axial slice is shown for the MRI data, while for the NDIR data, the temporal mean is shown. The z-coordinate was normalized to the beginning of the catalytically active honeycomb.

diffuse into the region of high methane production rises. This tendency is increased as the methanation reduces the molecule number and, thus, the volume of the gas by 40 % leading to additional convection into the region. As described in Chapter 4.2.3, the CTD calculations require assumptions about the distribution of the other gases around the methane. Lacking more sophisticated information, the gas mixture's composition is assumed to solely depend on the extent of reaction. Thus, a certain methane content can only be accompanied by an exact combination of the other three gases hydrogen, carbon dioxide, and water. When diffusion effects change the real distributions, this assumption is violated leading to false results in the calculated distribution shown here. When looking at the mean mole fraction of methane in each slice for the different measurements (Figure 6.1), it can be seen that the maximum mole fraction of methane of 0.54 is not exceeded in any single slice inside the honeycomb. Thus, high mole fractions of methane are only observed locally.

The resulting distributions of **state #2** of the methanation reaction are shown in Figure 6.5. Compared to state #1, the heating rate of the laser has been reduced from 75 W to 60 W. The highest temperature of about 400 °C is found at the ceramic sponge. At the beginning of the honeycomb, the temperature has dropped to approximately 200 °C. According to literature [85], significant conversion rates require temperatures of at least 250 °C on a Ru/Al_2O_3 catalyst with high catalyst loading like in this case. Thus, the temperature inside the honeycomb is too low to light off the reaction. No increase in methane can be observed in the concentration distribution. The 5 % yield measured by the NDIR spectrometer only results in an increase of the methane mole fraction of 0.012, which cannot be resolved by the MRI measurement. The results of this measurement underline how the CTD method can calculate temperature and concentration independently of each other. The temperature has a clear gradient and decreases towards the end of the reactor, while the methane concentration stays constant. It is noteworthy that the fitting procedure did not calculate many voxels in the region of the sponge. The ceramic sponge creates large magnetic field inhomogeneities, which affect the signal due to the different positioning more in these two measurements than in the measurements of states #1.1 and #1.2. However, as the sponge is not the main region of interest, the results still give essential information about the measured system.

State #1 showed almost complete conversion, and state #2 showed almost no conversion due to the difference in heating of 75 W and 60 W, respectively. For **state #3**, it was planned to capture images of an in-between state with non-full conversion. However, as will be shown in the next chapter, it was impossible to reach steady-state

conditions using 65 W or 70 W as the formation of liquid water led to an oscillating reaction behavior. In order to avoid liquid water at least inside the catalytically active region, the volume flow was increased from 2 NL/min to 3 NL/min, aiming to push the formation of liquid water toward the reactor outlet. This high-velocity measurement was the last of the three steady states observed in the measurement series. Its results are shown in Figure 6.6. In state #3, near full-conversion was reached like in state #1, but as a lot more gas was available for reaction, the reaction zone is larger and covers almost the whole beginning of the honeycomb. Thus, the effect of natural convection on the temperature and methane distribution is less pronounced than in state #1.

The results of state #1 and #3 can be analyzed further when the calculated thermo-dynamic equilibrium of the methanation reaction (Figure 2.1) is considered. Even though the assumptions for the calculation of the equilibrium conversion (infinitely long tube and isothermal conditions) do not hold for the studied reactor, it can still be derived that the reaction does not take place at temperatures above 800 °C. As a result, the highest possible temperature inside the reactor is approximately 800 °C. In fact, this is just the maximum temperature exhibited by the measurements of states #1 & #3. This comparison not only shows that the measured temperature agrees well with state-of-the-art knowledge. Moreover, it is visible that the main limiting factor for the methanation reaction in states #1 & #3 is the thermodynamic equilibrium. In this case, the limitation is actually beneficial for the reactor's safety. Without
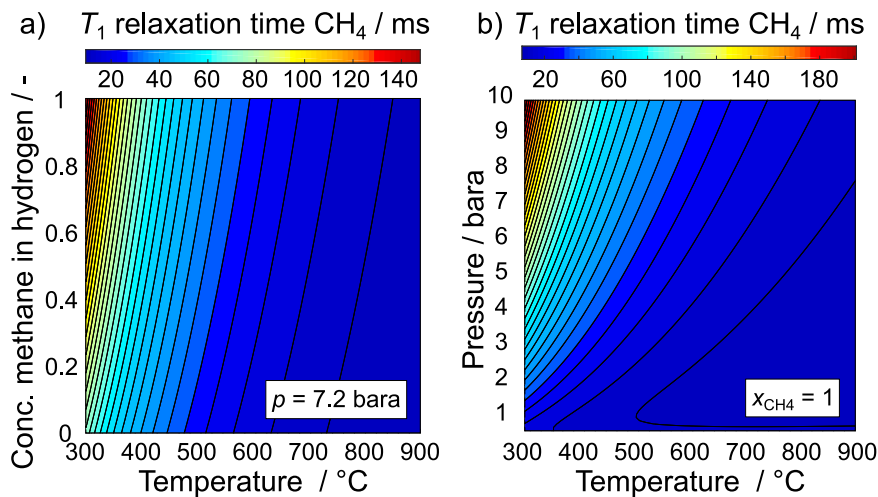

Figure 6.2: Dependence of T_1 on temperature, pressure, and concentration (in hydrogen) according to Equation 4.4. The data range for T_1 in the contour plots is split into 35 equidistant steps that are represented using one unique color. Narrow color fields thus represent a larger T_1 gradient.

it, the local temperature could rise a lot higher until the honeycomb starts to melt. This point emphasizes the need to avoid hot spots for exothermic reactions using proper heat management when the thermodynamic equilibrium is not a limiting factor. However, for the methanation the formation of hot spots is less important when the catalyst is able to endure the temperature of $800\,°C$.

In the discussed results, the calculated distribution of the temperature fits better to the expected outcome than the mole fraction. While the temperature is in reasonable agreement with literature at both ends of the measured spectrum, mole fractions outside the expected range from 0.3 to 0.54 are frequently encountered. As already stated, high mole fractions might be a result of diffusion effects. However, values below 0.3 are impossible given the used inlet conditions. One explanation for the calculation error might be found in the dependence of T_1 on the three reaction parameters temperature, gas concentration, and pressure (Figure 6.2). The steepest gradients can be found for the temperature dependence, while the influence of the gas concentration is less pronounced. A low gradient means that the solver reacts to any measurement errors with large changes of gas concentration, and vice versa for large gradients. This might explain the higher accuracy of the temperature profile compared to the map of the mole fraction calculated for the methanation.

inlet mole fractions: H_2 0.58 / CO_2 0.12 / CH_4 0.30 $\dot{V}$: 2 Nl/min p: 7.12 bar(a) laser: 75 W

outlet mole fractions: H_2 0.20 / CO_2 0.01 / CH_4 0.52 / H_2O 0.27 yield: 91.2 %

Figure 6.3: Results for the measurement of state #1.1. The measured temperature and mole fraction of methane are shown as individual images. For both, the central longitudinal slice (sagittal, x = const) through the reactor is shown. Further, four cross sectional slices are shown right before the monolithic sponge in the free gas phase, right after the monolithic sponge inside the honeycomb and in two more positions inside the honeycomb. For orientation the positions are indicated in comparison to 3D models of the measured objects. In gray voxels no data was fitted.
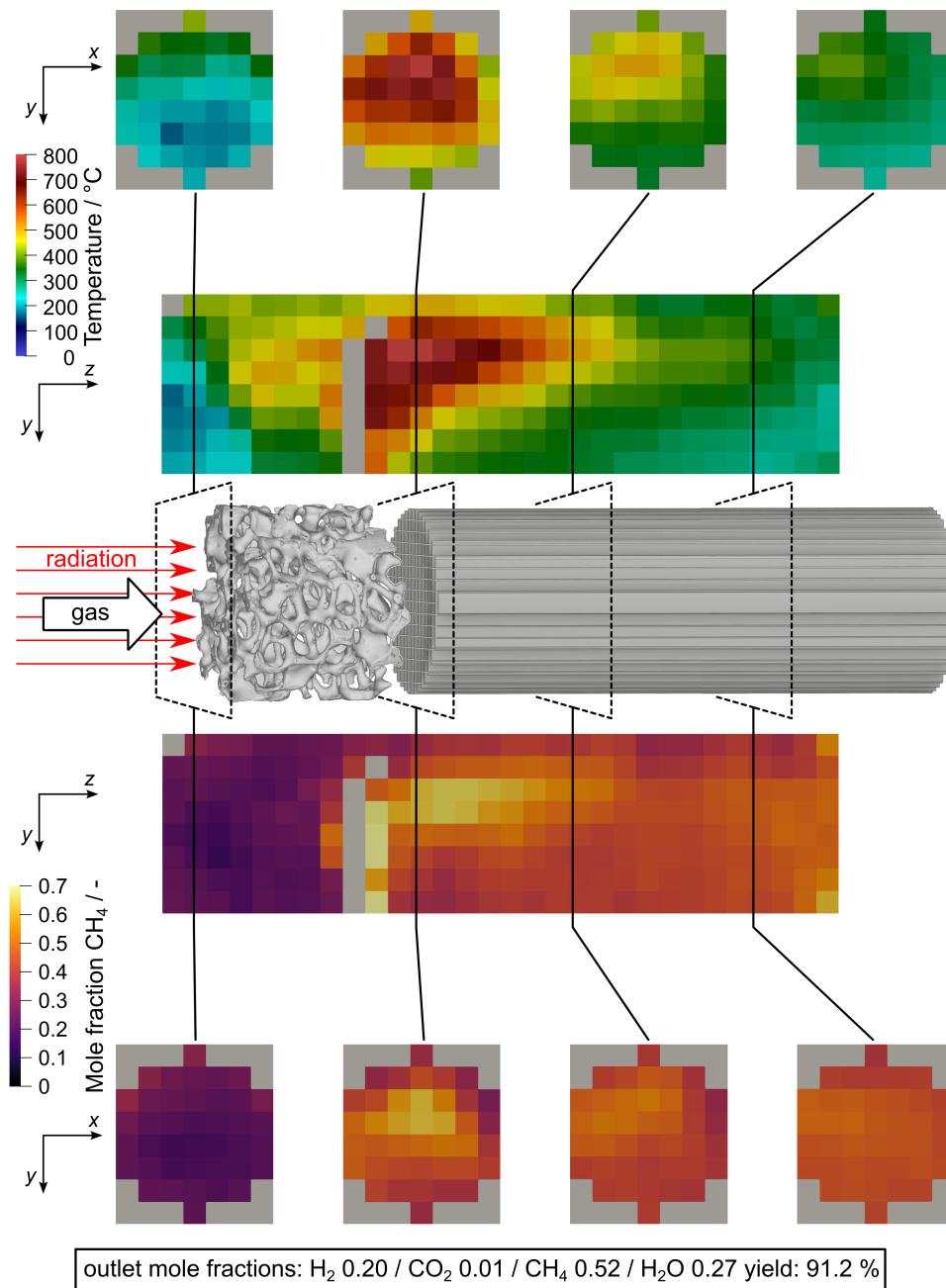
Figure 6.4: Results for the measurement of state #1.2. The measured temperature and mole fraction of methane are shown as individual images. For both, the central longitudinal slice (sagittal, x = const) through the reactor is shown. Further, four cross sectional slices are shown right before the monolithic sponge in the free gas phase, right after the monolithic sponge inside the honeycomb and in two more positions inside the honeycomb. For orientation the positions are indicated in comparison to 3D models of the measured objects. In gray voxels no data was fitted.

inlet mole fractions: H$_2$ 0.58 / CO$_2$ 0.12 / CH$_4$ 0.30 V̇: 2 Nl/min p: 7.12 bar(a) laser: 60 W

outlet mole fractions: H$_2$ 0.57 / CO$_2$ 0.11 / CH$_4$ 0.31 / H$_2$O 0.01 yield: 5 %

Figure 6.5: Results for the measurement of state #2. The measured temperature and mole fraction of methane are shown as individual images. For both, the central longitudinal slice (sagittal, x = const) through the reactor is shown. Further, four cross sectional slices are shown right before the monolithic sponge in the free gas phase, right after the monolithic sponge inside the honeycomb and in two more positions inside the honeycomb. For orientation the positions are indicated in comparison to 3D models of the measured objects. In gray voxels no data was fitted.

inlet mole fractions: H_2 0.58 / CO_2 0.12 / CH_4 0.30 $\dot{V}$: 3 Nl/min p: 7.12 bar(a) laser: 70 W

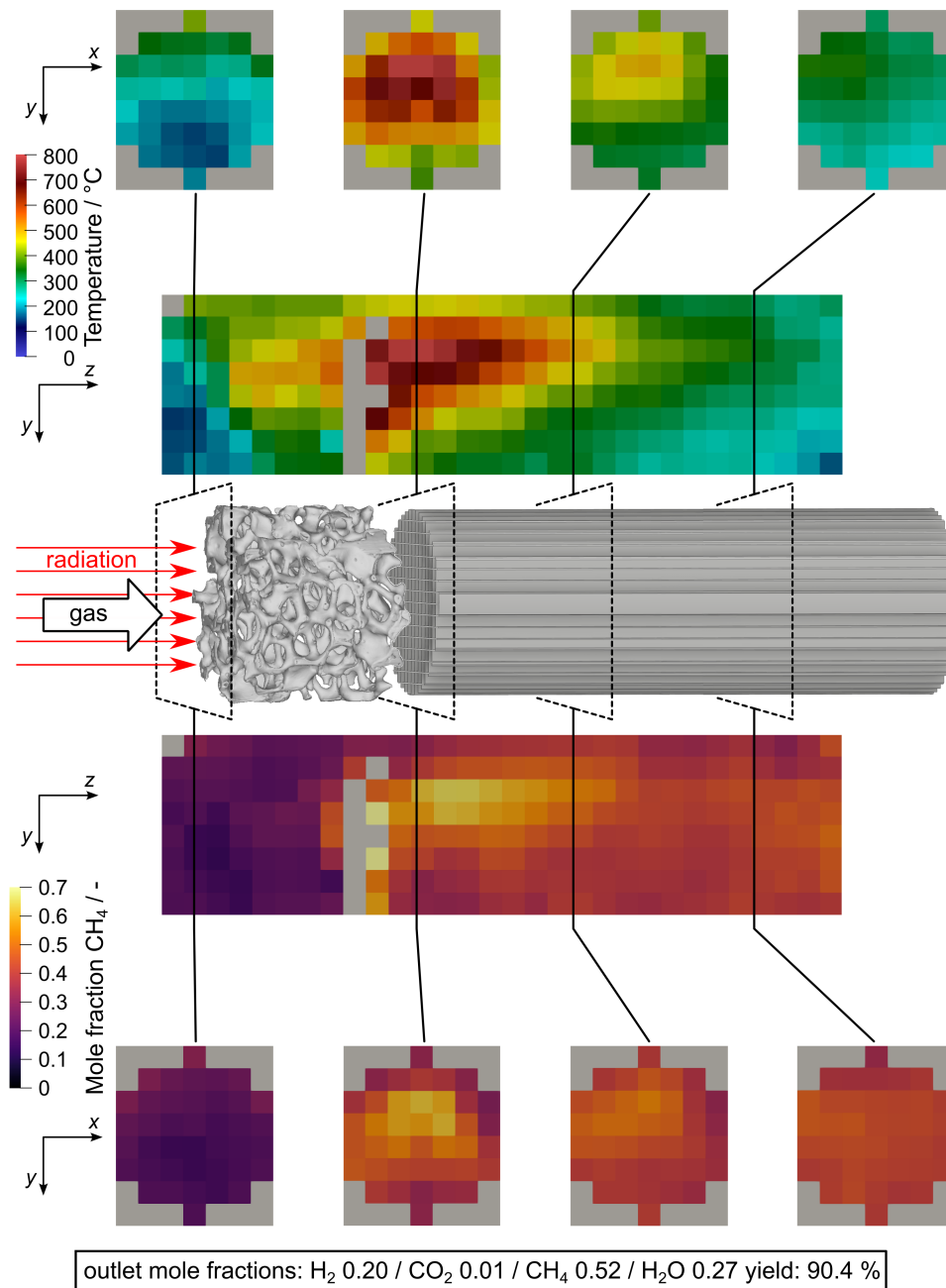outlet mole fractions: H_2 0.20 / CO_2 0.01 / CH_4 0.52 / H_2O 0.27 yield: 90.2 %
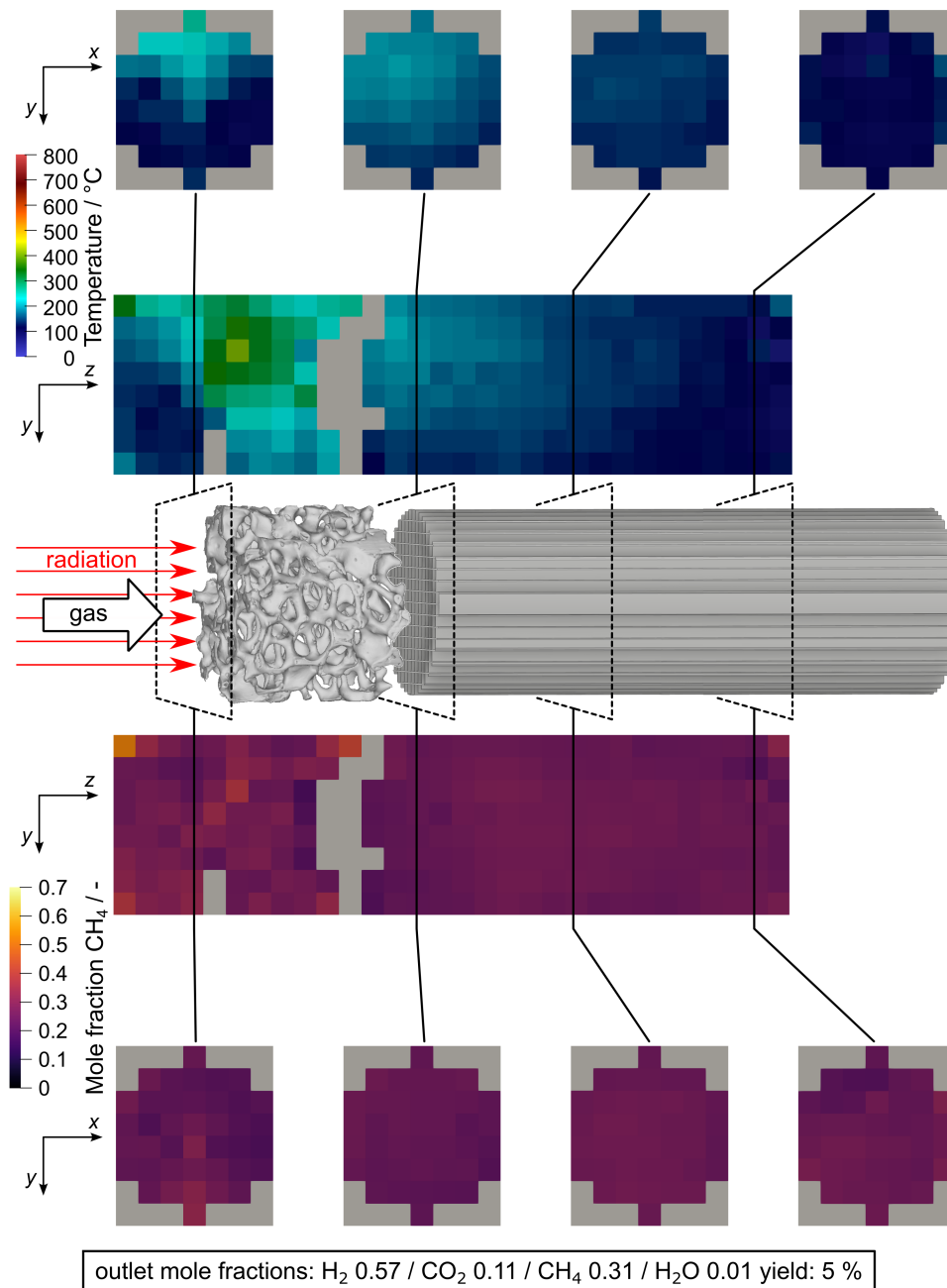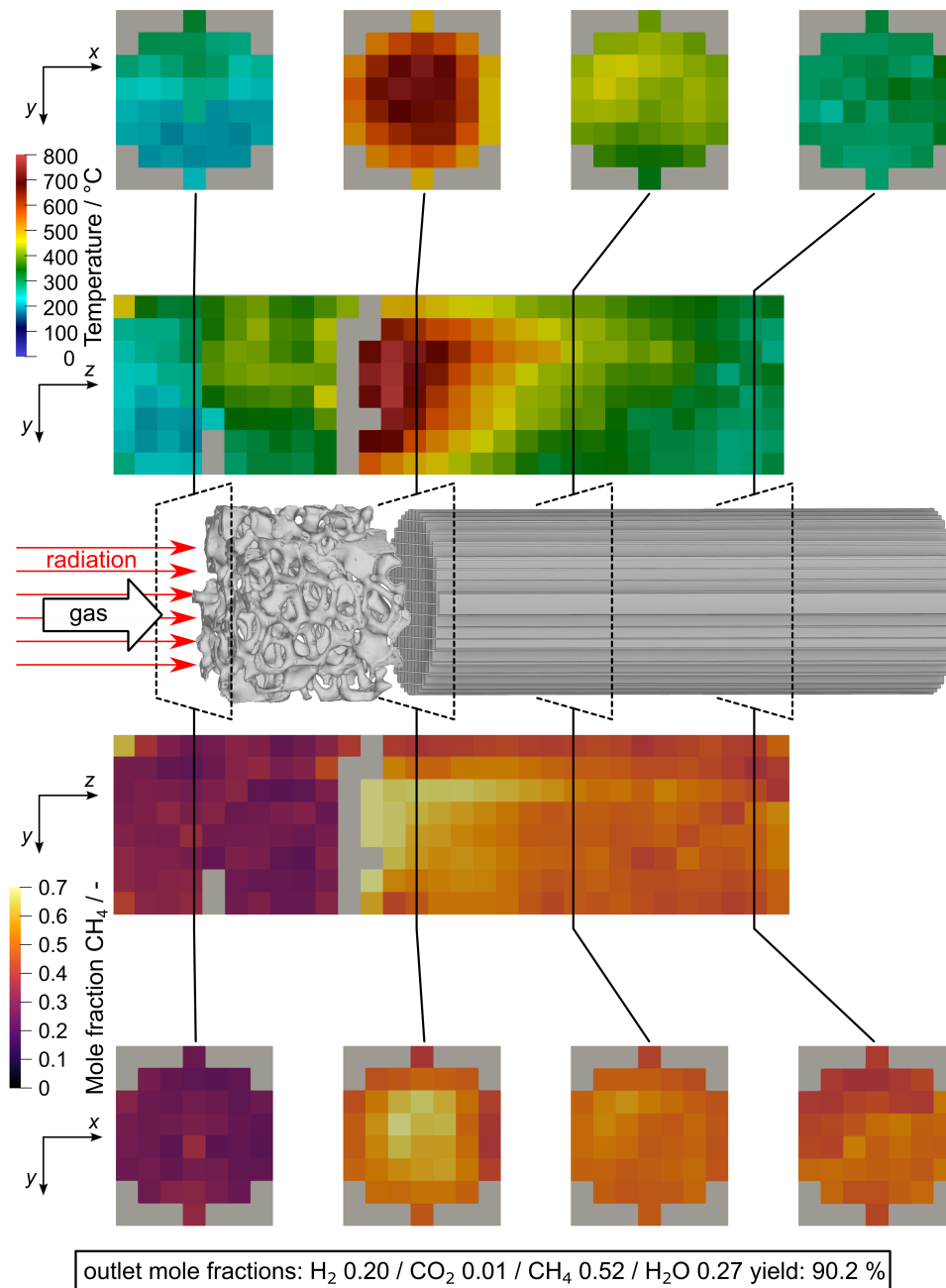
Figure 6.6: Results for the measurement of state #3. The measured temperature and mole fraction of methane are shown as individual images. For both, the central longitudinal slice (sagittal, x = const) through the reactor is shown. Further, four cross sectional slices are shown right before the monolithic sponge in the free gas phase, right after the monolithic sponge inside the honeycomb and in two more positions inside the honeycomb. For orientation the positions are indicated in comparison to 3D models of the measured objects. In gray voxels no data was fitted.
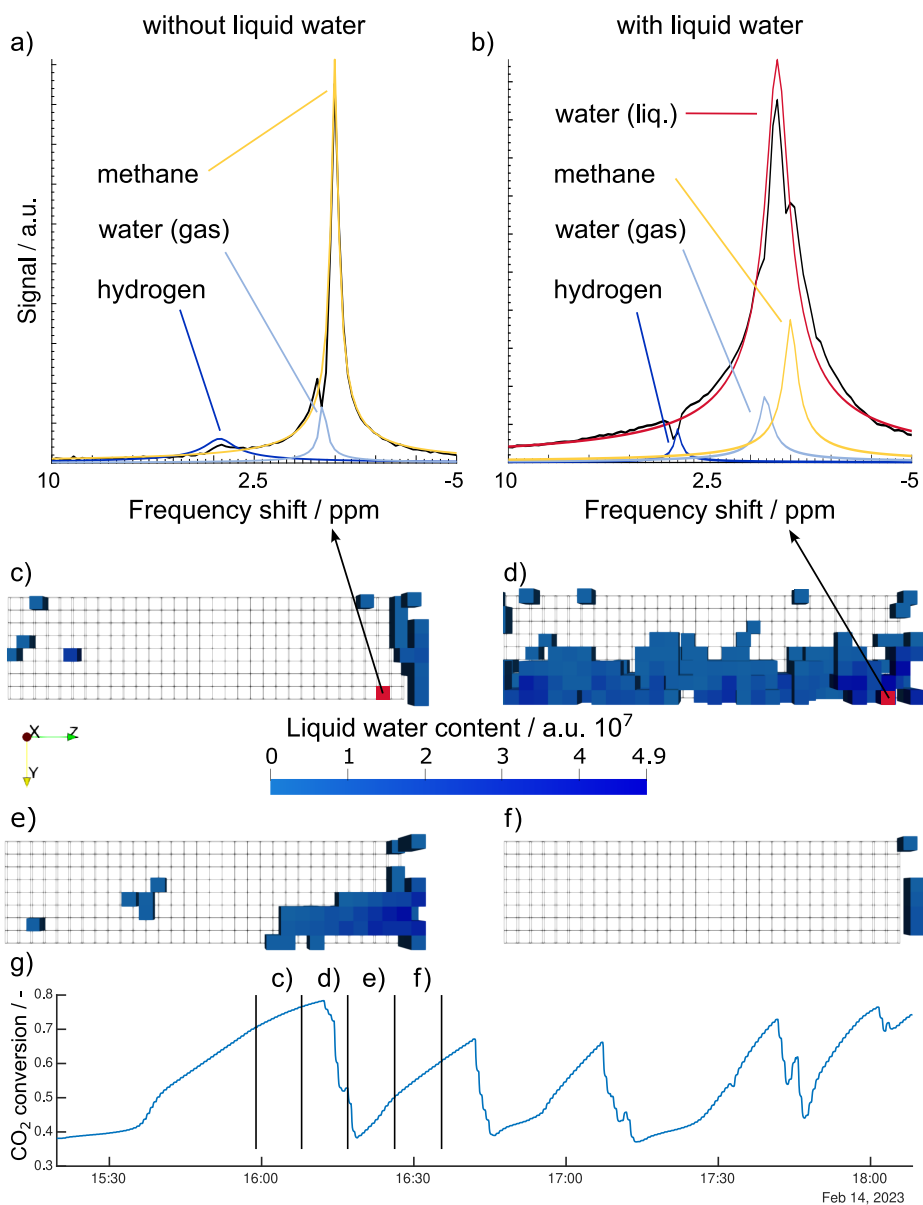
Figure 6.7: Comparison between four measurements with different water content. Frequency spectra (absolute values) without (a) and with (b) liquid water showing the additional signal appearing in some voxels. Voxel at identical position but from two consecutive measurements are shown. c-f) 3D depiction of formed liquid water inside the catalytically active honeycomb during the methanation reaction in four consecutive 3D-MRSI measurements (no T_1 measurement). Only voxel are shown, where liquid water was found. Gas flow is in z-direction. g) Results for the carbon dioxide conversion measured by the NDIR spectrometer at the gas outlet during the methanation reaction. The time window is between the T_1 measurement series of state #2 and state #3.

6.3 Liquid water

As described in the previous chapter, steady-state conditions could not be reached when the methanation reaction was not at full conversion. Using a heating rate of 65 or 70 W combined with a total volume flow of 2 NL/min, the carbon dioxide conversion and, thus, the reaction rate constantly changed, and an oscillatory behavior was observed. In the 3D-MRSI measurements performed during the non-steady reaction, an additional, prominent peak could be observed in some of the spectra of the honeycomb during phases of low reaction rate, as can be seen in Figure 6.7 a) and b). The unwanted signal is very broad and, thus, has a low T_2^*. Therefore, it could be separated from the other signals using MPM. In Figure 6.7 c-f), maps of the unwanted signal in four consecutive measurements are shown. The maps are side views of the measured honeycomb, and only the voxels are shown where a certain amount of this signal was found. Additionally, the results of the NDIR for the carbon dioxide conversion are shown in Figure 6.7 g). As the signal is large compared to methane (Figure 6.7 b), it is assumed that a liquid must have formed inside the reactor. The only substance that can be considered for this is water, which has the highest boiling point of all gases in the system.

The map in Figure 6.7 c) shows practically no liquid water. In the second map (d), the water covers the whole lower area. In the following two maps (e/f), the water is pushed back until it disappears from the visible region of the honeycomb. The appearance and disappearance of water can be witnessed several times from the 18 measurements made in between state #2 and state #3 (all measurements shown in Appendix B in Figure B.2 & B.3). The fact that T_2^* of water was so very low is an indicator that the liquid water was inside the porous wash coat, which is on top of the walls of the honeycomb walls. The wash coat is a porous region where the catalyst is deposited. It contains tiny pores with a high surface area. Water inside the wash coat experiences a high amount of wall contact through the high surface area, which decreases the relaxation times [86]. The presence of liquid water inside the porous region is further confirmed by the strong capillary forces that water experiences inside the pores. These forces work against the evaporation of water and, thus, increase the boiling point. As a result, the porous region will be the first region to be saturated with liquid water.

To explain the oscillatory behavior of the reaction, the presence of water inside the porous region is necessary. The liquid water decreases intra-pore diffusion, thus, the reaction rate decreases, and less heat is produced. With less heat, more

and more water will move into the liquid state inside the pores, and the reaction is decelerating even more. When the reaction rate is low, less water is formed by the reaction. Eventually, the hot inlet gas stream evaporates the water inside the pores, allowing the reaction to proceed and generate heat again. In the steady states observed using the CTD method, there was either enough heat inside the catalytically active honeycomb so that no water was condensing (states #1 & #3) or insufficient water formed to block the active sites (state #2).

In this thesis, we have seen different obstacles when observing the gas formed during the methanation reaction, like steady-state conditions, electrically conductive material, and field inhomogeneities. The fact that the heat from the laser is applied frontally at the same spot where the main reaction zone is promotes temperature gradients inside the object and the formation of liquid water. By this, it limits the observable parameter range. Still, the oscillatory behavior of the reaction is an interesting oddity that we could nicely observe using the given technique.

7

Conclusion and Outlook

In order to study the temperature and concentration of methane *operando* during the methanation reaction, a MRI-compatible setup, the Combined Temperature and Density (CTD) method, and boundary conditions for the application of MRI methods to gas-phase reactions have been developed in this thesis.

7.1 Conclusions

1. The **MRI reactor** specially designed for the application to heterogeneously catalyzed gas-phase reactions can withstand high temperatures and pressure, which usually cannot be reached inside MR magnets. The glass and alumina tubes featured in the observable region of the reactor have a negligible effect on the magnetic field and the magnetic field homogeneity in particular. Reaching temperatures over $800\,^\circ$C inside the reaction zone without permanent damage to the reactor exceeds our expectations. By combining the insulation around the reactor tube with air cooling of the MR coil and laser heating, high temperatures can be realized inside the reaction zone while the surrounding MR coil stays at manageable temperatures. The frontal heating of the reaction zone is not beneficial for many applications as it results in significant temperature gradients along the reactor tube. If it is desired to study the effect of heat conductivity of the supporting material on a chemical reaction, the measurements are already biased by the temperature gradient resulting purely from frontal heating. Secondly, a certain gas leak rate was always present during the reactor operation at increased temperatures. However, the gases accumulate in the insulation layer around the reactor tube, leading to additional measured signals. It was required to increase the field of view of the measurement to avoid an overlapping of different signals. Depending on the type and amount of leaking gas, the leakage may prove hazardous for the operating people.

2. The presented **Combined Temperature and Density (CTD)** measurement technique is a promising strategy to characterize gases inside chemical reactors. When the acquired signal is not disturbed by large magnetic field inhomogeneities, the combined usage of maximum signal amplitude A and longitudinal relaxation time T_1 of methane can visualize both the temperature and the mole fraction of methane independently from each other and with a high amount of repeatability. Noteworthy is the fact that the information can be obtained from the methane signal alone, even though it required a very defined set of boundary conditions. Disadvantages were mainly encountered in the measurement of T_1. The magnetic field inhomogeneity strongly influences the fitted T_1. Further, T_1 is affected by the presence of every different gas species, making the calculation of T_1 from theory very tedious. As the distribution of the remaining gases inside the reactor could not be measured spatially resolved, it was necessary to rely on the assumption of ideal gas distribution. For other chemical reactions it might be impossible to determine the gas distribution and the expected T_1 accurately. Further, the acquisition of the two cross-sectional parameters σ_{j,CH_4-H_2}, and σ_{j,CH_4-H_2O} was a time-consuming process. For most different gas systems, similar parameter studies would be required.

Aside from the issues experienced with T_1, the basic idea behind the method is a strong tool. Measuring two NMR parameters, temperature and density can be quantified independently. Very recently, the CTD method could be applied to the hydrogenation of ethylene in a yet-unpublished work. Instead of using T_1 of one of the gases present in the system, the ratio between the two carbonic species, ethane, and ethene, could be used to quantify the gas density, as was already done by Ulpts et al. [55]. By combining this information with the ratio of the maximum signal amplitude A/A_0, the temperature of the gases could also be extracted. In this case, the preparational effort was almost non-existent, and the measurement time could also be drastically reduced. Still, the method requires good knowledge about the studied system and how different NMR parameters are affected during the chemical reaction.

3. From the results of the **methanation reaction** shown in this work, regions of high methane yield could be identified and temperature hot spots quantified. Even though the chosen voxel size of $(3\,\mathrm{mm})^3$ is quite large and the resolution accordingly low, clear trends can be observed inside the reactive region. Natural convection is crucial, especially at the lower flow rate of $2\,\mathrm{NL/min}$.

The reactive region is shifted upwards. In front of the sponge, it can be seen how warm and less dense gas is moving against the flow direction while the cooler inlet gas is pushing in from below. The flow rate difference between the full conversion in state #1 and state #3 leads to significantly different results. It can clearly be seen how the increased amount of gas and reaction changes the temperature and mole fraction profiles. Apart from these important pieces of information, the potential to optimize a honeycomb catalyst support is relatively low, and further investigations might not offer substantial new insights. Other monolithic structures, like a sponge for catalyst support or a fixed bed of pellets, offer more parameters to optimize. They are inherently more inhomogeneous in their temperature and density distribution, making the application of this time-consuming and complex measurement technique more viable. However, as can be seen from the results in the uncoated sponge in front of the honeycomb, severe problems for the technique arise due to the massive magnetic field inhomogeneities. While it can be seen from the measurements of state #1 that feasible results are not impossible inside the sponge, the influence of magnetic field inhomogeneities on the quality of the results needs to be addressed in the future. A second drawback of the investigated system is the frontal heating which led to water formation inside the honeycomb structure and prevented a steady state at non-full conversion. The frontal heating limits the investigated parameter range. To deal with this limitation, it might be necessary to perform measurements at increased flow rates or use support materials with a higher axial thermal conductivity. However, the latter usually comes with a high electric conductivity, preventing these measurements completely.

Nonetheless, the application of the CTD method to the methanation was successful. It is a viable technique to investigate chemical reactions *operando* and spatially resolved, without making significant changes to the reaction system.

7.2 Outlook

So far, the method's application shown in this thesis is limited to investigations on honeycombs, as the structure offers a simple geometry with small influences on the measurement. It is necessary to investigate how disturbances like magnetic field inhomogeneities influence the measurement to overcome this limitation in the future.

It might be possible to find different monolithic structures with almost the same reactive parameters but with less magnetic field disturbance. Further, the results of the CTD method can be combined with computer simulations of chemical reactions. While MRI measurements can provide results of real applications and more accurate boundary conditions, computer simulations can be applied to reactor systems without the limitations mentioned above. The measurement results would not only offer guiding points for the validation of the simulations but provide their own unique set of information. So far, combined CFD/MRI approaches are only seen by the community as a comparison between the results of each method. Instead, it would be possible to create a combination of simulation and measurement parameters and feed these together into the calculation of final results. The calculation could be done by implementing the governing equations used in this work for T_1 and A into the simulation such that it can use the original MRI results without the need to convert them first into reaction parameters. This type of calculation allows incorporating a diffusion/reaction model into the processing of NMR parameters, greatly improving the calculation process as the assumption of ideal mixing could be omitted.

The presented work strongly emphasizes the possibilities available to use MRI to describe catalytic reaction processes in chemical reactors. Even though the application of MRI is not straightforward and requires much effort to consolidate new findings, it is an exciting field with many new topics to study. It can unlock a new and more profound understanding of transport processes and chemical reactions in general.

Bibliography

[1]   Harm Ridder, Christoph Sinn, Georg R. Pesch, Jan Ilsemann, Wolfgang Dreher, and Jorg Thöming. "A large fixed bed reactor for MRI operando experiments at elevated temperature and pressure". In: *Review of Scientific Instruments* 92.4 (2021), p. 043711. DOI: `10.1063/5.0044795`.

[2]   Harm Ridder, Christoph Sinn, Georg R. Pesch, Wolfgang Dreher, and Jorg Thöming. "Spatially resolved direct gas-phase thermometry in chemical reactors using NMR". In: *Chemical Engineering Journal* 433.September 2021 (2022), p. 133583. DOI: `10.1016/j.cej.2021.133583`.

[3]   Harm Ridder, Christoph Sinn, Georg R Pesch, Wolfgang Dreher, and Jorg Thöming. "Longitudinal Relaxation (T1) of Methane/Hydrogen Mixtures for Operando Characterization of Gas-Phase Reactions". In: *ACS Measurement Science Au* 2.5 (2022), pp. 449–456. DOI: `10.1021/acsmeasuresciau.2c00022`.

[4]   Mojtaba Mirdrikvand, Harm Ridder, Jorg Thöming, and Wolfgang Dreher. "Diffusion weighted magnetic resonance imaging for temperature measurements in catalyst supports with an axial gas flow". In: *Reaction Chemistry and Engineering* 4.10 (2019), pp. 1844–1853. DOI: `10.1039/c9re00082h`.

[5]   Georg R Pesch, Harm Ridder, and Christoph Sinn. "Operando characterization of heterogeneously catalyzed gas- and multi-phase reactions using nuclear magnetic resonance imaging". In: *Chemical Engineering and Processing - Process Intensification* 179.August (2022), p. 109086. DOI: `10.1016/j.cep.2022.109086`.

[6]   Hannah Ritchie. *Sector by sector: where do global greenhouse emissions come from?* 2020.

[7]   International Energy Agency. "The Future of Petrochemicals – Analysis". In: *International Energy Agency* (2018), pp. 11–25.

[8]   Markus Lehner, Robert Tichler, Horst Steinmüller, and Markus Koppe. *Power-to-Gas: Technology and Business Models*. Springer Cham, 2014, pp. 41–61. DOI: 10.1007/978-3-319-03995-4.

[9]   Vincent Dieterich, Alexander Buttler, Andreas Hanel, Hartmut Spliethoff, and Sebastian Fendt. " Power-to-liquid via synthesis of methanol, DME or Fischer–Tropsch-fuels: a review ". In: *Energy & Environmental Science* (2020), pp. 3207–3252. DOI: 10.1039/d0ee01187h.

[10]   Alberto Varone and Michele Ferrari. "Power to liquid and power to gas: An option for the German Energiewende". In: *Renewable and Sustainable Energy Reviews* 45 (2015), pp. 207–218. DOI: 10.1016/j.rser.2015.01.049.

[11]   Ib Chorkendorff and Johannes W. Niemantsverdriet. *Concepts of Modern Catalysis and Kinetics*. 3rd Editio. John Wiley & Sons, 2017, p. 505.

[12]   Melis S. Duyar, Arvind Ramachandran, Christine Wang, and Robert J. Farrauto. "Kinetics of CO2 methanation over Ru/γ-Al2O3 and implications for renewable energy storage applications". In: *Journal of CO2 Utilization* 12 (2015), pp. 27–33. DOI: 10.1016/j.jcou.2015.10.003.

[13]   J. Gascon, J. R. Van Ommen, J. A. Moulijn, and F. Kapteijn. "Structuring catalyst and reactor - An inviting avenue to process intensification". In: *Catalysis Science and Technology* 5.2 (2015), pp. 807–817. DOI: 10.1039/c4cy01406e.

[14]   Jonas Wentrup, Georg R Pesch, and Jorg Thöming. "Dynamic operation of Fischer-Tropsch reactors for power-to-liquid concepts: A review". In: *Renewable and Sustainable Energy Reviews* 162.October 2021 (2022), p. 112454. DOI: 10.1016/j.rser.2022.112454.

[15]   Timo Engl, Moritz Langer, Hannsjörg Freund, Michael Rubin, and Roland Dittmeyer. "Tap Reactor for Temporally and Spatially Resolved Analysis of the CO2 Methanation Reaction". In: *Chemie-Ingenieur-Technik* 5 (2023), pp. 658–667. DOI: 10.1002/cite.202200204.

[16]   Oliver Korup, Sardor Mavlyankariev, Michael Geske, Claude Franklin Goldsmith, and Raimund Horn. "Measurement and analysis of spatial reactor profiles in high temperature catalysis research". In: *Chemical Engineering and Processing: Process Intensification* 50.10 (2011), pp. 998–1009. DOI: 10.1016/j.cep.2011.05.024.

[17] Ying Dong, Michael Geske, Oliver Korup, Nils Ellenfeld, Frank Rosowski, Cornelia Dobner, and Raimund Horn. "What happens in a catalytic fixed-bed reactor for n-butane oxidation to maleic anhydride? Insights from spatial profile measurements and particle resolved CFD simulations". In: *Chemical Engineering Journal* 350.May (2018), pp. 799–811. DOI: `10.1016/j.cej.2018.05.192`.

[18] Barbara Stuart. "Infrared Spectroscopy". In: *Kirk-Othmer Encyclopedia of Chemical Technology* (2015), pp. 1–18. DOI: `https://doi.org/10.1002/0471238961.0914061810151405.a01.pub3`.

[19] Olga B. Lapina. "Modern ssNMR for heterogeneous catalysis". In: *Catalysis Today* 285 (2017), pp. 179–193. DOI: `10.1016/j.cattod.2016.11.005`.

[20] J. J. Van Der Klink. "NMR Spectroscopy as a Probe of Surfaces of Supported Metal Catalysts". In: *Advances in Catalysis* 44.C (1999), pp. 1–117. DOI: `10.1016/S0360-0564(08)60512-X`.

[21] Lynn F. Gladden, Fernando J.R. Abegão, Christopher P. Dunckley, Daniel J. Holland, Mark H. Sankey, and Andrew J. Sederman. "MRI: Operando measurements of temperature, hydrodynamics and local reaction rate in a heterogeneous catalytic reactor". In: *Catalysis Today* 155.3-4 (2010), pp. 157–163. DOI: `10.1016/j.cattod.2009.10.012`.

[22] Siegfried Stapf and Song-i Han, eds. *NMR Imaging in Chemical Engineering*. 2007, p. 620. DOI: `10.1016/s1351-4180(07)70357-4`.

[23] Kirill V. Kovtunov, Oleg G. Salnikov, Vladimir V. Zhivonitko, Ivan V. Skovpin, Valerii I. Bukhtiyarov, and Igor V. Koptyug. "Catalysis and Nuclear Magnetic Resonance Signal Enhancement with Parahydrogen". In: *Topics in Catalysis* 59.19-20 (2016), pp. 1686–1699. DOI: `10.1007/s11244-016-0688-6`.

[24] Mehrdad Sadeghi, Mojtaba Mirdrikvand, Georg R. Pesch, Wolfgang Dreher, and Jorg Thöming. "Full-field analysis of gas flow within open-cell foams: comparison of micro-computed tomography-based CFD simulations with experimental magnetic resonance flow mapping data". In: *Experiments in Fluids* 61.5 (2020), pp. 1–16. DOI: `10.1007/s00348-020-02960-4`.

[25] Andrew J. Onstad, Christopher J. Elkins, Frank Medina, Ryan B. Wicker, and John K. Eaton. "Full-field measurements of flow through a scaled metal foam replica". In: *Experiments in Fluids* 50.6 (2011), pp. 1571–1585. DOI: `10.1007/s00348-010-1008-8`.

[26] Philip Kemper, Ekkehard Küstermann, Wolfgang Dreher, Thorben Helmers, Ulrich Mießner, Benjamin Besser, and Jorg Thöming. "Magnetic Resonance Imaging for Non-invasive Study of Hydrodynamics Inside Gas-Liquid Taylor Flows". In: *Chemical Engineering and Technology* 3 (2021), pp. 465–476. DOI: 10.1002/ceat.202000509.

[27] Petrik Galvosas and Paul T. Callaghan. "Fast magnetic resonance imaging and velocimetry for liquids under high flow rates". In: *Journal of Magnetic Resonance* 181.1 (2006), pp. 119–125. DOI: 10.1016/j.jmr.2006.03.020.

[28] A. Penn, C. M. Boyce, K. P. Pruessmann, and C. R. Müller. "Regimes of jetting and bubbling in a fluidized bed studied using real-time magnetic resonance imaging". In: *Chemical Engineering Journal* 383.June (2020), p. 123185. DOI: 10.1016/j.cej.2019.123185.

[29] Carmine D'Agostino, Gemma L. Brett, Peter J. Miedziak, David W. Knight, Graham J. Hutchings, Lynn F. Gladden, and Mick D. Mantle. "Understanding the solvent effect on the catalytic oxidation of 1,4-butanediol in methanol over Au/TiO 2 catalyst: NMR diffusion and relaxation studies". In: *Chemistry - A European Journal* 18.45 (2012), pp. 14426–14433. DOI: 10.1002/chem.201201922.

[30] Mark A. Isaacs, Neil Robinson, Brunella Barbero, Lee J. Durndell, Jinesh C. Manayil, Christopher M.A. Parlett, Carmine D'Agostino, Karen Wilson, and Adam F. Lee. "Unravelling mass transport in hierarchically porous catalysts". In: *Journal of Materials Chemistry A* 7.19 (2019), pp. 11814–11825. DOI: 10.1039/c9ta01867k.

[31] Igor V. Koptyug. *Magnetic resonance imaging methods in heterogeneous catalysis*. Vol. 45. 2014, pp. 1–42. DOI: 10.1039/9781782621485-00001.

[32] Jürgen Ulpts, Lars Kiewidt, Wolfgang Dreher, and Jorg Thöming. "3D characterization of gas phase reactors with regularly and irregularly structured monolithic catalysts by NMR imaging and modeling". In: *Catalysis Today* 310 (2018), pp. 176–186. DOI: 10.1016/j.cattod.2017.05.009.

[33] L. Baker, M.P. Renshaw, M.D. Mantle, A.J. Sederman, A.J. Wain, and L.F. Gladden. "Operando Magnetic Resonance Studies of Phase Behaviour and Oligomer Accumulation Within Catalyst Pores During Heterogeneous Catalytic Ethene Oligomerization". In: *Applied Catalysis A: General* 557 (2018), pp. 125–134. DOI: 10.1016/j.apcata.2018.03.011.

[34]   Qingyuan Zheng, Jack Williams, Léonard R. van Thiel, Scott V. Elgersma, Mick D. Mantle, Andrew J. Sederman, Timothy A. Baart, G. Leendert Bezemer, Constant M. Guédon, and Lynn F. Gladden. "Operando magnetic resonance imaging of product distributions within the pores of catalyst pellets during Fischer–Tropsch synthesis". In: *Nature Catalysis* 6.February (2023). DOI: 10.1038/s41929-023-00913-8.

[35]   Lars Kiewidt and Jorg Thöming. "Pareto-optimal design and assessment of monolithic sponges as catalyst carriers for exothermic reactions". In: *Chemical Engineering Journal* 359 (2019), pp. 496–504. DOI: 10.1016/j.cej.2018.11.109.

[36]   Mauro Bracconi, Matteo Ambrosetti, Matteo Maestri, Gianpiero Groppi, and Enrico Tronconi. "A fundamental analysis of the influence of the geometrical properties on the effective thermal conductivity of open-cell foams". In: *Chemical Engineering and Processing - Process Intensification* 129.March (2018), pp. 181–189. DOI: 10.1016/j.cep.2018.04.018.

[37]   Robert Guettel, Ulrich Kunz, and Thomas Turek. "Reactors for Fischer-Tropsch synthesis". In: *Chemical Engineering and Technology* 31.5 (2008), pp. 746–754. DOI: 10.1002/ceat.200800023.

[38]   Stefan Rönsch, Jens Schneider, Steffi Matthischke, Michael Schlüter, Manuel Götz, Jonathan Lefebvre, Praseeth Prabhakaran, and Siegfried Bajohr. "Review on methanation - From fundamentals to current projects". In: *Fuel* 166 (2016), pp. 276–296. DOI: 10.1016/j.fuel.2015.10.111.

[39]   Leonard Uchejim Okonye, Yali Yao, Diane Hildebrandt, and Reinout Meijboom. "Contributing to energy sustainability: A review of mesoporous material supported catalysts for Fischer-Tropsch synthesis". In: *Sustainable Energy and Fuels* 5.1 (2021), pp. 79–107. DOI: 10.1039/d0se01442g.

[40]   Zhouxin Luo, Guoqiang Zhao, Hongge Pan, and Wenping Sun. "Strong Metal–Support Interaction in Heterogeneous Catalysts". In: *Advanced Energy Materials* 12.37 (2022), pp. 1–15. DOI: 10.1002/aenm.202201395.

[41]   H. Scott Fogler. *Elements of Chemical Reaction Engineering*. Pearson Educacion, 1999, p. 967.

[42]   Robin Mutschler, Emanuele Moioli, Kun Zhao, Loris Lombardo, Emad Oveisi, Alessandro Porta, Leonardo Falbo, Carlo Giorgio Visconti, Luca Lietti, and Andreas Züttel. "Imaging Catalysis: Operando Investigation of the CO2

Hydrogenation Reaction Dynamics by Means of Infrared Thermography". In: *ACS Catalysis* 10.3 (2020), pp. 1721–1730. DOI: `10.1021/acscatal.9b04475`.

[43] Jose A. Hernandez Lalinde, Kevin Kofler, Xuejie Huang, and Jan Kopyscinski. "Improved kinetic data acquisition using an optically accessible catalytic plate reactor with spatially-resolved measurement techniques. Case of study: CO2 methanation". In: *Catalysts* 8.2 (2018). DOI: `10.3390/catal8020086`.

[44] Bruker. *60 Years of Innovation*. 2023.

[45] R. G. Henderson. "Nuclear magnetic resonance imaging: A review". In: *Journal of the Royal Society of Medicine* 76.3 (1983), pp. 206–212. DOI: `10.1177/014107688307600312`.

[46] Don Bradley and Kendall E. Bradley. "The value of diagnostic medical imaging." In: *North Carolina medical journal* 75.2 (2014), pp. 121–125. DOI: `10.18043/ncm.75.2.121`.

[47] Qingyuan Zheng, Jacob L. Brown, Mick D. Mantle, Andrew J. Sederman, Timothy A. Baart, Constant M. Guédon, and Lynn F. Gladden. "Water-wax behaviour in porous silica at low temperature Fischer-Tropsch conditions". In: *Applied Catalysis A: General* 572.September 2018 (2019), pp. 142–150. DOI: `10.1016/j.apcata.2018.11.022`.

[48] Markus Leutzsch, Andrew J. Sederman, Lynn F. Gladden, and Michael D. Mantle. "In situ reaction monitoring in heterogeneous catalysts by a benchtop NMR spectrometer". In: *Magnetic Resonance Imaging* 56.September (2019), pp. 138–143. DOI: `10.1016/j.mri.2018.09.006`.

[49] Jack Williams, Qingyuan Zheng, Andrew J. Sederman, Mick D. Mantle, Timothy Baart, Constant Guédon, and Lynn F. Gladden. "In Situ Determination of Carbon Number Distributions of Mixtures of Linear Hydrocarbons Confined within Porous Media Using Pulsed Field Gradient NMR". In: *Analytical Chemistry* 92.7 (2020), pp. 5125–5133. DOI: `10.1021/acs.analchem.9b05600`.

[50] Léonard R Van Thiel. "NMR Studies of Emulsions in Porous Media and Applications to Fischer-Tropsch Synthesis". PhD thesis. University of Cambridge, 2019, p. 227. DOI: `10.17863/CAM.51375`.

[51] Jaap A. Bergwerff, Anna A. Lysova, Leticia Espinosa-Alonso, Igor V. Koptyug, and Bert M. Weckhuysen. "Monitoring transport phenomena of paramagnetic metal-ion complexes inside catalyst bodies with magnetic resonance imaging". In: *Chemistry - A European Journal* 14.8 (2008), pp. 2363–2374. DOI: 10.1002/chem.200700990.

[52] Igor V. Koptyug, Stephen A. Altobelli, Eiichi Fukushima, Anatoly V. Matveev, and Renad Z. Sagdeev. "Thermally Polarized 1H NMR Microimaging Studies of Liquid and Gas Flow in Monolithic Catalysts". In: *Journal of Magnetic Resonance* 147.1 (2000), pp. 36–42. DOI: 10.1006/jmre.2000.2186.

[53] Anna A. Lysova, Alexander V. Kulikov, Valentin N. Parmon, Renad Z. Sagdeev, and Igor V. Koptyug. "Quantitative temperature mapping within an operating catalyst by spatially resolved 27Al NMR". In: *Chemical Communications* 48.46 (2012), pp. 5763–5765. DOI: 10.1039/c2cc31260c.

[54] Elizaveta S. Kononenko, Alexandra I. Svyatova, Ivan V. Skovpin, Larisa M. Kovtunova, Evgeny Yu Gerasimov, and Igor V. Koptyug. "Getting the Most out of Parahydrogen-Induced Signal Enhancement for MRI of Reacting Heterogeneous Systems". In: *Journal of Physical Chemistry C* 126.35 (2022), pp. 14914–14921. DOI: 10.1021/acs.jpcc.2c05218.

[55] Jürgen Ulpts, Wolfgang Dreher, Lars Kiewidt, Miriam Schubert, and Jorg Thöming. "In situ analysis of gas phase reaction processes within monolithic catalyst supports by applying NMR imaging methods". In: *Catalysis Today* 273 (2016), pp. 91–98. DOI: 10.1016/j.cattod.2016.02.062.

[56] Jürgen Ulpts, Wolfgang Dreher, Miriam Klink, and Jorg Thöming. "NMR imaging of gas phase hydrogenation in a packed bed flow reactor". In: *Applied Catalysis A: General* 502 (2015), pp. 340–349. DOI: 10.1016/j.apcata.2015.06.011.

[57] Mojtaba Mirdrikvand, Mehrdad Sadeghi, Georg R. Pesch, Wolfgang Dreher, and Jorg Thöming. "Full-field comparison of MRV and CFD of gas flow through regular catalytic monolithic structures". In: *Processes* 9.3 (2021), pp. 1–22. DOI: 10.3390/pr9030566.

[58] Alexander Penn, Christopher M. Boyce, Thomas Kovar, Takuya Tsuji, Klaas P. Pruessmann, and Christoph R. Müller. "Real-Time Magnetic Resonance Imaging of Bubble Behavior and Particle Velocity in Fluidized Beds". In: *Industrial and Engineering Chemistry Research* 57.29 (2018), pp. 9674–9682. DOI: 10.1021/acs.iecr.8b00932.

[59] M. Raquel Serial, Stefan Benders, Perrine Rotzetter, Daniel L. Brummerloh, Jens P. Metzger, Simon P. Gross, Jennifer Nussbaum, Christoph R. Müller, Klaas P. Pruessmann, and Alexander Penn. "Temperature distribution in a gas-solid fixed bed probed by rapid magnetic resonance imaging". In: *Chemical Engineering Science* 269.118457 (2023). DOI: `10.1016/j.ces.2023.118457`. arXiv: `2211.13599`.

[60] Franz Koschany, David Schlereth, and Olaf Hinrichsen. "On the kinetics of the methanation of carbon dioxide on coprecipitated NiAl(O)<inf>x</inf>". In: *Applied Catalysis B: Environmental* 181 (2016), pp. 504–516. DOI: `10.1016/j.apcatb.2015.07.026`.

[61] A. Abragam. *The Principles of Nuclear Magnetism*. 32nd ed. Vol. 29. 12. Oxford university press, 1961, pp. 860–861. DOI: `10.1119/1.1937646`.

[62] National Institute of Standards and Technology. *CODATA Value: proton gyromagnetic ratio*. 2023.

[63] William M. Spees, Sheng Kwei Song, Joel R. Garbow, Jeffrey J. Neil, and Joseph J.H. Ackerman. "Use of ethylene glycol to evaluate gradient performance in gradient-intensive diffusion MR sequences". In: *Magnetic Resonance in Medicine* 68.1 (2012), pp. 319–324. DOI: `10.1002/mrm.23201`. arXiv: `NIHMS150003`.

[64] W. G. Schneider, H. J. Bernstein, and J. A. Pople. "Proton magnetic resonance chemical shift of free (Gaseous) and associated (Liquid) hydride molecules". In: *The Journal of Chemical Physics* 28.4 (1958), pp. 601–607. DOI: `10.1063/1.1744199`.

[65] Saman Alavi, J. A. Ripmeester, and D. D. Klug. "NMR shielding constants for hydrogen guest molecules in structure II clathrates". In: *Journal of Chemical Physics* 123.5 (2005), pp. 1–4. DOI: `10.1063/1.2000258`.

[66] J. C. Hindman. "Proton resonance shift of water in the gas and liquid states". In: *The Journal of Chemical Physics* 44.12 (1966), pp. 4582–4592. DOI: `10.1063/1.1726676`.

[67] Keith Wachowicz. "Evaluation of active and passive shimming in magnetic resonance imaging". In: *Research and Reports in Nuclear Medicine* 4 (2014), pp. 1–12. DOI: `10.2147/rrnm.s46526`.

[68] F. Zaera and G. A. Somorjai. "Hydrogenation of Ethylene over Platinum (111) Single-Crystal Surfaces". In: *Journal of the American Chemical Society* 106.8 (1984), pp. 2288–2293. DOI: `10.1021/ja00320a013`.

[69] Yung Ya Lin, Paul Hodgkinson, Matthias Ernst, and Alexander Pines. "A Novel Detection-Estimation Scheme for Noisy NMR Signals: Applications to Delayed Acquisition Data". In: *Journal of Magnetic Resonance* 128.1 (1997), pp. 30–41. DOI: `10.1006/jmre.1997.1215`.

[70] Cynthia J. Jameson and A. Keith Jameson. "Angular momentum relaxation in binary collisions. Comparison of cross sections". In: *The Journal of Chemical Physics* 93.5 (1990), pp. 3237–3244. DOI: `10.1063/1.458856`.

[71] R. L. Armstrong. "Longitudinal Nuclear Spin Relaxation Time Measurements in Molecular Gases". In: *Introductory Essays* (1976), pp. 71–95. DOI: `10.1007/978-3-642-66395-6_7`.

[72] Peter Adrian Beckmann. "Nuclear Spin Relaxation in Methane Gas". PhD thesis. PhD [dissertation]. University of British Columbia, 1975.

[73] M. Bloom, I. Oppenheim, M. Lipsicas, C. G. Wade, and C. F. Yarnell. "Nuclear spin relaxation in gases and liquids. IV. Interpretation of experiments in gases". In: *The Journal of Chemical Physics* 43.3 (1965), pp. 1036–1047. DOI: `10.1063/1.1696816`.

[74] P. H. Oosting and N. J. Trappeniers. "Proton-spin-lattice relaxation and self-diffusion in methanes. III. Interpretation of Proton-Spin-Lattice Relaxation Experiments". In: *Physica* 51.3 (1971), pp. 395–417. DOI: `10.1016/0031-8914(71)90050-4`.

[75] Ronald Y. Dong and Myer Bloom. "Determination of spin–rotation interaction constants in fluorinated methane molecules by means of nuclear spin relaxation measurements". In: *Canadian Journal of Physics* 48.6 (1970), pp. 793–804. DOI: `10.1139/p70-100`.

[76] Cynthia J. Jameson, A. Keith Jameson, Nancy C. Smith, J. K. Hwang, and Tasneem Zia. "13C and 1H spin relaxation in CH4 in the gas phase". In: *Journal of Physical Chemistry* 95.3 (1991), pp. 1092–1098. DOI: `10.1021/j100156a015`.

[77] P. M. Singer, D. Asthagiri, W. G. Chapman, and G. J. Hirasaki. "NMR spin-rotation relaxation and diffusion of methane". In: *Journal of Chemical Physics* 148.20 (2018). DOI: `10.1063/1.5027097`. arXiv: `1802.10191`.

[78] R. G. Gordon. "Kinetic theory of nuclear spin relaxation in gases". In: *The Journal of Chemical Physics* 44.1 (1966), pp. 228–234. DOI: 10.1063/1.1726451.

[79] Matthew D. Robson, John C. Gore, and R. Todd Constable. "Measurement of the point spread function in MRI using constant time imaging". In: *Magnetic Resonance in Medicine* 38.5 (1997), pp. 733–740. DOI: 10.1002/mrm.1910380509.

[80] *Methane - NIST Chemistry WebBook*. 2022.

[81] *Hydrogen - NIST Chemistry WebBook*. 2022.

[82] Malte Lorenz, Daniel Malangré, Fei Du, Michael Baune, Jorg Thöming, and Georg R Pesch. "High-throughput dielectrophoretic filtration of sub-micron and micro particles in macroscopic porous materials". In: *Analytical and Bioanalytical Chemistry* 412.16 (2020), pp. 3903–3914. DOI: 10.1007/s00216-020-02557-0.

[83] Fadi Alnaimat, Sawsan Dagher, Bobby Mathew, Ali Hilal-Alnqbi, and Saud Khashan. "Microfluidics Based Magnetophoresis: A Review". In: *Chemical Record* 18.11 (2018), pp. 1596–1612. DOI: 10.1002/tcr.201800018.

[84] Jasper Giesler, Laura Weirauch, Jorg Thöming, Michael Baune, and Georg R. Pesch. "Separating microparticles by material and size using dielectrophoretic chromatography with frequency modulation". In: *Scientific Reports* 11.1 (2021), pp. 1–12. DOI: 10.1038/s41598-021-95404-w.

[85] Rei Yu Chein and Chih Chang Wang. "Experimental study on co2 methanation over ni/al2o3, ru/al2o3, and ru-ni/al2o3 catalysts". In: *Catalysts* 10.10 (2020), pp. 1–17. DOI: 10.3390/catal10101112.

[86] Ingo Bardenhagen, Wolfgang Dreher, Daniela Fenske, Arne Wittstock, and Marcus Bäumer. "Fluid distribution and pore wettability of monolithic carbon xerogels measured by 1H NMR relaxation". In: *Carbon* 68 (2014), pp. 542–552. DOI: 10.1016/j.carbon.2013.11.033.

[87] Caleb Bell. *Thermo Python Package*. Cambridge, USA, 2021. DOI: 10.5281/zenodo.4892196.

A
Description of the glass tube preparation procedure

Creating defined mixtures of water vapor and methane inside a measurement setup is no easy task, as it requires temperatures of at least $100\,°C$. Further, the amount of water required to match the number of molecules of the gaseous methane is very low. In an open system, where – especially inside an MR scanner – temperature gradient along the measurement setup are inevitable, it is very difficult to ensure that the exact local molecule ratio of methane and vapor is known. As a solution to this, a procedure was developed to fixate a known amount of water and methane inside a sealed glass tube. The procedure utilizes the fact that water is liquid at room temperature while methane is gaseous to be able to bring the two substances into the tube one after another. The filling procedure consisted of the following steps (Figure A.1):

1) fill water into the bottom of the glass tube

2) freeze water inside the glass tube by bringing the tube into a bath of undercooled water

3) connect the glass tube to the vacuum pump and gas supply while completely covered inside the bath of undercooled water

4) iteratively draw vacuum and then replace the missing gas with methane to remove the air inside the glass tube

5) set a defined pressure of methane in the glass tube

6) seal the valve at the glass tube and then remove the bath of undercooled water

7) dry the glass tube using a towel

8) put the lower third of the glass tube in a bath of liquid nitrogen to solidify the methane inside the glass tube

9) seal the glass tube using a blow torch

Before the start of the filling procedure, one end of the tube was already sealed. First, the water is filled into the tube using a $10\,\mu L$ syringe which is typically used for gas chromatographic applications extended by a small tube to be able to reach the bottom of the tube (Step 1). Afterwards the glass tube is almost completely sunk in a bath of undercooled water ($-7\,°C$ to $-2\,°C$, using NaCl) to freeze the water inside the glass tube (Step 2). The tube is then connected to a small tube array connecting the glass tube to a vacuum pump and a methane supply (Step 3). The connections to the pump and the gas supply are opened sequentially to draw vacuum and then resupply the removed gas with methane. This way, the remaining air inside the tube could be reduced to a marginal amount, even though the vacuum pump did only reach down to a pressure of $80\,mbar$a (Step 4). In the next step, the pressure regulator of methane was used to set a defined methane pressure inside the glass tube (Step 5). The pressure was checked using two different pressure sensors, one
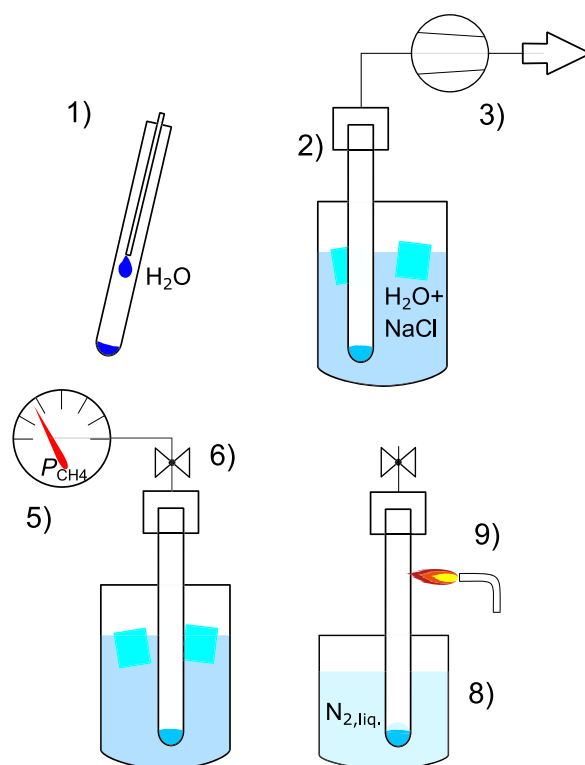

Figure A.1: Scheme of the different steps involved in sealing methane and water inside glass tubes.

for pressure below ambience and one for pressure above ambience. The resulting pressure is necessary for the calculation of the amount of methane inside the tube. When the desired pressure was reached, the valve near the glass tube was sealed and the bath of undercooled water was removed (Step 6). After drying the tube (Step 7), its lower part was emerged in a bath of liquid nitrogen (Step 8). As a result, solid methane was formed at the bottom of the tube. This ensured that the pressure inside the glass tube was below ambient pressure which allows to seal the tube using a blow torch even when a higher pressure was applied before (Step 9). Though different approaches to sealing water and methane inside a glass tube are theoretically possible, the presented procedure has the benefit that the ratio of water and methane inside the tube is not dependent on the final length of the glass tube which was a quite hard to control parameter as the sealing process was manual. The amount of water inside the glass tube was calculated as

$$ n_{H_2O} = \frac{V_{H_2O,liq.}}{V_{m,H_2O,STP}}, \tag{A.1} $$

with the volume of water in liquid form $V_{H_2O,liq.}$ and the molar volume of water at standard temperature and pressure $V_{m,H_2O,STP} = 1.807 \times 10^{-5} \, \mathrm{m^3 \, mol^{-1}}$ provided by the thermo package for python [87]. The amount of methane was calculated from the ideal gas law

$$ n_{CH_4} = \frac{V p_{CH_4}}{RT}, \tag{A.2} $$

where V denotes the volume of the glass tube plus the volume of the tubes before the valve, p_{CH_4} is the measured pressure of methane inside the glass tube, $R = 8.314 \, \mathrm{J \, mol^{-1} \, K^{-1}}$ is the gas constant and T the temperature of the under cooled water. The final pressure dependent on the temperature was calculated using the flasher procedure from the thermo python package [87]. A difficulty of this procedure was to get the exact information on how much water was brought into the glass tube. For the used combinations of water and methane only 0.6 to 13 µL of liquid water was required. The smallest available item to inject the water into the tube was a 10 µL syringe with a scale of 0.2 µL. As a result, amounts of water below 1 µL could only be extracted with reduced accuracy. Further, the amount of water is less than is required to form a drop of water. As a result of the surface tension of the water it could not be ensured that all of the water that was squeezed out of the syringe really stuck to the glass tube's wall. As in this application the exact ratio between methane and water was determined from MRI measurements, the uncertain amount of water did not change the results of this study.

B

Additional information

Original reactor design

gas inlet   fiber glass rods   double wall glass tube
for coil insulation   outlet for coolant

inlet for coolant   O-rings   ceramic tube   O-rings   gas/liquid outlet

Reactor design adapted for laser application

single wall glass tube   no coolant used/
semi-adiabatic

isolation layer
(not shown here)

large inlet for laser radiation
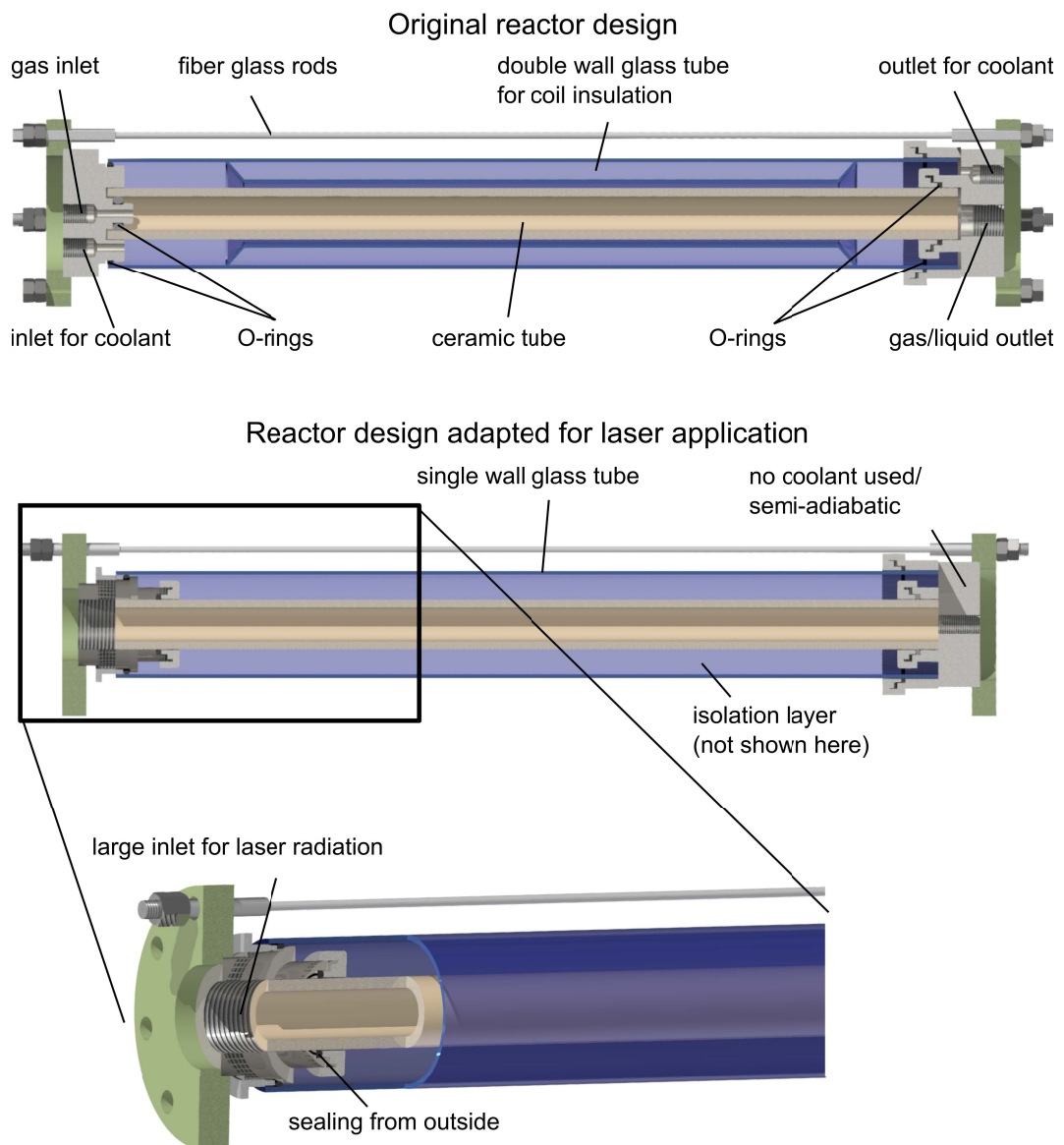
sealing from outside

Figure B.1: Comparison of the features of the original MRI reactor and the last version designed for laser heating. The idea to use a coolant inside the glass tube was abolished as the coolant inlet needed to be removed in the new flange.

Figure B.2: 3D depiction of formed liquid water inside the catalytically active honeycomb during the methanation reaction in eighteen consecutive 3D-MRSI measurements (no T_1 measurement). Only voxel are shown, where liquid water was found. Gas flow is in z-direction. As reference, the results for the CO_2 conversion measured by the NDIR spectrometer at the gas outlet during the methanation reaction are shown. The time window is between the T_1 measurement series of state #2 and state #3.
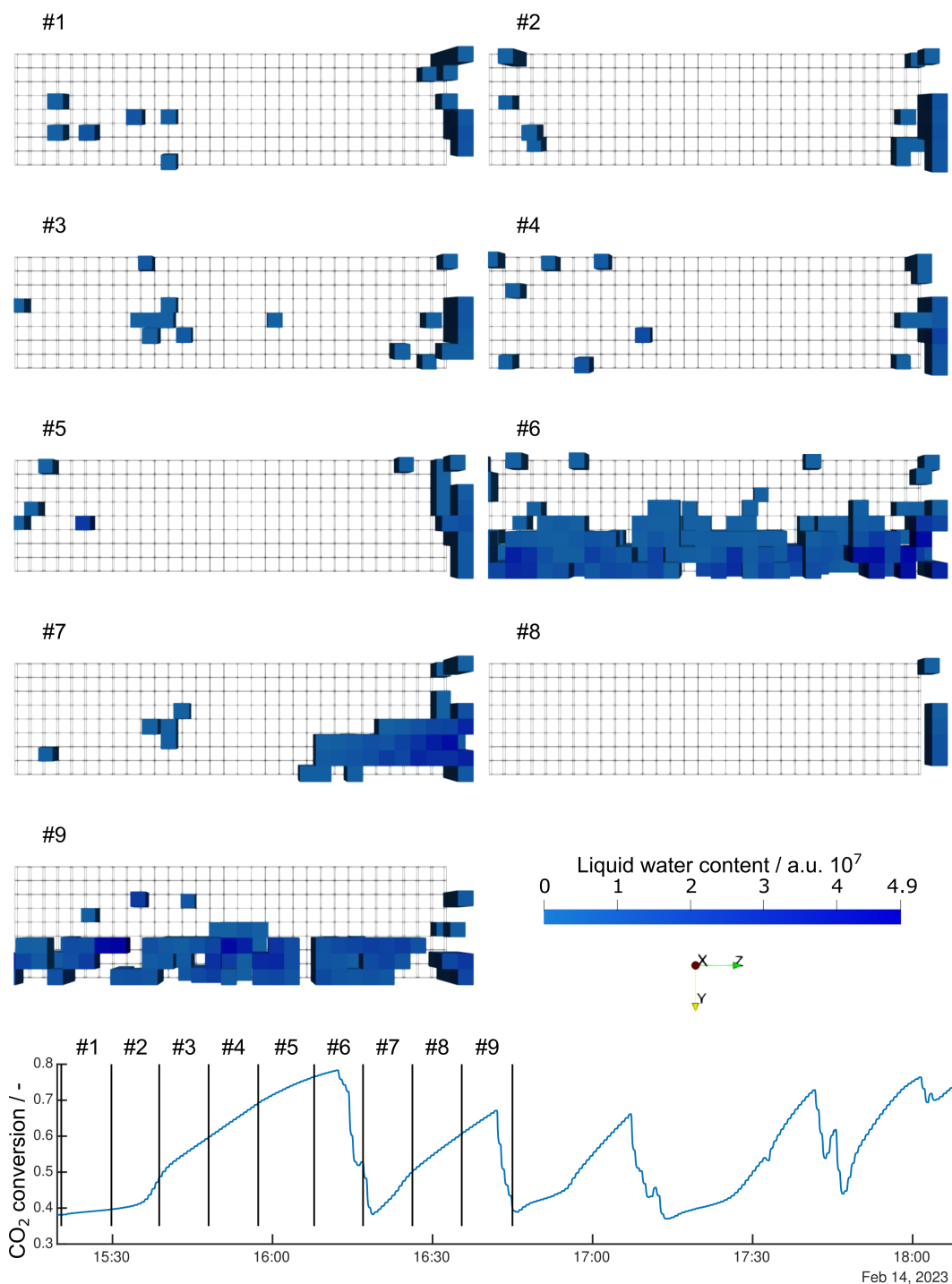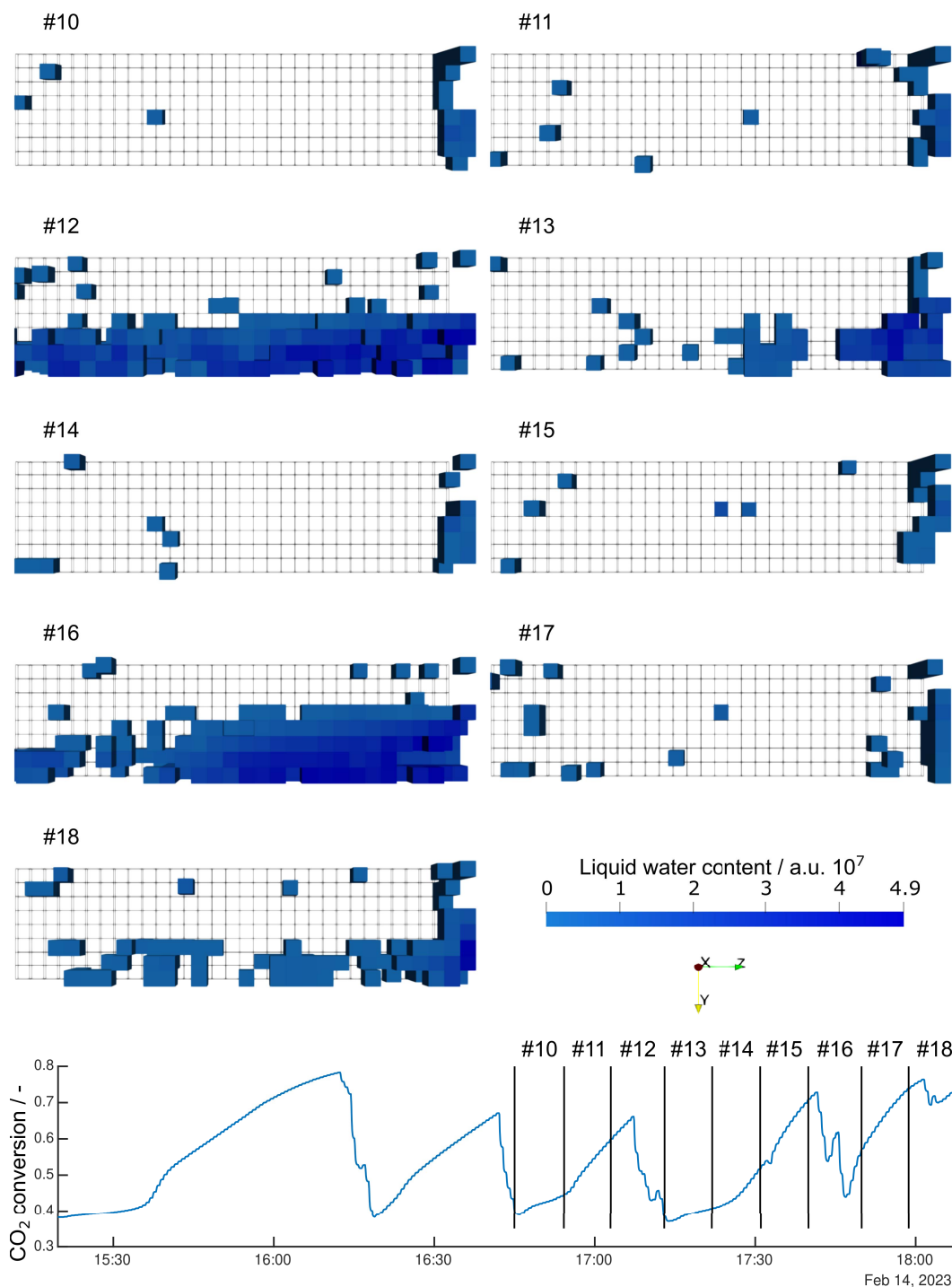
Figure B.3: 3D depiction of formed liquid water inside the catalytically active honeycomb during the methanation reaction in eighteen consecutive 3D-MRSI measurements (no T_1 measurement). Only voxel are shown, where liquid water was found. Gas flow is in z-direction. As reference, the results for the CO_2 conversion measured by the NDIR spectrometer at the gas outlet during the methanation reaction are shown. The time window is between the T_1 measurement series of state #2 and state #3.
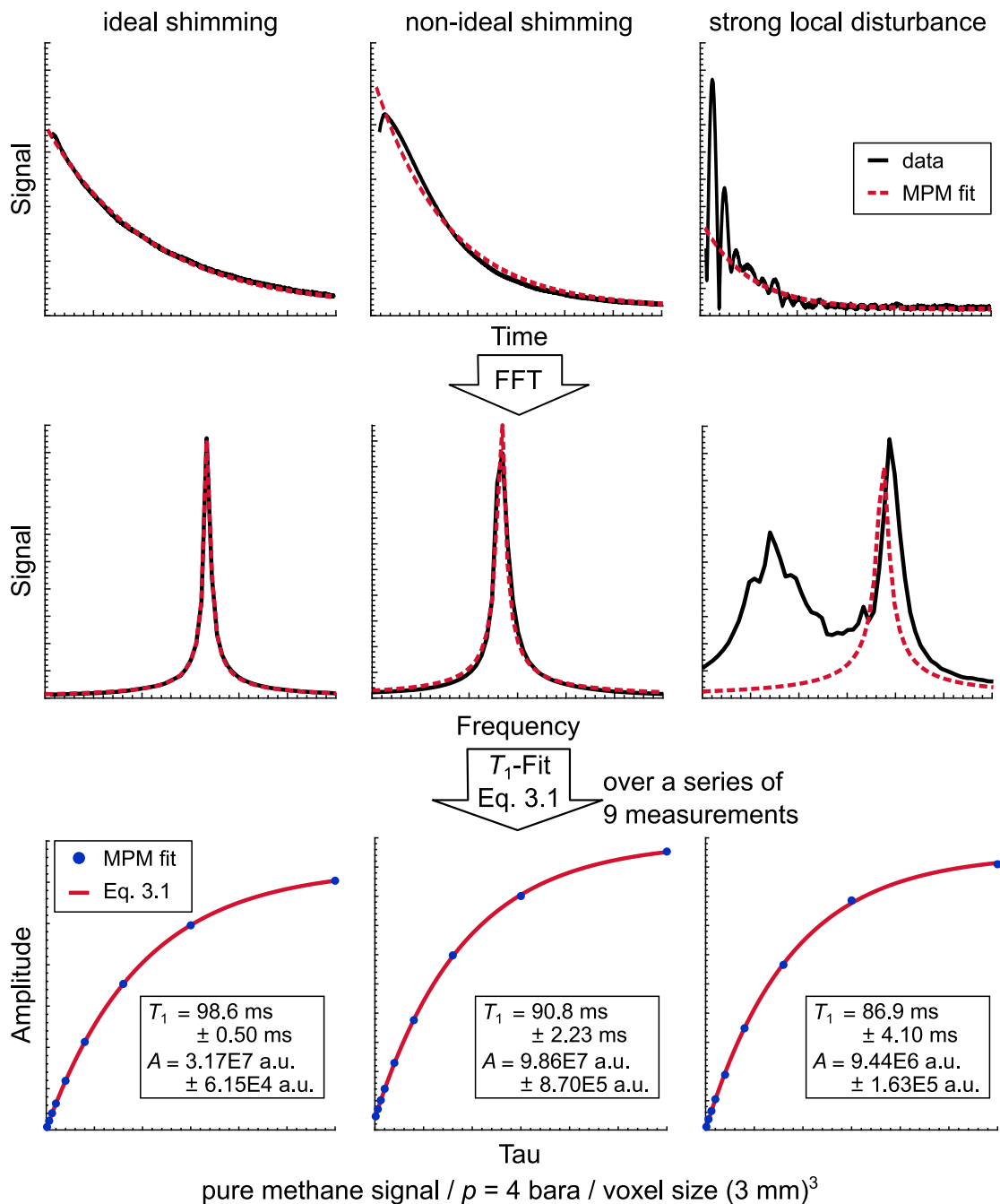
ideal shimming   non-ideal shimming   strong local disturbance

Signal — Time

FFT

Signal — Frequency

T_1-Fit
Eq. 3.1   over a series of
9 measurements

MPM fit
Eq. 3.1

T_1 = 98.6 ms
    ± 0.50 ms
A = 3.17E7 a.u.
    ± 6.15E4 a.u.

T_1 = 90.8 ms
    ± 2.23 ms
A = 9.86E7 a.u.
    ± 8.70E5 a.u.

T_1 = 86.9 ms
    ± 4.10 ms
A = 9.44E6 a.u.
    ± 1.63E5 a.u.

Amplitude — Tau

pure methane signal / p = 4 bara / voxel size (3 mm)^3

Figure B.4: Graphical abstract of the post processing. The FIDs (black line) are fitted using MPM (red line). From a series of 9 measurements, signal amplitude A and T_1 are fitted using Equation 3.2. Frequency spectra are shown for better understanding. They are not part of the post processing. The process is shown for three different qualities of magnetic field homogeneity to visualize its effect on the results. The three voxels were obtained from the reference measurement to state #1 where pure methane was measured at room temperature. Thus, the arrangement of sponge and honeycomb is identical to Figure 6.3. The three voxels are located inside the honeycomb (ideal shimming), in the free gas area in front of the sponge (non-ideal shimming), and at the interface between sponge and honeycomb (strong local disturbance). It can be seen that without proper shimming, the measured T_1 time changes drastically even though the measured amplitudes do not change much. However, the strong local disturbance cannot be reduced by shimming.

List of abbreviations

CI	Confidence interval
CTD	Combined Temperature and Density [technique]
CFD	Computational fluid dynamics
DW-MRI	Diffusion weighted magnetic resonance imaging
FID	Free induction decay
FOV	Field of view
FTS	Fischer-Tropsch synthesis
GHG	Greenhouse gas
GUI	Graphical user interface
NDIR	Non-dispersive infrared spectrometer
NMR	Nuclear magnetic resonance
MFC	Mass flow controller
MPM	Matrix-pencil method
MR	Magnetic resonance
MRI	Magnetic resonance imaging
MRSI	Magnetic resonance spectroscopic imaging
PTFE	Polytetrafluoroethylene
PtX	Power-To-X
RF	Radio frequency
ROI	Region of interest
SNR	Signal-to-noise ratio
STP	Standard temperature and pressure
TMS	Tetramethylsilane

List of symbols

Roman

A	Maximum signal amplitude, a.u.
B	Magnetic flux density, T
B_0	Static magnetic field strength, T
B_1	Dynamic magnetic field strength, T
C	Correction factor / fitting constant, -
C_{eff}	Effective spin-rotation constant, Hz
$\Delta_{\text{R}} H^{298\,\text{K}}$	Standard enthalpy of reaction, $\text{kJ}\,\text{mol}^{-1}$
G	Magnetic field gradient, T
$\hbar$	Reduced Planck constant, $1.0546 \times 10^{-34}\,\text{J s}$
I_0	Principal moment of inertia, $\text{kg}\,\text{m}^2$
k_B	Boltzmann constant, $1.3806 \times 10^{-23}\,\text{J K}^{-1}$
M	Magnetization, $\text{A}\,\text{m}^{-1}$
n	Exponent of temperature dependence / molar amount, - / mol
N	Absolute number of molecules, -
$N_{+/-}$	Amount of spins in/opposite magnetic field direction, -
N_A	Avogadro number, $6.022 \times 10^{23}\,\text{mol}^{-1}$
p	Pressure (absolute), bara
P_{laser}	Heat emitted by the diode laser, W
r	Cartesian coordinate vector, m
R	Gas constant, $8.314\,\text{J}\,\text{mol}^{-1}\,\text{K}^{-1}$
S	Signal, a.u.
S_{m}	Number of nuclei per molecule, -
t	Time, s
T	Temperature, °C|K
T_1	Longitudinal relaxation time, ms
T_2	Transversal relaxation time, ms
T_2^*	Effective transversal relaxation time, ms
T_E	Echo time (delay between RF excitation and start of acquisition), ms
T_R	Repetition time between two sequence executions, ms
$\bar{v}$	Mean relative gas velocity, m^2
V	Volume, m^3
V_{m}	Molar volume, $\text{m}^3\,\text{mol}^{-1}$
x	Mole fraction, -

Greek

γ	Gyromagnetic ratio, rad/T
δ	Gradient duration, s
δ_f	Chemical shift, ppm
θ	Overhead of aligned spins, -
ν	Frequency, Hz
σ_j	Cross section for the collision of one molecule with another, m^2
σ_0	Reference for σ_j at STP, m^2
ρ	Molecular number density, m^{-2}
τ	Wait time in the saturation recovery sequence, s
τ_1	Time between molecule collisions, s
Φ	Angle between two complex signals, rad
ω_0	Larmor frequency, rad/s
ω_L	Angular rotational frequency, rad/s

Indices

0	Reference conditions/STP
i	Referring to different molecular species
x	Cartesian dimension (horizontal axis)
y	Cartesian dimension (vertical axis)
z	Cartesian dimension (axis along magnet bore)

Students work

In the dissertation the results from the supervision of the following students' works are included:

- Sascha Winsemann, Entwicklung einer Methode zum optimierten Abgleich von CFD- und MRI-Daten, 2023

Studentische Arbeiten

In der vorliegenden Arbeit sind Ergebnisse enthalten, die im Rahmen der Betreuung folgender studentischer Arbeiten entstanden sind:

- Sascha Winsemann, Entwicklung einer Methode zum optimierten Abgleich von CFD- und MRI-Daten, 2023

Colophon

This thesis was typeset with $\LaTeX\,2_{\varepsilon}$. It uses the *Clean Thesis* style developed by Ricardo Langner. The design of the *Clean Thesis* style is inspired by user guide documents from Apple Inc.

Download the *Clean Thesis* style at `http://cleanthesis.der-ric.de/`.